Dmitrii Nabok

Cohesive properties of organic crystals and organic/metal interfaces

A density-functional study including van der Waals interactions

Dissertation

written at the Montanuniversität Leoben,
Chair of Atomistic Modeling and Design of Materials

under supervision of
Univ. Prof. Dr. Dr. h.c. C. Ambrosch–Draxl

Leoben, June 2009

Summary

The rapidly developing field of organic electronics has become a particularly important branch in modern solid state physics. Organic semiconductors exhibit interesting physical properties which offer the possibility to design devices with novel structures and functionality such as photovoltaic cells, chemical sensors, and flat panel displays. In addition, mechanically flexible applications can be realized and fabricated at lower costs compared to inorganic semiconductor technology.

The performance of the organic electronic devices is often limited by the material purity. Important properties such as the charge carrier mobility or light-emitting efficiency are insufficient to allow for a wide application of organic semiconductors. Hence, the development of new techniques for material synthesis, the growth of very pure and highly ordered thin films, and their experimental analysis are of prime interest. A sound theoretical background capable of describing the details of the processes is also equally important for the advance of organic electronics and therefore is a topic of a ongoing research and the topic of this thesis.

Density functional theory (DFT) is one of the most powerful and popular theoretical ab-initio method for describing structural and electronic properties of a vast class of materials. For dense matter, DFT has proven its usefulness to account for structure, cohesion and other properties. However, the van der Waals nature of bonding in weakly bound systems such as crystals formed by organic molecules or molecules physisorbed on metal surfaces has imposed severe restrictions on the application of DFT to the investigation of some of their properties. This limitation has only recently been overcome by the development of an extension to DFT, the so-called van der Waals density functional (vdW-DF).

This thesis aims at investigating the cohesive properties of organic semiconductors, and the vdW-DF method represents a central aspect of this investigation. The successful implementation of this scheme is demonstrated to be efficient enough to treat rather complicated systems like organic molecular crystals and their interfaces with metals. The vdW-DF methodology is applied to investigate cohesive and surface energies of three classes of molecular crystals based on small π-conjugated molecules, i.e. the oligoacenes (nA), oligophenylenes (nP), and oligothiophenes (nT). The results are found to be in excellent agreement with reported experimental data for cohesive energies and equilibrium crystal

shapes. This allows for a prediction of surface energies, quantities which are experimentally difficult to access. The vdW-DF is also used for investigating the role of vdW interactions on the adsorption process of organic molecules on metal surfaces. Even in such cases, the nonlocal correlations turn out to be responsible for the binding. Several examples are shown, including thiophenes on clean and oxygen terminated Cu, as well as 3,4,9,10-perylene-tetracarboxyl acid diahydride (PTCDA) on the coinage metals Cu, Ag, and Au. In the latter case, the application of vdW-DF contributed to the solution of a long-standing puzzle about the bonding situation.

A second emphasis of the thesis is on the structure solution of organic molecular solids which show a strong tendency to form polymorphic phases. This is motivated by the fact that molecular arrangements in organic thin films are influenced by the interaction with substrates and lead to substrate-induced crystal structures which can be rather different from the observed bulk structures. The small thickness of the films, however, imposes limitations on the experimental techniques to identify a full crystal structure solution. Therefore, a combined experimental and theoretical study to solve the crystal structure of thin film phases is proposed and applied to the thin film structures of pentacene and *para*-cyano-quaterphenylene. The unit cell parameters as determined from specular and grazing-incidence x-ray diffraction are used as input for our ab-initio optimization of the internal crystal structure to determine the atomic positions and molecular packing inside the unit cell. The reliability of the theoretical optimization procedure is estimated by direct comparison of the experimentally observed and theoretically calculated x-ray diffraction intensities.

Contents

Chapter 1

Introduction

Organic electronics is probably one of the most quickly developing fields in modern solid state physics [1]. The novel physical properties of organic semiconducting materials have provided the main motivation to use these materials as active layers in a variety of electronic devices. Nowadays a growing research effort is devoted to the improvement of the semiconducting, conducting, and light-emitting properties of organic (polymers, oligomers) and hybrid (organic-inorganic) composites. This performance improvement combined with the ability to deposit organic semiconductors at room temperatures on large surface areas such as plastic or paper leads to unique technologies and generates new applications [2]. As a first example, organic light emitting diodes (OLEDs) [3], devices that emit light in the visible and UV range upon the passage of current through an organic semiconductor film, have become now commercially available in small format flat panel displays and are being intensely developed for solid-state lighting. A second example is organic thin film transistors (OFETs) [4], which control the flow of electricity in circuits. OFETs are being developed for applications in smart tags and flat panel displays. Further important and promising applications exist in e.g. photovoltaics [5] and sensing [6].

For the past forty years inorganic semiconductors played an important role in solid state physics. Large amounts of both experimental and theoretical research has been invested in this field. However, with the emergence of organic semiconductors—which have rather different properties compared to inorganic semiconductors—also new techniques of material synthesis and analysis as well as new theoretical approaches are necessary. It is well known, that the charge carrier mobilities, which are crucial parameters for the performance of OFETs devices, show very strong dependence on the organic thin film morphology. Thereby, a deep understanding of organic thin film growth processes is a prerequisite for the production of electronic devices with required characteristics. Moreover, organic solids show a strong tendency to form polymorphic phases. The formation of a specific structure is determined by growth conditions, such as temperature

and deposition rate, as well as the type of substrate. The understanding of the organic/metal interface is not only important for the growth of molecular layers on metallic surfaces, but also regarding their electronic structure. In fact, the interface between metal electrodes and organic active layers is another main parameter which determines the operation of organic light emitting devices.

Turning to computational material science, density functional theory (DFT) is one of the most powerful and popular ab-initio method for describing structural and electronic properties in a vast class of materials. For dense matter, DFT has proven its success to account for structure, cohesion and other properties. The main standard approximations, such as a local-density approximation (LDA) and generalized gradient approximation (GGA), are able to produce equilibrium bond lengths within a few percent. However, the van der Waals (vdW) nature of bonding in soft matter has imposed severe restrictions on the application of LDA and GGA. Some examples of such systems are graphite, molecular crystals, polymers, liquids, biostructures as DNA, and weakly interacting systems such as physisorbed molecules on metal surfaces.

The main problem when incorporating vdW interactions into DFT arises due to the fact that nonlocal or dispersion interactions (of which vdW is one class) are quantum-mechanical manybody effects and require extensive mathematical treatment [7]. An efficient description of vdW interactions is still a challenging task for ab-initio calculations. Recently, several approaches to remedy the lack of the vdW interactions in existing approximations to the exchange-correlation potentials have been developed. They range from very simple methods utilizing the semiempirical vdW correction formula [8], to very complicated ab-initio methods of obtaining an approximate solution of the exact equation for the exchange-correlation energy (the so-called adiabatic connection formula) [9–12].

The van der Waals density functional (vdW-DF) developed by Dion et al. [10] is the most successful current ab-initio approach due to its precision and computational efficiency [13]. Applications of the vdW-DF to typical vdW systems, such as noble gases [10], layered systems such as graphite [14], benzene dimers [15, 16], adsorption of benzene and naphthalene on graphite [17], and many other systems [13] have shown good agreement with both experimental results and other more precise, so-called "benchmark", quantum-chemistry methods.

This thesis aims at providing insight into some of the above described problems by means of DFT studies. Thereby the cohesive properties of organic semiconductors and their polymorphism are the major topics. Aiming at an outlook towards organic thin film growth also organic/metal interfaces are discussed. For all these issues, an efficient implementation of the vdW-DF is a crucial prerequisite which represents another cornerstone of the present work.

The thesis is organized as follows. In Chapter 2 organic semiconductors are introduced. Their structure and the main physical properties relevant for organic

electronics are described. In Chapter 3 an overview of the DFT is given. The exact expression together with the most popular approximations for the exchange-correlation energy are discussed, and the vdW-DF theory is reviewed in detail. It is shown that the main result of the vdW-DF theory is an expression of the nonlocal energy in the form of a 6-dimensional integral that describes the interaction between electron densities in two different space points. This simple form for the vdW interaction energy, however, requires a rather efficient numerical implementation, especially if it is going to be applied to extended systems such as molecular crystals. One of the main achievements of this thesis is a particularly efficient implementation of the vdW-DF. We use an advanced technique of Monte-Carlo multidimensional integration, which is described in detail in Chapter 4. Efficiency and accuracy of this integration method is tested and compared with reported both experimental and theoretical results.

In Chapter 5 we apply the vdW-DF theory to the investigation of equilibrium properties of organic molecular crystals, oligoacene, oligophenylene, and oligothiophene families. Available data on the enthalpy of sublimation allow the estimation of experimental cohesive energies and a comparison with results obtained using different theoretical methodologies. Besides adopting vdW-DF, we also calculate the cohesive energies using the standard exchange-correlation approximations (LDA and GGA), and apply another approach of semiempirically corrected DFT energies. Accuracies of the different methods are discussed. Next, all methodologies mentioned above are applied to the investigation of a quantity that can hardly be experimentally accessed - surface energy. Surface energy defines the morphology of the crystals at growth conditions close to thermodynamical equilibrium, and, hence, the equilibrium crystal shape.

The role of the vdW interactions in the physisorption of molecules on metal surfaces has been a heavily discussed topic. Using our ab-initio tool for treating dispersion interactions, the adsorption of organic molecules such as an isolated thiophene ring or PTCDA on the coinage metals Cu, Ag, and Au are examined in Chapter 6. Our investigations show reasonable agreement with experimental values for the adsorption energies and equilibrium distances and reveal that the main contribution to the binding in these cases is due to the nonlocal energy contribution.

Polymorphism of thin film structures of the organic materials is discussed in Chapter 8. The method of the combined experimental and theoretical study of very thin films (100 nm) is applied to find the crystal structure of so-called substrate induced or thin film phases of pentacene and *para*-cyano-quaterphenylene. The information gained from specular and grazing-incidence x-ray diffraction on the positions and intensities of the reflection peaks only allow the determination of unit cell parameters. Using this data we perform an ab-initio optimization of the internal crystal structure to determine the atomic positions and molecular packing inside the unit cell. The reliability of the theoretical optimization

procedure is estimated by direct comparison of the experimentally observed and theoretically calculated x-ray diffraction intensities. The revealed crystal structure of the pentacene thin film phase is found to be rather different from that of the bulk phase. Comparison between these two phases is analyzed in terms of the electronic band structure.

Chapter 2

Organic semiconductors

2.1 Historical overview

Organic semiconductors represent a large class of solids, comprising organic molecular crystals and polymers. Both are primarily constructed from carbon and hydrogen but often contain also N, O, S, or various metals. Typical representatives of organic semiconductors are aromatic hydrocarbons and alkenes (olefins), N-, O- or S-containing heterocyclic compounds such as pyrrole, furane, thiophene, quinoxaline. In Fig. 2.1 some of the most prominent representatives of polymers (top) and molecular crystals (bottom) that are already used in electronic devices are displayed. These materials have formed the basis for the rapidly developing field of organic electronics, which has the aim of replacing their inorganic counterparts in applications where mechanical flexibility, large area coverage, and inexpensive mass production are required.

The history of organic semiconductors starts from the beginning of the 20th century when first studies of the photoconductivity of anthracene crystals (a prototypical organic semiconductor) were performed. Later, in the 1960s, triggered by the discovery of electroluminescence, molecular crystals were extensively investigated. As a result, the basic processes involved in optical excitation and charge carrier transport in such systems were described [18, 19] and the principal of luminescent diodes based on organic crystals was demonstrated [20]. However, practical difficulties such as the high operation voltage induced by the thickness of the films, insufficient current and light output, and problems with device stability impeded further development in this field.

In the 1970s, the development of new successful techniques for the synthesis and controlled doping of conjugated polymers led to the success of this second important subclass of organic semiconductors [21]. This work was honored with the Nobel Prize in Chemistry in the year 2000. Conducting polymers have led to the first application of organic materials in electronic devices as conductive coating

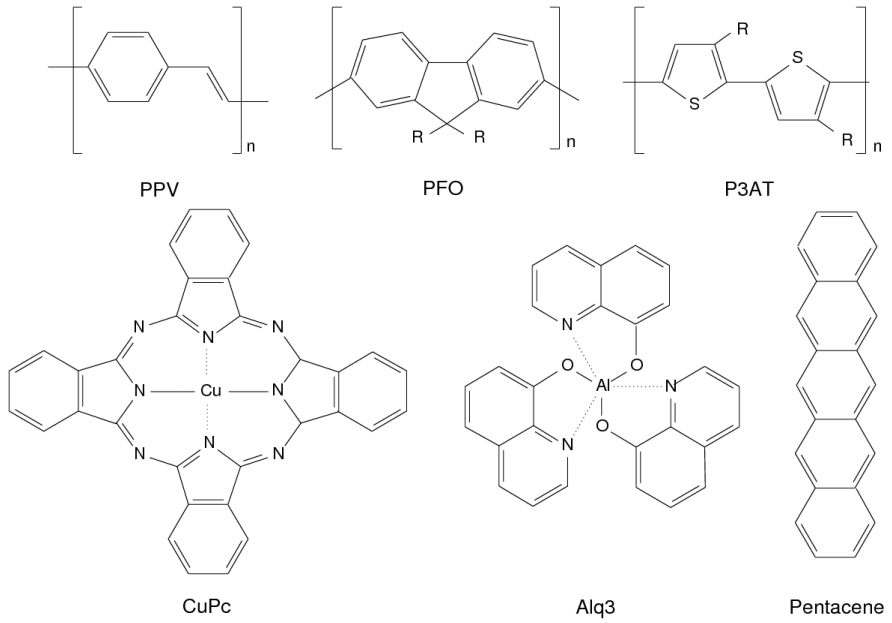

Figure 2.1: Molecular structure of some prototype organic semiconductors: poly(*p*-phenylenevinylene), PPV; polyfluorene, PFO; poly(3-alkylthiophene), P3AT; Cu-phtalocyanine, CuPc; tris(8-hydroxyquinoline)aluminum, Alq3; pentacene.

[22] or photoreceptors in electrography [23]. Since then, organic semiconductors have attracted increasing efforts of both academic and industrial research groups. The demonstration of an organic heterojunction of p- and n-conducting materials in the 1980s [24] showed very promising results for application of undoped organic semiconductors as photovoltaic cells (OPVCs). Tremendous research effort has been directed toward improving the efficiency and functionality of OLEDs. This was initiated by reports of efficient organic light-emitting diodes (OLED) based on thin films of small molecules (Alq_3 and an aromatic diamine) by Tang and Van Slyke [24] and the first polymer-based light-emitting diode (PLED) introduced by Burroughes et al. [25].

A sketch of a typical OLED device is depicted in Fig. 2.2 (left). The first commercial products that incorporate OLED displays have already become available. In addition to OLEDs, remarkable progress has been made in the development of organic thin film transistors (OTFTs) (Fig. 2.2 (right)) [25–27]. Success in the growth of organic crystals with high purity has allowed the best organic materials (one of the most prominent one is pentacene) to achieve charge-carrier mobilities comparable with those of amorphous silicon TFTs. The latter, commonly used as the pixel-switching elements in active matrix flat-panel displays [28], could hence be possibly replaced by organic materials in such applications in the near future.

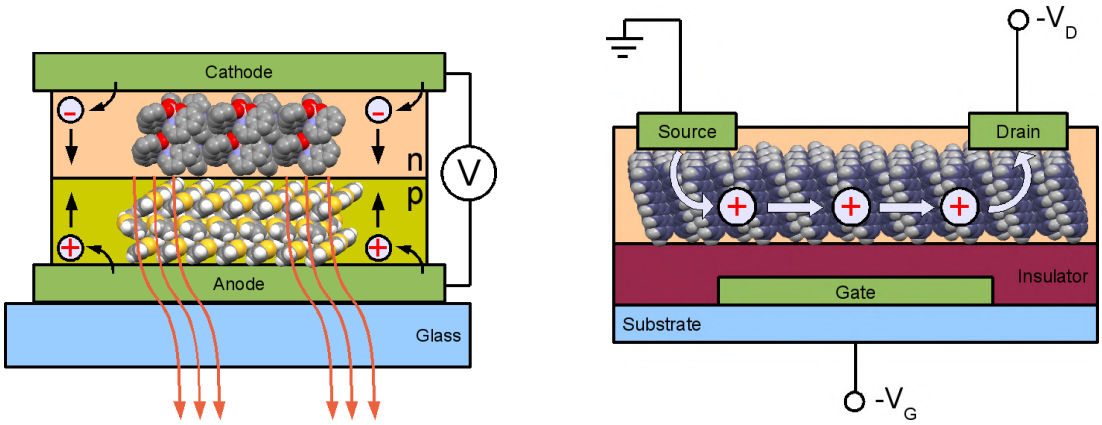

Figure 2.2: Organic electronic devices: Organic light-emitting diodes (OLED) (left) typically have a heterolayer structure consisting of the hole transport layer (p) and the electron transport layer (n); Organic field-effect transistor (right) [1].

2.2 Organic molecular crystals

2.2.1 Crystal structure

In contrast to polymers, built up by infinite chains, oligomers of different length are the building blocks of molecular crystals. Three families of oligomers, i.e. oligoacenes (nA), oligophenylenes (nP), and oligothiophenes (nT), are the simplest and most widely studied representatives of organic semiconductors. nA, nP, and nT belong to the class of heterocyclic π-conjugated aromatic hydrocarbons. Their chemical structures are presented in Fig. 2.3. n benzene rings form the nA and nP oligomers, while nT consists of n thiophene rings which are linked together as shown in Fig. 2.3. Due to their structure, the oligoacene molecules are rather rigid and planar, whereas the torsion angle between neighboring rings in the oligophenylene and oligothiophene molecules has values of about 40° and 20° respectively. However, in the bulk phase all molecules are almost planar.

At room temperature and ambient pressure nA, nP, and nT crystallize in a so-called *herringbone structure* which is very common for planar rod-like molecules. The main features of the herringbone structure are displayed in Fig. 2.4 for a 4P crystal. The molecular crystal consists of layers with almost upright standing molecules. Within one layer, the molecules form a herringbone pattern with typical herringbone angles of about 50°. They all crystallize in a monoclinic space group, except tetracene (4A) and pentacene (5A) which exhibit a lower, triclinic, symmetry.

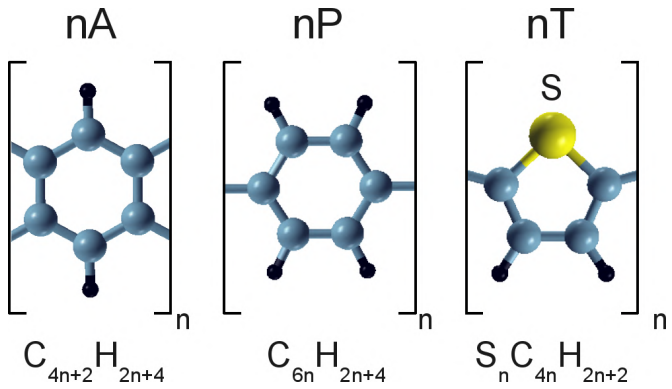

Figure 2.3: Generic structure of oligoacenes (nA), oligophenylenes (nP), and oligothiophenes (nT).

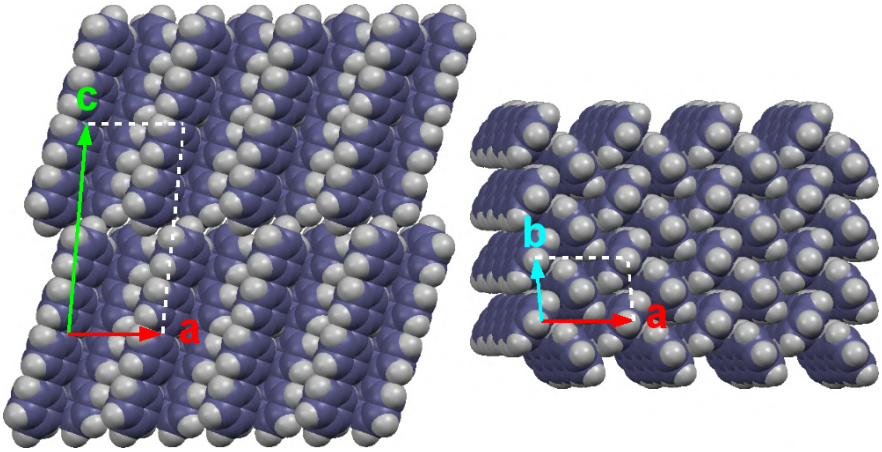

Figure 2.4: The herringbone packing shown for the example of the 4P crystal: layered stacking along **c** direction (left) and herringbone pattern of two inequivalent molecules within the **ab** plane (right).

2.2.2 Electronic structure

The molecules investigated within this thesis belong to the group of conjugated π electron systems. The term π-conjugated comes from the electronic structure of such molecules [29]. The carbon s and p orbitals form three sp^2 orbitals (sp^2 hybridization), i.e. the $2s$ orbital mixes with two of the three original mutually orthogonal p-orbitals, the p_x and p_y, while the third p_z remains unaltered. The hybrid sp_2 orbitals are all coplanar and directed about 120° from each other. The bond formed from these orbitals is called a σ-bond.

Considering the benzene molecule (Fig. 2.5), the sp_2 orbitals make the molecule planar and generate a highly localized and directed electron density in the plane of the ring. In contrast, the p_z orbitals of each carbon atom are perpendicular to

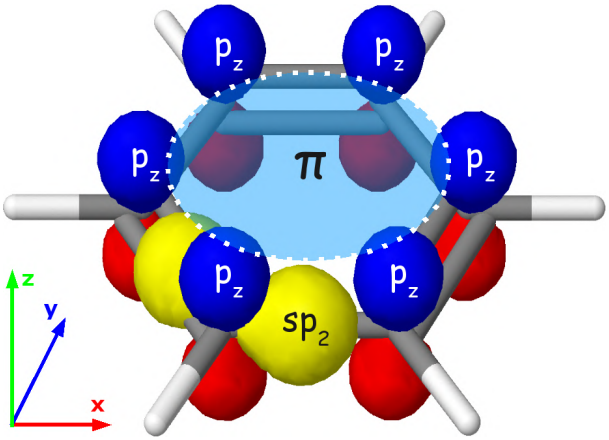

Figure 2.5: Sketch of the molecular orbitals in the benzene – a prototypical aromatic molecule. The sp_2 hybridized orbitals are all coplanar and directed about 120° from each other. The π bond is formed by the overlapping p_z orbitals and marked as a light-blue ellipse. Blue and red color of the p_z orbital states for the negative and positive sign of the wave-function.

the molecular plane. These p_z orbitals overlap to create what is called a π bond. This π bond establishes a delocalized electron density above and below the plane of the ring with no electron density in a nodal plane that coincides with the plane of the molecule.

In comparison with σ electrons, the interaction between π orbitals is weak producing an energy gap between the highest occupied molecular π orbital (HOMO) and the lowest unoccupied molecular π^* orbital (LUMO) in the range of a few eV, leading to a possibility to light adsorption or emission in the visible and near visible spectral range. A sketch of the electronic structure typical for the π-conjugated molecule is depicted in Fig. 2.6. The splitting between HOMO and LUMO π orbitals is rather large (about 5 eV for benzene). However, this value is much lower than the splitting between occupied and unoccupied σ orbitals and has a tendency to reduce when several rings build an oligomer with the inverse oligomer length. Thus, for instance, the band gap of pentacene consisting of five such rings is about 2 eV. The electronic properties of the molecules also strongly depend on the conformation of the molecules or the presence of donating or accepting groups. In this manner, organic chemistry offers the opportunity to tune and select the required optoelectronic properties of organic semiconducting materials.

The nature of the π orbitals is crucial not only for the understanding of the electronic properties, but also for their bonding. This characteristic type of bonding makes organic semiconductors fundamentally different from their inorganic counterparts. The interaction between the molecules are mainly due to weak van der Waals forces which appear since the π orbitals are readily polarizable and easily

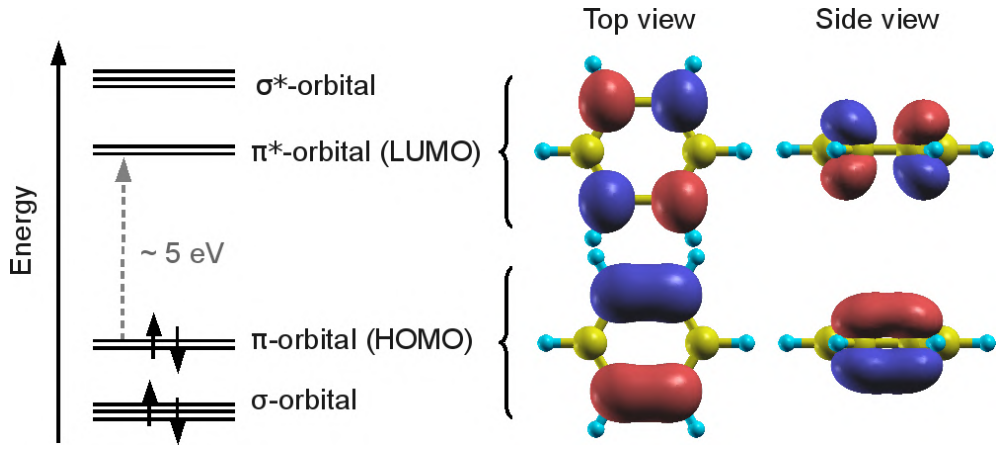

Figure 2.6: Typical energy level ordering in π conjugated molecules. Electronic structure (left) and HOMO and LUMO orbitals (right) of the benzene molecule are depicted.

excited. For this reason, the stability of molecular solids is considerably lower than that of covalently bonded semiconductors. Consequently, mechanical and thermodynamical properties such as hardness or melting point are also lower.

The slight overlap between delocalized π orbitals amongst neighboring molecules also leads to certain implications concerning electronic and optical properties as well as charge carrier transfer. The optical absorption and luminescence spectra of molecular crystals may resemble the spectra in the gas phase or in solution [30], although the packing of the molecules has an important impact on the formation of electron-hole pairs during the absorption process [31, 32]. In any case, knowledge of the properties of an isolated molecule provides a good starting point to understand the properties of the molecular crystal.

In the bulk phase, the weak overlap between molecular electronic orbitals leads to narrow electronic bands and low mobilities of charge carriers ($\mu \sim 1-10$ cm^2/Vs at room temperatures). For comparison, a typical bandwidth $W \sim 0.1 - 0.5$ eV is an order of magnitude smaller than that in inorganic semiconductors [28]. Furthermore, the anisotropy of the transfer integrals between adjacent molecules results in a complicated dependency of the electrical conductance on the crystal orientation.

2.2.3 Charge carrier transport

The performance of electronic devices depends on several parameters. One of the major quantities is the charge carrier mobility μ of a semiconducting material. After several decades of intensive research, basic understanding of charge transport in small-molecule organic semiconductors still remains limited. The

complexity of transport phenomena in these systems is due to the polaronic nature of charge carriers and the strong interaction of small polarons with defects [33]. An especially challenging task is to develop an adequate model of high-temperature polaronic transport. At room temperature, lattice vibrations might become sufficiently strong to destroy the translational symmetry of the lattice. In this regime, the fluctuation amplitude of the transfer integral becomes of the same order of magnitude as its average value [34], the band description breaks down, and a crossover from bandlike transport in delocalized states to incoherent hopping between localized states is predicted at higher temperatures [35]. Thus, the transport properties of highly ordered organic crystals like pentacene have the following features. Upon lowering the temperature the characteristics of band transport can be observed in which the temperature dependence of the mobility follows a power law behavior $\mu \propto T^{-n}$ with $n = 1...3$ [36]. At higher temperatures (300 K), polaron transport becomes more important; that is, the charge carriers (and their associated lattice deformation) move by thermally activated hopping leading to an Arrhenius-type temperature dependence of the mobility ($\mu \propto exp(-E_a/kT)$) [37, 38].

On a microscopic level, the electrical current through a material is determined by the charge carrier density n, the charge carrier mobility μ, and the applied electric field E according to

$$\vec{j} = \vec{\sigma} \cdot \vec{E} = en\vec{\mu} \cdot \vec{E}. \tag{2.1}$$

The dependence of the charge current is not a linear function of the electric field since the charge density and mobility also depend on it. Moreover, this quantity is anisotropic due to the anisotropy of the charge carrier mobility μ.

The charge carrier density is the second crucial parameter for the performance of organic electronic devices. For semiconductors it is given by

$$n_i = N_0 \exp\left(-\frac{E_g}{2kT}\right), \tag{2.2}$$

where E_g is an energy band gap and N_0 is an effective density of states which is proportional to the density of the molecules in the crystal. Using typical values of $E_g = 2.5$ eV and $N_0 = 10^{21}$ cm^{-3} for organic semiconductors, one can get a hypothetical carrier density of $n_i \sim 1$ cm^{-3} at room temperature, whereas the corresponding value for Si ($E_g = 1.12$ eV and $N_0 = 10^{19}$ cm^{-3}) is about $n_i \sim 10^9$ cm^{-3}, many orders of magnitude higher. Thus, pure organic semiconductors have extremely low conductivity insufficient for practical applications.

The most efficient way to overcome the limitations posed by the low charge carrier density is carrier injection from the contacts. The process of carrier injection essentially drives device operation in organic light-emitting diodes (OLEDs) (Fig. 2.2). This requires low energetic barriers at metal/organic interfaces for

both contacts to inject equally large quantities of electrons and holes, which are necessary for a balanced charge carrier flow. Hence, knowledge of the properties at the interfaces between metal electrodes and active organic materials is a prerequisite for the design and production of electronic devices such as OLEDs [39] or OFETs.

Other factors which have a crucial influence on the mobilities are the degree of order and purity of the organic semiconductors. Because of these factors, e.g., in amorphous organic crystals the mobilities can have very low values several orders of magnitude lower than in the corresponding single-crystal phase. Therefore, the synthesis of new organic molecules with predicted high mobilities is always coupled to the task of developing the technology for the production of highly ordered crystals and thin films built of these molecules.

Chapter 3

Theoretical Background

3.1 Density functional theory

3.1.1 The density as the basic variable

The basic theorem of HOHENBERG and KOHN states that the ground state density $n(\mathbf{r})$ of a system of interacting electrons in some external potential $v_{ext}(\mathbf{r})$ determines this potential uniquely (up to an additive constant) [40]. The proof is very simple: Let $n(\mathbf{r})$ be the non-degenerate ground-state density of N electrons in the external potential $v_1(\mathbf{r})$ corresponding to the ground state characterized by the many-electron wave function Ψ_1 and its total energy E_1. Then we can write

$$\begin{aligned} E_1 &= \langle \Psi_1 | \hat{H}_1 | \Psi_1 \rangle \\ &= \int \mathrm{d}^3 r \, v_1(\mathbf{r}) n(\mathbf{r}) + \langle \Psi_1 | \hat{T} + \hat{U} | \Psi_1 \rangle, \end{aligned} \tag{3.1}$$

where $\hat{H}_1$ is the total Hamiltonian corresponding to the external potential $v_1(\mathbf{r})$, and $\hat{T}$ and $\hat{U}$ are the kinetic and electrostatic interaction energy operators, respectively. Now suppose that there exists a second external potential $v_2(\mathbf{r})$, which differs from $v_1(\mathbf{r})$ not only by a constant and leads to the *same* density $n(\mathbf{r})$. If we denote its ground state wave function and energy with Ψ_2 and E_2, respectively, we obtain

$$E_2 = \int \mathrm{d}^3 r \, v_2(\mathbf{r}) n(\mathbf{r}) + \langle \Psi_2 | \hat{T} + \hat{U} | \Psi_2 \rangle. \tag{3.2}$$

The Rayleigh-Ritz minimal principle for Ψ_1 gives the following inequality

$$\begin{aligned} E_1 &< \langle \Psi_2 | \hat{H}_1 | \Psi_2 \rangle \\ &= \int \mathrm{d}^3 r \, v_1(\mathbf{r}) n(\mathbf{r}) + \langle \Psi_2 | \hat{T} + \hat{U} | \Psi_2 \rangle \\ &= E_2 + \int [v_1(\mathbf{r}) - v_2(\mathbf{r})] n(\mathbf{r}) \mathrm{d}^3 r. \end{aligned} \tag{3.3}$$

The analogous argument for the ground state of Ψ_2 leads to the expression

$$E_2 < \langle \Psi_1 | \hat{H}_2 | \Psi_1 \rangle = E_1 + \int [v_2(\mathbf{r}) - v_1(\mathbf{r})] n(\mathbf{r}) \mathrm{d}^3 r. \tag{3.4}$$

Adding Eqs. (3.3) and (3.4) makes the contradiction apparent

$$E_1 + E_2 < E_1 + E_2. \tag{3.5}$$

Thus, our initial assumption of the existence of a second external potential $v_2(\mathbf{r})$ leading to the identical density $n(\mathbf{r})$ must be wrong, and the Hohenberg-Kohn theorem is proven. We note that the proof presented above is based on the assumption of the non-degeneracy of the ground state. This requirement, however, can be lifted as shown by KOHN [41]. Moreover, we have assumed that *any* well-behaved positive function $n(\mathbf{r})$, which integrates to the number of electrons N, is a possible ground-state density corresponding to *some* $v(\mathbf{r})$ (v-representability). LEVY [42] and LIEB [43] have demonstrated that there are indeed examples of well-behaved densities that are not v-representable, but these cases do not appear to limit the practical application of DFT. Thus, the important message of this section is that the total electron density $n(\mathbf{r})$ of a system of interacting electrons determines both the number of electrons N and the external potential $v(\mathbf{r})$. Moreover, the many-body wave function Ψ is also a functional of the electron density $n(\mathbf{r})$ [40]. Consequently, the density gives us the full Hamiltonian $\hat{H}$ for the electronic system, and $n(\mathbf{r})$ implicitly contains all properties derivable from $\hat{H}$ through the solution of the Schrödinger equation.

3.1.2 The Hohenberg-Kohn variational principle

The ground state energy E of a system of interacting electrons can be obtained from the solution of the many-body Schrödinger equation $\hat{H}\Psi = E\Psi$. Another approach is provided by the Rayleigh-Ritz minimal principle

$$E = \min_{\tilde{\Psi}} \langle \tilde{\Psi} | \hat{H} | \tilde{\Psi} \rangle, \tag{3.6}$$

where $\tilde{\Psi}$ is a normalized trial function for the N electron system. Equivalently, the minimal principle can be formulated in terms of trial densities $\tilde{n}(\mathbf{r})$, rather than trial wave functions $\tilde{\Psi}$, as was first shown by HOHENBERG and KOHN [40], and later in the form of the *constrained search method* by LEVY [42]. By integrating $\tilde{\Psi}$ over all space variables except the first, one obtains the corresponding density $\tilde{n}(\mathbf{r})$. Thus, the minimization of Eq. (3.6) may be achieved in two steps: In the first step, we choose a trial density $\tilde{n}(\mathbf{r})$. Denoting all wave functions that result in this density by $\tilde{\Psi}^{\alpha}_{\tilde{n}}$, we define an energy functional of the density using

$$\begin{aligned} E_v[\tilde{n}(\mathbf{r})] &= \min_{\alpha} \langle \tilde{\Psi}^{\alpha}_{\tilde{n}} | \hat{H} | \tilde{\Psi}^{\alpha}_{\tilde{n}} \rangle \\ &= \int v(\mathbf{r}) \tilde{n}(\mathbf{r}) \mathrm{d}^3 r + F[\tilde{n}(\mathbf{r})], \end{aligned} \tag{3.7}$$

where the functional $F[\tilde{n}(\mathbf{r})]$ is independent of the external potential $v(\mathbf{r})$ and given by

$$F[\tilde{n}(\mathbf{r})] = \min_{\alpha} \langle \tilde{\Psi}^{\alpha}_{\tilde{n}} | \hat{T} + \hat{U} | \tilde{\Psi}^{\alpha}_{\tilde{n}} \rangle. \tag{3.8}$$

In the second step, we minimize Eq. (3.7) over all densities $\tilde{n}(\mathbf{r})$ resulting in the ground state energy E

$$\begin{aligned} E &= \min_{\tilde{n}(\mathbf{r})} E_v[\tilde{n}(\mathbf{r})] \\ &= \min_{\tilde{n}(\mathbf{r})} \left\{ \int v(\mathbf{r}) \tilde{n}(\mathbf{r}) \mathrm{d}^3 r + F[\tilde{n}(\mathbf{r})] \right\}. \end{aligned} \tag{3.9}$$

This is the Hohenberg-Kohn minimum principle [40] which states that the total energy is a functional of the density and that the ground state density $n(\mathbf{r})$ minimizes this functional resulting in the ground state energy $E = E[n(\mathbf{r})]$.

3.1.3 The Kohn-Sham equations

Formally, the Hohenberg-Kohn principle provides a strict formulation of the ground-state energy entirely in terms of the density distribution. Practical applications, however, require the knowledge of the functional $F[\tilde{n}(\mathbf{r})]$ defined in Eq. (3.8). Kohn and Sham [44] suggested to write this functional in the form

$$F[\tilde{n}(\mathbf{r})] = T_s[\tilde{n}(\mathbf{r})] + \frac{1}{2} \int \frac{\tilde{n}(\mathbf{r}) \tilde{n}(\mathbf{r}')}{|\mathbf{r} - \mathbf{r}'|} \mathrm{d}^3 r \mathrm{d}^3 r' + E_{xc}[\tilde{n}(\mathbf{r})], \tag{3.10}$$

where $T_s[\tilde{n}(\mathbf{r})]$ is the kinetic energy functional for *non-interacting* electrons, and the second term is the electrostatic or Hartree energy. The last term, $E_{xc}[\tilde{n}(\mathbf{r})]$, as it is defined by Eq. (3.10), includes all other electron-electron interactions and is called the exchange-correlation energy functional. Next, we apply the Hohenberg-Kohn minimum principle in order to obtain the corresponding Euler-Lagrange equations with the functional $F[\tilde{n}(\mathbf{r})]$ defined in (3.10). Variation of the total energy $E_v[\tilde{n}(\mathbf{r})]$ in (3.7) with respect to the density $\tilde{n}(\mathbf{r})$, keeping the total number of electrons unchanged, yield

$$\delta E_v[\tilde{n}(\mathbf{r})] = \int \delta \tilde{n}(\mathbf{r}) \left\{ v_{\text{eff}}(\mathbf{r}) + \frac{\delta}{\delta \tilde{n}(\mathbf{r})} T_s[\tilde{n}(\mathbf{r})] \Big|_{\tilde{n}(\mathbf{r}) = n(\mathbf{r})} - \varepsilon \right\} \mathrm{d}^3 r = 0. \tag{3.11}$$

Here, we have defined the effective potential (Kohn-Sham potential) $v_{\text{eff}}(\mathbf{r})$ as the sum of the external, the Hartree, and the exchange-correlation potential,

$$v_{\text{eff}}(\mathbf{r}) = v_{ext}(\mathbf{r}) + \int \frac{n(\mathbf{r}')}{|\mathbf{r} - \mathbf{r}'|} \mathrm{d}^3 r' + v_{xc}(\mathbf{r}). \tag{3.12}$$

The latter is obtained as the functional derivative of the exchange-correlation energy with respect to the electron density,

$$v_{xc}(\mathbf{r}) = \frac{\delta}{\delta\tilde{n}(\mathbf{r})} E_{xc}[\tilde{n}(\mathbf{r})]\bigg|_{\tilde{n}(\mathbf{r})=n(\mathbf{r})} . \tag{3.13}$$

The Lagrange multiplier ε in Eq. (3.11) ensures the conservation of the number of electrons in the variational procedure.

The structure of (3.11) is the same as for the system of *non-interacting* particles in an effective one-particle potential $v_{\text{eff}}(\mathbf{r})$. Thus, KOHN and SHAM concluded [44] that the minimizing density $n(\mathbf{r})$ can be obtained by solving the single-particle Schrödinger equations

$$\left[-\frac{1}{2}\nabla^2 + v_{\text{eff}}(\mathbf{r}) - \varepsilon_j\right] \varphi_j(\mathbf{r}) = 0 \tag{3.14}$$

with the density $n(\mathbf{r})$ constructed from single particle orbitals $\varphi_j(\mathbf{r})$

$$n(\mathbf{r}) = \sum_{j=1}^{N} |\varphi_j(\mathbf{r})|^2 . \tag{3.15}$$

Equations (3.14) and (3.15), with the definitions of the effective potential (3.12) and the local exchange-correlation potential (3.13), are called the Kohn-Sham equations. These equations have to be solved self-consistently: Starting from an initial guess for the Kohn-Sham potential v_{eff}, the Kohn-Sham equations (3.14) are diagonalized yielding the Kohn-Sham energies ε_j and orbitals φ_j, which give the density n via Eq. (3.15). The density, in turn, determines a new effective potential by applying relations (3.12) and (3.13). This cycle is repeated until a converged ground state density is obtained. The ground state energy E may then be calculated from the ground state density as

$$E = \sum_{j=1}^{N} \varepsilon_j + E_{xc}[n(\mathbf{r})] - \int v_{xc}(\mathbf{r}) n(\mathbf{r}) \mathrm{d}^3 r - \frac{1}{2} \int \frac{n(\mathbf{r}) n(\mathbf{r}')}{|\mathbf{r} - \mathbf{r}'|} \mathrm{d}^3 r \mathrm{d}^3 r' . \tag{3.16}$$

Note that with the *exact* expression for E_{xc} and v_{xc} all many-body effects are, in principle, included in the calculation of the ground state properties. Clearly, the usefulness of the Kohn-Sham equations depend entirely on whether approximations for the functional $E_{xc}[n(\mathbf{r})]$ can be found which are both sufficiently simple and accurate. The next section deals with such approximations for the exchange-correlation energy functional $E_{xc}[n(\mathbf{r})]$.

3.1.4 Approximations for E_{xc}

Despite the elegance of the Kohn-Sham equations, they would remain useless in practice without adequate approximations for the exchange-correlation functional

$E_{xc}[n(\mathbf{r})]$. These approximations reflect the many-body aspects of interactions between electrons and come from outside of DFT.

The local density approximation

The simplest approximation for $E_{xc}[n(\mathbf{r})]$ is the so-called local-density approximation (LDA)

$$E_{xc}^{LDA}[n(\mathbf{r})] = \int e_{xc}\left(n(\mathbf{r})\right) n(\mathbf{r}) \mathrm{d}^3 r, \tag{3.17}$$

where $e_{xc}(n(\mathbf{r}))$ is the exchange-correlation energy per particle of a *uniform* electron gas of density $n(\mathbf{r})$ at a point $\mathbf{r}$ [44]. Thus, the local contribution to the xc energy of the non-uniform system is taken to be identical to the xc energy of the uniform electron gas of the same density. The exchange part $e_x(n)$ can be calculated analytically and is given by

$$e_x(n) = -\frac{0.458}{r_s}, \tag{3.18}$$

where r_s is the radius of a sphere containing one electron and is determined by setting the sphere volume $(4\pi/3)r_s^3$ equal to the inverse density. The correlation part was first calculated by Ceperly [45] and Ceperly and Alder [46] using Quantum Monte Carlo methods. The LDA is obviously exact for a homogeneous electron gas. Moreover, it was expected that for non-uniform cases it should only be valid for densities that are slowly varying on the scale of the local Fermi wavelength λ_F. However, it turned out that the LDA gives reasonable results not only for free-electron systems like metals but also for atoms and molecules where the condition of slowly varying densities is not satisfied. Indeed, a great number of calculations have shown that the LDA gives ionization energies of atoms and dissociation energies of molecules with an accuracy of typically 10–20%. Structural properties such as bond lengths or vibrational frequencies even agree to within 1–5% with experimental values. This remarkable success of the LDA can be at least partially explained by an exact sum rule that is satisfied by the LDA (see the next subsection). Moreover, the self-consistent solution of the Kohn-Sham equations using the LDA for the exchange-correlation energy is a conceptually very easy task and it is less demanding than the solution of the Hartree-Fock equations.

Despite the success of LDA, it is often unsatisfactory in condensed-matter systems. The principal difficulty is connected with the fact that in real systems the density is clearly not uniform. Even if its predictions are qualitatively acceptable (which is not always the case), quantitatively the LDA is far from perfect. The absolute error in the atomization energies of molecules is of the order of 1 eV – much larger than the desired chemical accuracy of roughly 0.05 eV [47–49]. Moreover, the LDA tends to overestimate the bond strength, resulting in bond lengths

that are typically too short by several percent and leading to more close-packed crystal structures [49].

The generalized gradient approximation

Many of the above mentioned failures of the LDA are remedied using the Generalized Gradient Approximation (GGA) for the exchange-correlation energy [49], which is given by

$$E_{xc}^{GGA}[n(\mathbf{r})] = \int f\left(n(\mathbf{r}), |\nabla n(\mathbf{r})|\right) n(\mathbf{r}) \mathrm{d}\mathbf{r}. \tag{3.19}$$

The GGA is also dubbed a semilocal approximation of the exchange-correlation energy. It includes information on deviations from homogeneity by considering the gradients of the charge density. $f(\cdot)$ in Eq. (3.19) is the thoroughly constructed function that reproduces the exact result in certain limits, e.g., the slowly and rapidly varying density cases, and obeys many important properties of the exact functional (see Subsection 3.1.5).

Nowadays, many realizations of GGA exist and compete with each other in precision, universality, and computational efficiency. The most popular of them are Perdew-Burke-Ernzerhof (PBE) [50] with its latest modification (PBEsol) [51], different "revised" versions of PBE – revPBE [52] and RPBE [53], meta-GGA [such as Tao-Perdew-Staroverov-Scuseria (TPSS)], Armiento-Mattsson GGA (AM05) [54]. The comparison between different sorts of GGA and assessment their performance can be found in very recent works by Csonka et al. [55] and Haas et al. [56].

The usage of such gradient-corrected functionals [49, 50, 57–61] yield much better results for atomization energies of molecules and enthalpies of formation derived from atomization energies than LDA. In particular, they provide a good description of the hydrogen bond, thus opening a method to work with compounds where the hydrogen bond is crucial (e.g. water), whereas LDA is unusable for those systems since it predicts hydrogen bonds which are too strong due to the mentioned above general trends to overbind results.

Unfortunately, GGA also suffers from serious deficiencies that can result in qualitatively incorrect computations. One deficiency is that the popular GGAs do not improve the calculated lattice constants. Both LDA and GGA give errors of comparable magnitude, although generally of opposite sign. For instance, for a small set of metals, it has been shown that LDA underestimates the lattice constants on average by -0.7% and GGA overestimates it by 1.8%. This leads to one order of magnitude higher error in the bulk modulus: 11.6% for LDA and -13.7% for GGA [62]. Thereby, the calculation of properties such as phonon frequencies, ferromagnetism, ferroelectricity and others that are critically dependent on volume can be problematic.

Another shortcoming of the mentioned above approximations, the long-ranged dispersion interactions, is one of the topics of this thesis and will be discussed in detail in Section 3.2.

3.1.5 The adiabatic connection formula

Practical and well-defined in the limit of an almost uniform density, the theory of Hohenberg, Kohn, and Sham favored the appearance of an explicit formula for the treatment of the exchange-correlation energy $E_{xc}[n]$, the *Adiabatic Connection Formula* (ACF), which was derived independently by Langreth and Perdew [63], and by Gunnarsson and Lundqvist [64].

The Kohn-Sham equations are the result of an exact mapping between the physical interacting-electron and fictitious noninteracting-electron systems. This mapping can also be viewed as an adiabatic turning-off of the Coulomb interaction between electrons:

$$U_\lambda = \lambda \frac{e^2}{2} \sum_{i,j} \frac{1}{|\mathbf{r}_i - \mathbf{r}_j|} = \lambda U, \tag{3.20}$$

where λ goes from $\lambda = 1$ for the interacting system to $\lambda = 0$ for the noninteracting system. The charge density is forced to remain equal to the charge density of the interacting system, i.e.,

$$n_\lambda(\mathbf{r}) = n(\mathbf{r}). \tag{3.21}$$

In order to keep the density fixed, the external potential v should also depend on λ. At $\lambda = 0$, the energy functional has the simple form

$$E_0 = T_s[n(\mathbf{r})] + \int n(\mathbf{r}) v_{\lambda=0}(\mathbf{r}) \mathrm{d}\mathbf{r} \tag{3.22}$$

where $v_{\lambda=0}$ simply corresponds to v_{ext} of Eq. (3.12).

In the next step, the energy functional for the true interacting system is written as an integral of the derivative with respect to λ as

$$E = E_0 + \int_0^1 \frac{dE_\lambda}{d\lambda} \mathrm{d}\lambda. \tag{3.23}$$

Using the Hellmann-Feynman theorem, the derivative can be expressed as

$$\frac{dE_\lambda}{d\lambda} = \langle \Psi_\lambda | \frac{\partial H}{\partial \lambda} | \Psi_\lambda \rangle. \tag{3.24}$$

Taking into account the dependence of the Hamiltonian on λ, $H = v_\lambda + \lambda U$, the expression is rewritten as

$$\frac{dE_\lambda}{d\lambda} = \langle \Psi_\lambda | U | \Psi_\lambda \rangle + \langle \Psi_\lambda | \frac{\partial v_\lambda}{\partial \lambda} | \Psi_\lambda \rangle. \tag{3.25}$$

Integrating Eq. (3.23), one can obtain

$$E = E_0 + \int_0^1 E_\lambda^{coul} \mathrm{d}\lambda + \int \mathrm{d}\mathbf{r} n(\mathbf{r})(v_{\lambda=1}(\mathbf{r}) - v_{\lambda=0}(\mathbf{r})). \tag{3.26}$$

After insertion of Eq. (3.22) in the previous expression, one gets

$$E = T_s + \int \mathrm{d}\mathbf{r} n(\mathbf{r}) v_{\lambda=1}(\mathbf{r}) + \int_0^1 E_\lambda^{coul} \mathrm{d}\lambda. \tag{3.27}$$

Comparing to the Kohn-Sham expression (3.10) for the total energy, one can immediately find

$$E_{xc} = \int_0^1 \left(E_\lambda^{coul} - E_H\right) \mathrm{d}\lambda. \tag{3.28}$$

This expression can be transformed [64] to

$$E_{xc} = \frac{1}{2} \int \frac{n_{xc}(\mathbf{r}, \mathbf{r}')}{|\mathbf{r} - \mathbf{r}'|} n(\mathbf{r}) \mathrm{d}\mathbf{r} \mathrm{d}\mathbf{r}', \tag{3.29}$$

where the quantity $n_{xc}(\mathbf{r}, \mathbf{r}')$ is known as the *exchange-correlation hole*. By definition, the exchange-correlation hole is

$$n_{xc}(\mathbf{r}, \mathbf{r}') = g(\mathbf{r}, \mathbf{r}') - n(\mathbf{r}'), \tag{3.30}$$

where $g(\mathbf{r}, \mathbf{r}')$, which is the conditional density at $\mathbf{r}'$ given that one electron is at $\mathbf{r}$. It describes the "hole" dug into the average density $n(\mathbf{r}')$ by the electron at $\mathbf{r}$ [65]. The exchange-correlation hole obeys the sum rule

$$\int n_{xc}(\mathbf{r}, \mathbf{r}') \mathrm{d}\mathbf{r}' = -1, \tag{3.31}$$

which can be interpreted as the charge missing around a point $\mathbf{r}$ due to the combined exchange effect of the Pauli principle and electron-electron interaction. Hence, the expression (3.29) allows a physical interpretation of the exchange-correlation energy as the interaction of the electron with its exchange-correlation hole.

3.2 Van der Waals interactions

The van der Waals (vdW) forces belong to the special class of interactions that arise between sufficiently separated (such as electronic orbitals without overlap) atoms, molecules, and surfaces and are fundamentally different from covalent or ionic interactions. One usually distinguishes between three types of vdW interactions. The first group consists of electrostatic dipole-dipole (multipole-multipole)

interactions. The second group includes interactions between dipole (multipole) of one object and the induced dipole (multipole) on another object due to the polarization. The third subclass encloses interactions that arise from the interactive forces between temporary multipoles in molecules without permanent multipole moments. These forces are known as *dispersion* interactions or interactions between instantaneous dipoles. On the microscopic level, the nature of the latter is connected with the high polarizability of the valence electrons of atoms that easily align themselves in a concerted motion, known as plasma oscillations, under the influence of a time-dependent external field. Thus, prediction of the vdW attraction requires a fully quantum-mechanical treatment.

Whereas the first two groups of the vdW forces are exactly included in the density functional theory, an efficient description of vdW interactions is still a challenging task for ab-initio calculations and a hot topic of current investigations. The main problem of incorporating vdW interactions into DFT is due to the complicated underlying many-body physics [7] and computational complexity.

Several distinct methods are currently available for dealing with vdW interactions within DFT. The simplest of them is a method of semiempirical correction of the DFT energies by considering the dispersion interaction as directly occurring between the nuclei via empirically determined potentials. Such methods are very simple and computationally efficient but often suffer from inaccuracy and lack of transferability. Such a method reported by Grimme [8, 66] is used in this work and will be described below. Another method is a recently developed density-functional version of symmetry adapted perturbation theory (SAPT-DFT) [67, 68]. It gives very accurate results, but its applications are limited to fairly small systems. Moreover, this method is not devoid of adjustable semiempirical elements. Nowadays, the methods based on an approximate solution of the adiabatic connection formula (3.29) have been increasing in popularity. The random phase approximation (RPA) method has been applied to many systems, including molecules [69] and solids [11]. This approach is very promising, although it is computationally quite demanding and still requires further investigation. The most successful method for treating the van der Waals interactions within DFT is a recently developed theory of the van der Waals density functional (vdW-DF), which is becoming more popular due to its accuracy and computational efficiency in comparison with other ab-initio methods. Similar to the RPA method, the vdW-DF is based on special approximations to the solution of the ACF. This method has been chosen as a main tool in this thesis for investigation of the cohesive properties of organic crystals and organic/metal interfaces. It describes dispersion interactions in the most general and seamless fashion, yielding the known correct asymptotics. Derivation of the exchange-potentials based on vdW-DF has enabled fully self-consistent DFT calculations that allow the performance of the highly required structure optimization of many weakly-bound systems and provide a basis for further developments, such as the evaluation of

forces and stress tensors [70].

3.2.1 Semiempirical vdW correction formula

A straightforward way to deal with vdW systems, such as molecular crystals, in the framework of the DFT and standard approximations for the exchange-correlation potentials is to add an empirical potential of the well-known asymptotic form $C_6 \cdot R^{-6}$ to the usual DFT energy, where R are interatomic distances and C_6 are dispersion coefficients. The careful and systematic study of this approach was performed by S. Grimme [8, 66].

The corrected total energy in this method is given by

$$E_{total} = E_{DFT} + E_{disp}, \tag{3.32}$$

where E_{DFT} is the energy as obtained from a self-consistent DFT calculation and E_{disp} is an empirical dispersion correction given by

$$E_{disp} = -s_6 \sum_{i=1}^{N_{at}-1} \sum_{j=i+1}^{N_{at}} \frac{C_6^{ij}}{R_{ij}^6} f_{damp}(R_{ij}). \tag{3.33}$$

Here, N_{at} is the number of the atoms in the system, C_6^{ij} denotes the dispersion coefficients for atom pair ij, s_6 is a global scaling factor that depends on the DF used, and R_{ij} is an interatomic distance. A damping function f_{damp} must be used to avoid near-singularities for small R and is given by

$$f_{damp}(R_{ij}) = \frac{1}{1 + e^{-d(R_{ij}/R_r - 1)}}, \tag{3.34}$$

where R_r is the sum of atomic vdW radii. The values of the vdW radii for several atoms are given in Table 3.1 together with the atomic coefficients C_6. The exponential damping factor is chosen to be $d = 20$. For the composed coefficients C_6^{ij} a geometric mean of the form

$$C_6^{ij} = \sqrt{C_6^i C_6^j} \tag{3.35}$$

is employed. The values of van der Waals radii R_0 are derived purely theoretically from the electron density. The C_6 parameters were obtained using the London formula for dispersion and first-principles DFT/PBE0 calculations of atomic potentials I_p and static dipole polarizabilities α. The calculated C_6 coefficients are model-dependent quantities that describe the atomic contribution to the dispersion in a molecular environment and, thus, cannot be directly compared with free atom values. In the next step, a special fitting procedure was used to obtain the final values of C_6, R_0, s_6, and d. The reference set of the molecules and

Table 3.1: C_6 parameters (in J·nm^6/mol) and van der Waals radii R_0 (in Å) for selected elements.

Element	C_6	R_0	Element	C_6	R_0
H	0.14	1.001	F	0.75	1.287
C	1.75	1.452	S	5.57	1.683
N	1.23	1.397	Cl	5.07	1.639
O	0.70	1.342	Ar	4.61	1.595

reactions consisted of 30 atomization energies, 8 atomic ionization potentials, 3 proton affinities, 15 chemical reactions, and 21 noncovalently bound complexes. In particular, the s_6 scale factor has been determined by least-squares optimization of interaction energy deviations and found to be 0.75 for the PBE flavor of the exchange-correlation functional.

Concluding this section, some technical remarks about the calculation of the semiempirically corrected energies used in this work are given. The PBE total energy is obtained from a self-consistent calculation for optimized molecular and crystal structures. For calculation of the vdW dispersion correction term E_{disp} of the crystals, a cluster was created by translating the unit cell in each direction by a factor of 10. This value has been checked and is found to be sufficient to give converged results.

3.2.2 The vdW density functional

The theory of the van der Waals density functional divides the correlation energy into two parts [71],

$$E_c[n] = E_c^0[n] + E_c^{nl}[n]. \tag{3.36}$$

$E_c^{nl}[n]$ is defined to include the long-ranged or most nonlocal terms including the van der Waals interactions; it approaches zero in the limit of a slowly varying system. The first term, $E_c^0[n]$, is also semilocal, however, considering the long-range term in Eq. (3.36) separately, it seems to be a reasonable approximation to treat E_c^0 in LDA, which is precise in the limit of slowly varying densities:

$$E_c^0[n] \approx E_c^{LDA}[n]. \tag{3.37}$$

The evaluation of the second term, E_c^{nl}, can be considerably simplified by noting that the long-range interactions are less sensitive to the details of the system's dielectric response than the short-range terms. Thus, a rather simple approximation for the dielectric function in the long-range terms may be made. As

discussed in Ref. [71], the second term of Eq. (3.36) is obtained from the adiabatic connection formula by treating the so-called full potential approximation, which is exact at long distances between separated fragments:

$$E_c^{nl} = \int_0^\infty \frac{du}{2\pi} \mathrm{tr}\left[\ln(1 - V\tilde{\chi}) - \ln\epsilon\right]. \tag{3.38}$$

Here, $\tilde{\chi}$ is the density response to a fully self-consistent potential, $V = 1/|\mathbf{r}_1 - \mathbf{r}_2|$ is the electron-electron Coulomb interaction, ϵ is an approximated dielectric function, and u is the imaginary frequency. There is no double counting, because $(1 - V\tilde{\chi}) = \epsilon$ for a uniform system and the term E_c^{nl} vanishes as it should.

The expression for a truly nonlocal correlation functional based on (3.38) was developed by Rydberg et al. for layered structures [14]. The generalization for the case of general geometries was then derived by Dion and coworkers [10]. In their scheme, the nonlocal correlation energy (3.38) is expanded to second order in terms of the quantity $S = 1 - \epsilon^{-1}$, leading to the expression

$$E_c^{nl} = \int_0^\infty \frac{du}{4\pi} \mathrm{tr}\left[S^2 - \left(\frac{\nabla S \cdot \nabla V}{4\pi e^2}\right)^2\right]. \tag{3.39}$$

In order to evaluate Eq. (3.39), a simple approximation for S, as a functional of the density, was made. This choice is constrained by a number of exact relationships. In a plane-wave representation, $S_{\mathbf{q},\mathbf{q}'}$ has several requirements. First, the f-sum rule imposes

$$S_{\mathbf{q},\mathbf{q}'} \to -\frac{4\pi e^2}{m\omega^3} n_{\mathbf{q}-\mathbf{q}'} \tag{3.40}$$

at large frequencies, where $n_{\mathbf{k}}$ is the Fourier transform of the density. Second,

$$\int_{-\infty}^{\infty} \mathrm{d}u S_{\mathbf{q},\mathbf{q}'}(iu) \to \frac{8\pi^2 N e^2}{q^2} \tag{3.41}$$

for large q, where N is the number of electrons, in order to reproduce the exactly known self-correlation. Third, $S_{\mathbf{q},\mathbf{q}'} = S_{-\mathbf{q},-\mathbf{q}'}$ due to time reversal invariance. Finally, a finite $S_{\mathbf{q},\mathbf{q}'}(\omega)$ for vanishing q or q' at all nonzero values of ω is required to give an exchange-correlation hole with the correct volume (charge conservation).

An approximate S in vdW-DF theory is based on the plasmon-pole model for the dielectric function [71],

$$\epsilon = 1 + \frac{\omega_p^2}{\omega_q^2 - \omega_p^2 - \omega^2}, \tag{3.42}$$

where

$$\omega_q^2 = \omega_p^2 + \frac{k_F^2 q^2}{3} + \frac{q^4}{4}, \tag{3.43}$$

with $\omega_p^2 = 4\pi n$ and $k_F = (3\pi^2 n)^{1/3}$. In this way, a model for S, incorporating the above mentioned constraints, is constructed in Fourier space as a nonuniform generalization of Eq. (3.42):

$$S_{\mathbf{q},\mathbf{q}'} = \frac{1}{2}\left(\tilde{S}_{\mathbf{q},\mathbf{q}'} + \tilde{S}_{-\mathbf{q},-\mathbf{q}'}\right), \tag{3.44}$$

where

$$\tilde{S}_{\mathbf{q},\mathbf{q}'} = \int \mathrm{d}^3 r e^{-i(\mathbf{q}-\mathbf{q}')\cdot\mathbf{r}} \frac{4\pi n(\mathbf{r})e^2/m}{[\omega + \omega_q(\mathbf{r})][-\omega + \omega_{q'}(\mathbf{r})]}. \tag{3.45}$$

To simplify the numerical calculations, Eq. (3.43) is replaced by a different dispersion formula [10]:

$$\omega_q(\mathbf{r}) = \frac{q^2}{2m}\frac{1}{h(q/q_0(\mathbf{r}))}, \tag{3.46}$$

with the switching function

$$h(y) = 1 - \exp\left(-\gamma y^2\right), \tag{3.47}$$

where $\gamma = 4\pi/9$ is an adjustable parameter and the quantity q_0 is defined below.

The remainder of the exchange correlation energy, $E_{xc}^0 = E_{xc} - E_c^{nl}$, can also be expressed in terms of S, resulting in the following approximation [10]:

$$E_{xc}^0 = \int \mathrm{d}^3 r \; n(\mathbf{r})\epsilon_{xc}^0(\mathbf{r}), \tag{3.48}$$

with

$$\epsilon_{xc}^0(\mathbf{r}) = \frac{\pi e^2}{m}\int \frac{\mathrm{d}^3 q}{(2\pi)^3}\left[\frac{1}{\omega_q(\mathbf{r})} - \frac{2m}{q^2}\right]. \tag{3.49}$$

Here, the second term in brackets is the self-energy substraction written explicitly. Upon substitution from (3.46), one finds that

$$\epsilon_{xc}^0(\mathbf{r}) = \frac{e^2 q_0(\mathbf{r})}{\pi}\int_0^\infty \mathrm{d}y[h(y) - 1] = -\frac{3e^2}{4\pi}q_0(\mathbf{r}). \tag{3.50}$$

Thus,

$$q_0(\mathbf{r}) = -\frac{4\pi}{3}\epsilon_{xc}^0(\mathbf{r}) = k_F(\mathbf{r})F_{xc}^0(n(\mathbf{r}), s(\mathbf{r})), \tag{3.51}$$

where F_{xc}^0 is an enhancement factor, dependent on the electron density n and the reduced density gradient $s = |\nabla n|/(2k_F n)$ [72]. Specifically,

$$F_{xc}^0 = 1 + \lambda s^2 - \frac{4\pi}{3k_F}\epsilon_c^{LDA} \tag{3.52}$$

with $\lambda = 0.09434$ has been proposed [10].

Writing Eq. (3.39) in a plane-wave representation gives

$$E_c^{nl} = \int_0^\infty \frac{\mathrm{d}u}{4\pi} \sum_{\mathbf{q},\mathbf{q}'} [1 - (\mathbf{q}\cdot\mathbf{q}')^2] S_{\mathbf{q},\mathbf{q}'} S_{\mathbf{q}',\mathbf{q}}. \tag{3.53}$$

After some tedious algebra [10], this expression can be transformed to

$$E_c^{nl} = \frac{1}{2} \int \mathrm{d}^3 r \mathrm{d}^3 r' n(\mathbf{r}) \phi(\mathbf{r},\mathbf{r}') n(\mathbf{r}'). \tag{3.54}$$

This is the main result of the vdW-DF theory, which expresses the nonlocal correlation energy as an integral of a function describing interaction between the electron density at point $\mathbf{r}$ and $\mathbf{r}'$. Details of this interaction are hidden in the kernel function ϕ, which is, by construction, a generalized function of space coordinates, the electron densities and their gradients, i.e., $\phi = \phi(|\mathbf{r} - \mathbf{r}'|, n(\mathbf{r}), n(\mathbf{r}'), \nabla n(\mathbf{r}), \nabla n(\mathbf{r}'))$. The kernel ϕ is given by

$$\phi(\mathbf{r},\mathbf{r}') = \frac{2me^4}{\pi^2} \int_0^\infty a^2 \, \mathrm{d}a \int_0^\infty b^2 \, \mathrm{d}b \; W(a,b) \cdot T(\nu(a),\nu(b),\nu'(a),\nu'(b)), \tag{3.55}$$

where

$$T(w,x,y,z) = \frac{1}{2}\left[\frac{1}{w+x} + \frac{1}{y+z}\right]\left[\frac{1}{(w+y)(x+z)} + \frac{1}{(w+z)(y+x)}\right], \tag{3.56}$$

and

$$\begin{aligned} W(a,b) \;&= 2[(3-a^2)b\cos b \sin a + (3-b^2)a\cos a \sin b + \\ &\quad (a^2+b^2-3)\sin a \sin b - 3ab\cos a \cos b]/(a^3b^3). \end{aligned} \tag{3.57}$$

The quantities ν and ν' are expressed by

$$\nu(y) = y^2/2h(y/d), \qquad \nu'(y) = y^2/2h(y/d'), \tag{3.58}$$

where

$$d = |\mathbf{r} - \mathbf{r}'| q_0(\mathbf{r}), \qquad d' = |\mathbf{r} - \mathbf{r}'| q_0(\mathbf{r}'), \tag{3.59}$$

and q_0 is given by Eq. (3.51). The kernel ϕ thus depends on $\mathbf{r}$ and $\mathbf{r}'$ only through d and d', so that ϕ can be tabulated in advance in terms of these two variables, or better, in terms of the sum and difference variables D and δ defined by

$$D = \frac{1}{2}(d + d'), \quad 0 \le D \le \infty, \tag{3.60}$$

$$\delta = \frac{d - d'}{d + d'}, \quad 0 \le |\delta| \le 1. \tag{3.61}$$

When both d and d' are large, the asymptotic form of $\phi(d, d')$ is

$$\phi \to -\frac{C}{d^2 d'^2 (d^2 + d'^2)}, \tag{3.62}$$

with $C = 12(4\pi/9)^3 me^4$. Thus, the interaction energy has the correct r^{-6} dependence for large separation r. Another important feature of the kernel function is that E_c^{nl} is strictly zero for systems with a uniform (constant) distributed electron density, as was initially imposed by the approximation Eq. (3.36). In Fig. 3.1, a plot of $4\pi D^2 \phi$ vs D for several values of δ is shown.

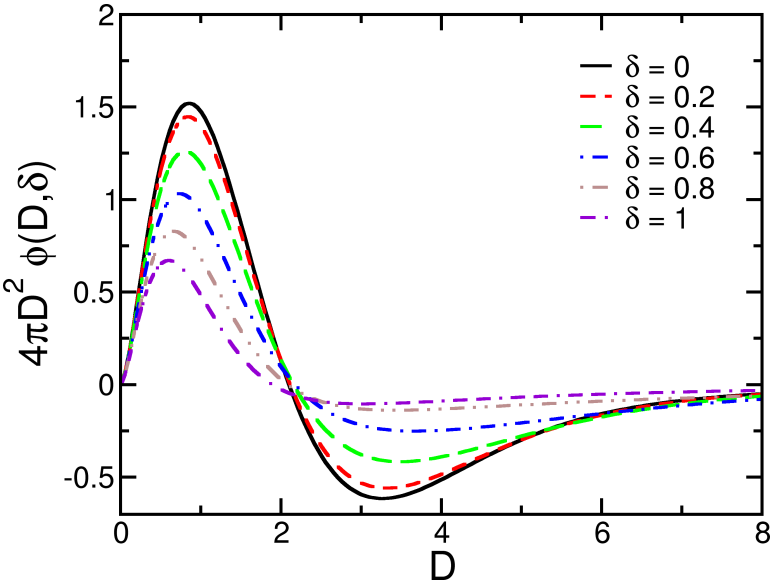

Figure 3.1: The nonlocal correlation kernel ϕ (multiplied by $4\pi D^2$) as a function of D. The variables D and δ are defined by $d = D(1 + \delta)$ and $d' = D(1 - \delta)$.

Approximation for the exchange

The theory of the van der Waals density functional discussed above is an approximation for the correlation energy only. To perform practical calculations, one needs to approximate the exchange energy as well. The standard scheme is to use a GGA for exchange augmented with vdW-DF correlation [10, 71]. However, it is important to choose a GGA flavor whose exchange part does not produce a binding alone, that is not present when the exchange is treated exactly. As discussed in detail in Ref. [71], the exchange part of the Zhang-Yang revPBE [52] is used for numerical calculations. This choice is mainly motivated by the work of Wu *et al.* [73], who have pointed out that PW91 and PBE predict binding in

rare gas dimers from exchange alone, a feature absent for the exact Hartree-Fock exchange. It was found [71] that revPBE does not have this property.

Summarizing, the total exchange-correlation energy in vdW-DF theory is defined as

$$E_{xc}^{vdW-DF} = E_x^{revPBE} + E_c^{LDA} + E_c^{nl}. \tag{3.63}$$

Calculational procedure

The vdW-DF calculational procedure is conducted as follows. In the first step, crystal or molecular structures optimized using PBE are used for producing a self-consistent electron density. In the second step, the nonlocal correlation energy E_c^{nl} is evaluated using this density as the input for the program. In the final step, the vdW-DF total energy is calculated as

$$E^{vdW-DF} = E^{PBE} - E_{xc}^{PBE} + E_{xc}^{vdW-DF}. \tag{3.64}$$

Although the vdW-DF is evaluated in a postprocessing manner in the procedure described above, it has been shown [70] that self-consistency has little effect on the atomic interaction energy and structure at equilibrium distances. On the other hand, this procedure allows a rather quick evaluation of the vdW-DF total energy.

Chapter 4

Implementation of vdW-DF

The main achievement of vdW-DF theory is to express the long-range part of the correlation energy as an integral over interactions between a pair of the electron densities Eq. (3.54). All details of these interactions are enclosed in the kernel function $\phi(\mathbf{r}, \mathbf{r}')$ (3.55). The rather simple expression for the nonlocal correlation energy in the shape of a 6-dimensional integral over a real space, however, requires a very efficient numerical implementation. In this chapter we consider in detail our implementation of vdW-DF which allows us to treat such extended systems as molecular crystals and molecule/metal interfaces successfully.

4.1 Numerical integration

A short introduction to the numerical integration methods is given in this section. Special attention is paid to the efficiency and accuracy of the these methods regarding their application to multidimensional integration.

4.1.1 Numerical quadrature rules

Numerical quadrature rules can be broadly divided in two categories: Formulas, which evaluate the integrand at equally spaced abscissas (Newton-Cotes formulas), and formulas which evaluate the integrand at carefully selected, but non-equally spaced abscissas (Gaussian quadrature rules).

Newton-Cotes type formulas

Formulas which approximate an integral over a finite interval by weighted values of the integrand at equally spaced abscissas are called formulas of the Newton-

Cotes type. The simplest is the trapezoidal rule:

$$\int_{x_0}^{x_0+\Delta x} dx f(x) = \frac{\Delta x}{2}\left[f(x_0) + f(x_0+\Delta x)\right] - \frac{(\Delta x)^3}{12} f''(\xi), \tag{4.1}$$

where $x_0 \leq \xi \leq x_0 + \Delta x$. To approximate an integral over a finite interval $[x_0, x_n]$ with the help of this formula, one needs to divide the interval into n sub-intervals of length Δx and apply the trapezoidal rule to each sub-interval. With the notation $x_j = x_0 + j \cdot \Delta x$, one obtains

$$\int_{x_0}^{x_n} dx f(x) = \frac{x_n - x_0}{n} \sum_{j=0}^{n} w_j f(x_j) - \frac{1}{12}\frac{(x_n - x_0)^3}{n^2} \tilde{f''} \tag{4.2}$$

with $w_0 = w_n = 1/2$ and $w_j = 1$ for $1 \leq j \leq n-1$. The values

$$\tilde{f''} = \frac{1}{n} \sum_{j-1}^{n} f''(\xi_j), \tag{4.3}$$

where ξ_j is a point inside of the corresponding interval $[x_{j-1}, x_j]$. So the last term in Eq. (4.2) introduces an error in the numerical integration. Note that to perform the integration one has to evaluate the function $f(x)$ n times and the error is proportional to $1/n^2$.

An improvement is given by Simpson's rule, which evaluates the function at three points:

$$\int_{x_0}^{x_2} dx f(x) = \frac{\Delta x}{3}\left[f(x_0) + 4f(x_1) + f(x_2)\right] - \frac{(\Delta x)^5}{90} f^{(4)}(\xi). \tag{4.4}$$

This yields

$$\int_{x_0}^{x_n} dx f(x) = \frac{x_n - x_0}{n} \sum_{j=0}^{n} w_j f(x_j) - \frac{1}{180}\frac{(x_n - x_0)^5}{n^4} \tilde{f^{(4)}}, \tag{4.5}$$

where n is an even number, $w_0 = w_n = 1/3$, and for $1 \leq j \leq n$, $w_j = 4/3$ if j is odd and $w_j = 2/3$ if j is even.

In such a way the Newton-Cotes formulas can be derived with further improvement in accuracy. But there are several reasons that prevent this evaluation. Firstly, the more refined a rule is, the more certain we must be that it is applied to a function which is sufficiently smooth. In the formulas above, it is implied that, if the error term is proportional to $f^{(2n)}(\xi)$, the function $f(x)$ is at least $(2n)$-times differentiable and that $f^{(2n)}(x)$ is continuous. Applying the rule to a function which does not satisfy the criteria can lead to a completely wrong error estimation. Secondly, it can be shown if the number of points becomes large, the coefficients of the Newton-Cotes formulas become large and of mixed sign. This may lead to significant numerical cancellation between different terms.

Gaussian quadratures

The Newton-Cotes type rules approximate an integral of a function by the sum of its functional values at a set of equally spaced points, multiplied by appropriately chosen weights. Choosing the weights, one can achieve integration formulas of higher and higher order. Gaussian integration formulas extend this idea and allow to choose weights appropriately together with the possibility to locate the abscissas at which the function is to be evaluated. As mentioned above, a Newton-Cotes type formula, which is based on the evaluation at n points, is exact for polynomials up to degree n (if n is odd) or degree $(n-1)$ (if n is even). Gaussian formulas yield integration rules of degree $(2n-1)$. Furthermore, these rules can be generalized such that they will give exact results for an integrand of the form "special function" times a polynomial up to degree $(2n-1)$.

The main formula of Gaussian quadrature states that if $w(x)$ is a weight function on $[a,b]$, then there are weights w_j and abscissas x_j for $1 \leq j \leq n$ such that

$$\int_a^b dx\ w(x)f(x) = \sum_{j=1}^{n} w_j f(x_j) + \frac{f^{(2n)}(\xi)}{(2n)!} \int_a^b dx\ w(x)[\Pi(x)]^2, \tag{4.6}$$

with

$$\Pi(x) = (x-x_1)(x-x_2)...(x-x_n), \tag{4.7}$$

$$a \leq x_1 \leq x_2 \leq ... \leq x_n \leq b, \qquad a < \xi < b. \tag{4.8}$$

The abscissas are given by zeros of the orthogonal polynomial of degree n associated to the weight function $w(x)$. In order to find them numerically, it is useful to know that they all lie in the interval $[a,b]$. The weights are given by the (weighted) integral over the Lagrange polynomials:

$$w_j = \int_a^b dx\ w(x) l_j^n(x). \tag{4.9}$$

Multi-dimensional integration

The generalization to the multi-dimensional case of quadrature rules described above is straightforward by considering the d-dimensional integral to be an iteration of one-dimensional integrals and applying a one-dimensional integration rule in each iteration. As an example, we consider an integral over the d-dimensional hypercube $[0,1]^d$ evaluated with the help of the trapezoidal rule:

$$\int d^d u\ f(u_1,...,u_d) = \frac{1}{n^d} \sum_{j_1=0}^{n} ... \sum_{j_d=0}^{n} w_{j_1}...w_{j_d} f\left(\frac{j_1}{n},...,\frac{j_d}{n}\right) + O\left(\frac{1}{n^2}\right). \tag{4.10}$$

In total we have to evaluate the function $N = (n+1)^d \approx n^d$ times. Since the necessary computing time is proportional to N we observe that the error scales as $N^{-2/d}$. With increasing dimension d the usefulness of the error bound $O(N^{-2/d})$ declines drastically. Changing, for example, from the trapezoidal rule to Simpsons rule does not change the situation significantly: The error bound would scale in this case as $N^{-4/d}$. We will later see that Monte-Carlo integration yields an error which decreases with $1/\sqrt{N}$, independent of the number of dimensions what makes the Monte-Carlo technique the method of choice for numerical integration in high dimensions.

As a summary, numerical quadrature rules are the best method for low-dimensional integrals. If the integrand is sufficiently smooth and if one knows an absolute bound for a certain derivative of the integrand, they yield an exact error estimate. The efficiency of numerical quadrature rules decreases rapidly with the number of dimensions. Furthermore, for complicated integration boundaries which have to be embedded, for example, into a hypercube, the integrand is no longer a smooth function and the estimate for the error can no longer be used.

More details on numerical quadrature rules can be found in books by Davis et al. [74] and by Press et al. [75].

4.1.2 Monte-Carlo integration

Consider an integral of a function $f(u_1, ..., u_d)$ of d variables $u_1, ..., u_d$ over the unitcube $[0,1]^d$ and assume that f is square-integrable. As a short-hand notation we will denote a point in the unit hypercube by $x = (u_1, ..., u_d)$ and the function evaluated at this point by $f(x) = f(u_1, ..., u_d)$. The Monte-Carlo estimate for the integral

$$I = \int dx f(x) = \int d^d u f(u_1, ..., u_d) \tag{4.11}$$

is given by

$$E = \frac{1}{N} \sum_{n=1}^{N} f(x_n). \tag{4.12}$$

The law of large numbers ensures that the Monte-Carlo estimate converges to the true value of the integral:

$$\lim_{N \to \infty} \frac{1}{N} \sum_{n=1}^{N} f(x_n) = I. \tag{4.13}$$

In order to evaluate the accuracy of the Monte-Carlo estimate, the variance $\sigma^2(f)$ of the function $f(x)$ is introduced:

$$\sigma^2(f) = \int dx (f(x) - I)^2. \tag{4.14}$$

It can be shown that

$$\int dx_1 ... \int dx_N \left(\frac{1}{N} \sum_{n=1}^{N} f(x_n) - I \right)^2 = \frac{\sigma^2(f)}{N}, \tag{4.15}$$

where $\sigma(f)$ is the standard deviation. This equation determines the error of the Monte-Carlo estimate to be $\sigma^2(f)/N$ on average. The central limit theorem says that the probability the Monte-Carlo estimate lies in the range

$$E \in [I - a\sigma(f)/\sqrt{N},\ I + b\sigma(f)/\sqrt{N}]$$

is determined by

$$\lim_{N\to\infty} \text{Prob} \left(-a\frac{\sigma(f)}{\sqrt{N}} \leq \frac{1}{N} \sum_{n=1}^{N} f(x_n) - I \leq b\frac{\sigma(f)}{\sqrt{N}} \right) = \frac{1}{\sqrt{2\pi}} \int_a^b dt \exp\left(-\frac{t^2}{2} \right). \tag{4.16}$$

Thus, the error in a Monte-Carlo integration scheme scales like $1/\sqrt{N}$ independent of the dimension d. In practice, to estimate the value of variance $\sigma^2(f)$ one uses the following formula:

$$S^2 = \frac{1}{N-1} \sum_{n-1}^{N} (f(x_n) - E)^2 = \frac{1}{N} \sum_{n=1}^{N} (f(x_n))^2 - E^2. \tag{4.17}$$

An important point is that Monte-Carlo integration gives only a probabilistic error bound, e.g., it can give a probability that the Monte-Carlo estimate lies within a certain range of the true value.

Summarizing, the error estimate of a Monte-Carlo integration scales like $1/\sqrt{N}$. The main advantage of Monte-Carlo method is that the error estimate is independent on the dimension d. However, the price we pay for this is that the integral converges relatively slowly to the true value. Several techniques exist to improve the situation.

Stratified sampling

Stratified sampling consists of dividing the full integration space into subregions, performing a Monte-Carlo integration in each subregion, and adding up the partial results in the end. Consider a total of n points sampled in a region $r = r_a + r_b$ and $n/2$ points sampled in both r_a and $n/2$ in r_b. In the latter case, the variance is

$$\frac{1}{4} \left(\frac{\sigma_a^2 f}{n/2} + \frac{\sigma_b^2 f}{n/2} \right) = \frac{\sigma_a^2 f + \sigma_b^2 f}{2n}, \tag{4.18}$$

whereas, in the former case, the variance can be written as

$$\frac{\sigma^2 f}{n} = \frac{\sigma_a^2 f + \sigma_b^2 f}{2n} + \frac{(I_a f - I_b f)^2}{4n}. \tag{4.19}$$

As one can easily see this variance is, at best, equal to the former one, and only if the integral values are identical. The optimal reduction of the variance can be shown to occur for $n_a/n_b = \sigma_a f/\sigma_b f$ [75]. In other words, the total variance is minimized when the number of points for Monte-Carlo sampling n_j in each sub-volume is proportional to the variance of the corresponding $\sigma_j f$.

Importance sampling

Importance sampling introduces a weight function into integral:

$$\int dx f(x) = \int dx w(x) \frac{f(x)}{w(x)}, \tag{4.20}$$

with

$$w(x) > 0, \qquad \int dx w(x) = 1. \tag{4.21}$$

The function $w(x)$ has two important requirements: a) one must be able to sample from the distribution $w(x)$, and b) $f(x)/w(x)$ should be "smooth" in the sense that $\sigma_w(f(x)/w(x)) < \sigma f(x)$, i.e. $w(x)$ and $f(x)$ should have the same peak structure. Of course, the ideal choice is known to be $w(x) = |f(x)|/\int dx f(x)$ for which $\sigma_w(f/w) = 0$, but for this choice *a priori* knowledge of the integral value is required.

Adaptive methods

The variance-reducing techniques described above require some advance knowledge of the behavior of the function to be integrated. In many cases this information is not available, and one prefers adaptive techniques in which an algorithm learns the function as it proceeds.

One of the most famous adaptive algorithms is VEGAS [75]. VEGAS combines the basic ideas of importance and stratified sampling into an iterative algorithm which automatically concentrates evaluation of the integrand in those regions where the integrand is largest in magnitude.

Another simple but efficient iterative adaptive scheme is globally adaptive subdivision. This scheme is based on the possibility of error estimation of the integral. First, the integral and its error estimate is evaluated in the entire region. This error is compared with the required accuracy. If the error is higher than the accuracy, the integration region is subdivided, and each subregion is integrated separately. The new value of the integral and error estimate is evaluated and compared with the accuracy. If the error is not satisfactory, the region with the largest error is subdivided. This loop is continued until the required accuracy is achieved.

Quasi-Monte-Carlo methods

As mentioned previously, a major drawback of the Monte-Carlo method with pseudo-random numbers is given by the fact that the error term scales only as $1/\sqrt{N}$. This is an inherent problem of methods based on random numbers. However, in Monte-Carlo integration the true randomness of the generated numbers is not so relevant. It is more important to sample the integration region as uniform as possible. This leads to the idea of choosing the points deterministically in such a way as to minimize the integration error. And indeed, a Monte-Carlo algorithm based on these quasi-random sequences typically achieves convergence rates of $O(\log^{d-1} n/n)$ rather than the usual $1/\sqrt{N}$ for pseudo-random numbers. More detail about quasi-random numbers and their implementation can be found in [76, 77].

4.1.3 Implementation details

Here we proceed with a description of the implementation details of the program written to evaluate the 6-dimensional integral (3.54).

To calculate nonlocal correlation energy, as one can see from formula (3.54), we only need information about the electron density distribution. Thereby it is straightforward to write a subroutine that performs an integration and uses it with existing ab-initio DFT codes.

The three-dimensional total electron density distribution is read by the subroutine from an input file in a format convenient for visualization with the XcrySDen program [78]. This input file can be generated by many codes (QUANTUM-ESPRESSO, ABINIT, VASP etc.) by specifying a corresponding flag for an output 3-d density format.

The density gradients required by Eq. (3.51) are computed numerically based on the input density. For this, the simple three-point estimation method is used. The kernel $\phi(D, \delta)$ (Fig. 3.1) has been calculated numerically and tabulated on the fine grid (400×21) in the range $D \in [0.01, 19.96]$ and $\delta \in [0, 1]$. The starting value for $D = 0.01$ is connected with the divergence of the kernel function ϕ at small D. For the values $D < 0.01$, $\phi = \phi(D = 0.01)$ is assumed. It has been checked that this approximation has no influence on the final value of the integral. For the values $D > 19.96$, the asymptotic form of Eq. (3.62) is used. Specifics of the Monte-Carlo integration requires calculations of the integrand at random points. Therefore, we use trilinear interpolation [79] for the values of the kernel function and densities.

The vdW-DF program is written in Fortran as an external routine. The quasi-random Korobov [80] sequences are used to achieve higher convergence rates of the Monte-Carlo algorithm. The main parameter required for a Monte-Carlo

integration which should, consequently, be specified is a requested accuracy of final result. The requested accuracy, which serves as the stopping criterion of the integration, can be either relative or absolute, i.e. the integrator tries to find an estimate $\hat{I}$ for the integral I which fulfills $|\hat{I} - I| \leq \max(\epsilon_{abs}, \epsilon_{rel} I)$.

Cuba library

The heart of the subroutine is a CUBA library for multidimensional integration [81][1]. The CUBA library provides new implementation of four general-purpose multidimensional integration algorithms: VEGAS, SUAVE, DIVONNE, and CUHRE. This library is written in C and has interfaces for Fortran, C/C++, and Mathematica. We have chosen the routine DIVONNE, which showed the best results in accuracy, stability and evaluation timing.

DIVONNE is a significantly extended version of CERNlibs's Algorithm D151 [82]. It is essentially a Monte-Carlo algorithm but has additional cubature rules built in for comparison. Variance reduction is conducted by stratified sampling, which is aided by methods from numerical optimization. DIVONNE has a three-phase algorithm: In the first phase, the integration region is split into subregions of (approximately) equal spread s, defined as

$$s(r) = \frac{vol(r)}{2} \left(\max_{x \in r} f(x) - \min_{x \in r} f(x) \right). \tag{4.22}$$

The minimum and maximum of each subregion are sought using methods from numerical optimization (a quasi-Newton search). Then "dividers" are moved around to find an optimal splitting. This latter procedure is translated into a solution of a linear system and is, hence, quite fast [82]. In the second phase, the subregions determined in the previous step are independently sampled with the same number of points each. The latter is extrapolated from the results of the previous phase. In the last phase, regions whose results from the first and second phase do not agree within their errors are subdivided or sampled again.

In addition, DIVONNE has the possibility to specify the location of possible peaks, if such are known from analytical considerations. The idea here is to help the integrator find the extrema of the integrand, since narrow peaks are a particular challenge for the algorithm. Even if only the approximate location is known, this feature of suggesting the integrator can easily cut an order of magnitude out of the number of samples needed to reach required accuracy for complicated integrands. There is also the possibility to specify the method to obtain the integrand estimate: a Korobov [80] or Sobol [77] quasi-random sample of given size, a Mersenne-Twister [83] pseudorandom sampling of given size, and the cubature rules of Genz and Malik [84].

[1] http://www.feynarts.de/cuba/

4.2 Test systems

The implemented program has been applied to several "benchmark" vdW systems such as the Ar dimer, the benzene dimer, and graphite. We test both reliability and computational efficiency of the code comparing the results for the interaction energies with those reported in literature. All these tests have been carried out using the QUANTUM-ESPRESSO code [85] utilizing ultrasoft pseudo-potentials. The self-consistently calculated with PBE electron density is used to obtain E_c^{nl}, as well as the other energy contributions, namely, revPBE$_\mathrm{x}$ + LDA$_\mathrm{c}$ in a post-processing manner.

At the end of this section, numerical tests are presented regarding the calculation of the nonlocal vdW energies of organic crystals and organic/metal interfaces.

4.2.1 Argon dimer

One of the most prominent systems, where standard exchange-correlation functionals fail, is the Ar dimer. Since the Ar atom has a fully occupied 3p shell, the binding in the dimer is purely due to dispersion forces. Self-consistent calculations were performed putting two Ar atoms in a supercell with the cell size of 30 au. A plane-wave cutoff of 60 Ry and was chosen.

We first consider the convergence of E_c^{nl} by choosing different values for the parameter ϵ which governs the accuracy of the Monte-Carlo (MC) integration (see Section 4.1.3). The results are presented in Fig. 4.1 and Table 4.1. Therein, also the information is included about time which is required for the calculation of E_c^{nl} on a desktop machine with an Opteron processor. In addition, the number of the integrand evaluations is presented for comparison with the total number of evaluations which would be required when using a quadrature rule:

$$N_{eval}^{tot} = n_{cell}\ (N_x \cdot N_y \cdot N_z)^2, \tag{4.23}$$

where n_{cell} denotes the number of unit cells representing a crystal ($n_{cell} = 1$ for the case of isolated molecules). N_x, N_x, and N_z are the numbers of points in a corresponding direction as determined by the real space grid, where the electron density is defined. In the case of the Ar dimer example, we use the grid of 150 points in each direction, so the maximal number of calculations is of the order 10^{13}. Hence, directly applying the quadrature rule for this grid, the evaluation of the integral would take several orders of magnitudes of computing time longer than the MC method.

Fig. 4.1 shows the nonlocal interaction energy for the Ar dimer as a function of the interatomic distance for different parameters ϵ governing the accuracy of the Monte-Carlo integration. It turns out that a value of $\epsilon = 10^{-5}$ Ha is sufficient to obtain converged results. The behavior of the curve for $\epsilon = 10^{-4}$

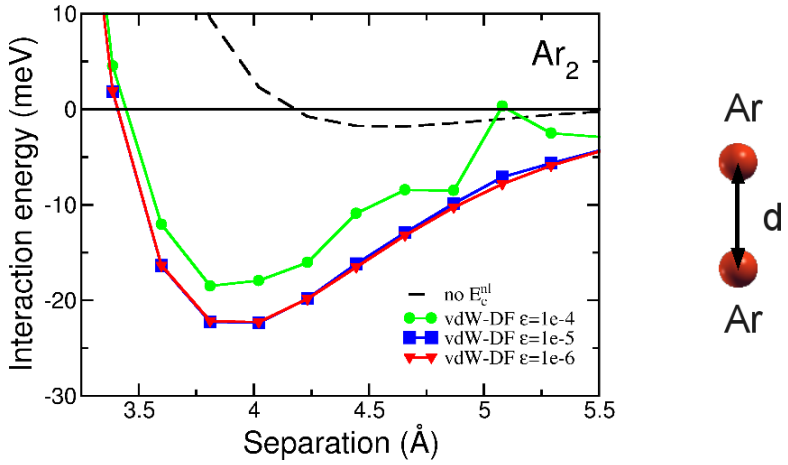

Figure 4.1: Nonlocal interaction energy for the Ar dimer as a function of the interatomic distance for different parameters governing the accuracy of the Monte-Carlo integration.

ϵ [Ha]	Time	E_c^{nl} [Ha]	N_{eval}
10^{-4}	1min 48s	0.18098870	$0.8{\cdot}10^{8}$
10^{-5}	8min 41s	0.18097679	$0.4{\cdot}10^{9}$
10^{-6}	84min 55s	0.18097998	$0.2{\cdot}10^{10}$

Table 4.1: Convergence of the nonlocal correlation energy E_c^{nl} of the Ar dimer as a function of the parameter ϵ governing the accuracy in the integration. The total integration time and actual number of integrand evaluations are included (N_{eval}).

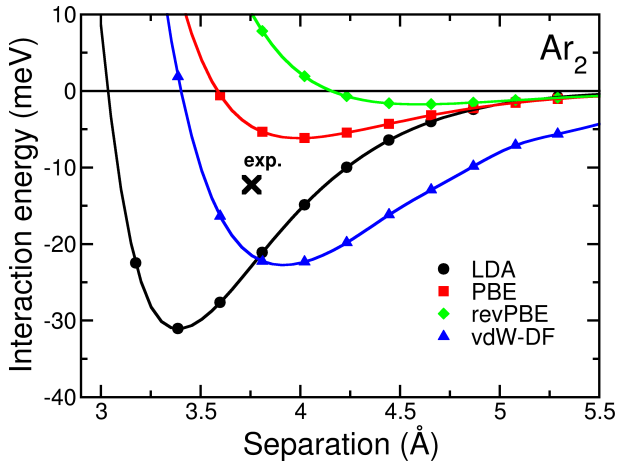

Figure 4.2: Interaction energy of Ar dimer as a function of separation for different types of exchange-correlation potentials.

is rather interesting. One can see that for small separation distances the results are almost the same as for $\epsilon = 10^{-5}$, with the difference being about 5 meV at the minimum energy. The biggest deviations, and even oscillations, are present at bigger separations, where the values of the integrand become smaller than the requested accuracy. Therefore, they are not considered by the MC algorithm described in Section 4.1.3. On the other hand, the time required for this level of accuracy is roughly four times less than for $\epsilon = 10^{-5}$, and hence it can be used for getting a quick estimation of the binding energy. In particular, the region around the energy minimum is sampled quite reliably already, since the oscillatory behavior usually only appears far from it. Cross-checking our results for the argon dimer shows perfect agreement with the corresponding curves from published works, e.g., Fig. 2 of Ref. [10] and Fig. 2 of Ref. [70].

Now we can proceed to the discussion of the role of the exchange-correlation potentials (Fig. 4.2) for the binding properties of such a van der Waals system. LDA heavily overestimates the binding, giving an as much as three times too large binding energy, and consequently a too small equilibrium distance. In contrast to LDA, PBE gives a too small interaction energy and a bigger equilibrium distance than experimentally determined, whereas revPBE produces even worse results. The vdW-DF results are also far from perfect. One can see only slight improvement of the equilibrium distance in comparison with PBE, whereas the predicted interaction energy is twice as large as the experimental value. This behavior of the vdW-DF has been discussed in literature [10, 70, 71] and attributed to the form of the exchange part. Regardless of remaining discrepancies, the most important point is that the addition of the nonlocal contribution E_c^{nl} dramatically improves the description of this vdW system.

4.2.2 Benzene dimer

The next test system is a benzene dimer in a top-parallel configuration. Following the same procedure as described above, we calculate the vdW-DF interaction energy and compare it with that obtained using different exchange-correlation potentials (Fig. 4.3). An energy cutoff of 35 Ry and a cubic supercell box of 15 Å length is used for the self-consistent calculations. For the Monte-Carlo integration, the accuracy parameter of $\epsilon = 10^{-4}$ Ha is found to be sufficient to produce convergent values of E_c^{nl}. The average calculation time corresponding per run to achieve the required accuracy is about 15 min on an Opteron processor.

Detailed discussion of the application of vdW-DF to different benzene dimers and a comparison with other methods was provided in Ref. [15]. Here it can be stressed that the actual results are completely consistent with those of Ref. [15]. The comparison with other xc potentials shows again the superiority of the vdW-DF that predicts the binding energies and equilibrium distances close to those

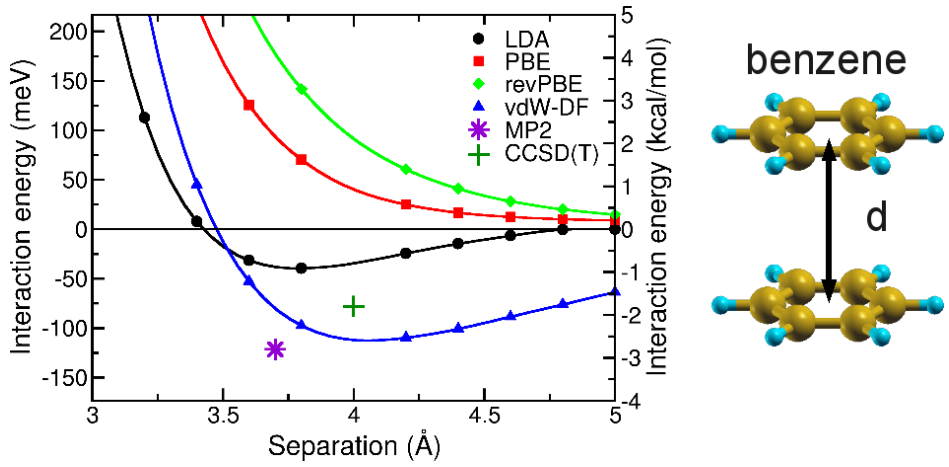

Figure 4.3: The interaction energy of two benzene molecules in atop-parallel configuration as function of separation for different types of exchange-correlation potentials. MP2 and CCSD(T) values estimated from Ref. [86].

given by wave-function based methods such as Møller-Plesset theory (MP2) and coupled-cluster theory [CCSD(T)] [15].

4.2.3 Graphite

Another typical vdW system is graphite, where graphene sheets are weakly bound along the **c**-direction. Graphite is a particular example, being a simple vdW-bound extended system. It is especially interesting for this work since we will apply vdW-DF theory to the description of carbon-based bulk crystals and their surfaces.

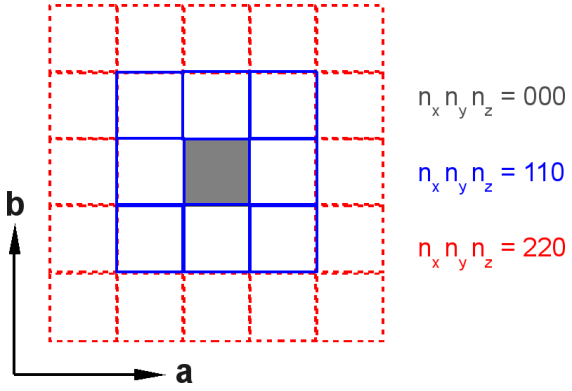

Figure 4.4: The sketch demonstrates how a supercell is constructed to calculate the nonlocal energy for a periodic crystal. n_x n_y n_z label the number of translational images along the three lattice vectors.

For the self-consistent calculations, an energy cutoff of 35 Ry and a $4 \times 4 \times 4$ k mesh is chosen. The experimental lattice parameter of $a = 2.4612$ Å is used, while the interplane distance is varied. The task now is to evaluate E_c^{nl} considering contributions not only from inside one unit cell, but from all pairs of points where one is located in the original unit cell and the other one somewhere in the crystal. To this extent, a supercell is created as shown in Fig. 4.4. In practice, one has to check the convergence of the nonlocal energy with respect to an interaction distance which obviously goes far beyond one unit cell size. Thereby the convergence of E_c^{nl} with respect to the number of translational images has to be monitored. The results are presented in Table 4.2. In the table n_x, n_y, n_z denote the number of translational images along the three lattice vectors that corresponds to $n_{cell} = (2n_x + 1)(2n_y + 1)(2n_z + 1)$.

For the calculation of E_c^{nl} we used an accuracy parameter $\epsilon = 10^{-4}$ Ha, which gives the integral within an accuracy of about 1 meV. One can see that there is almost no dependence of the calculation time on the number of translational images higher than the 110 set. This demonstrates the efficiency of the chosen integration scheme for dealing with periodic systems. The results for the binding energy in graphite, which we define as the energy required to split a graphite crystal into separated graphene sheets, are given in Fig. 4.5.

The results for graphite are consistent with those previously reported (e.g., Fig. 2 of Ref. [17]). The only distinction is that here the interaction energy is calculated not just between two graphene layers but for the graphite crystal, i.e. corresponds to the cohesive energy of "graphene in graphite". As a consequence, the curve presented here has a deeper minimum than that in Ref. [17] but the same equilibrium distance. The behavior of the binding energy for different exchange-correlation potentials is, in general, the same as in the previous model vdW systems: LDA predicts reasonable equilibrium distance but underestimates the binding energy as much as by a factor of two; all GGA flavors fail, giving almost no binding and leading to distances as much as two times larger than in experiment. In contrast to standard xc potentials, the vdW-DF produces results in reasonable agreement

n_x n_y n_z	E_c^{nl} [Ha]	CPU time
000	0.19687	1min 31s
110	0.12717	2min 48s
220	0.12332	2min 56s
330	0.12284	3min 07s
440	0.12268	2min 53s
550	0.12261	3min 28s

Table 4.2: Convergence of the nonlocal correlation energy E_c^{nl} of graphite with respect to the number of translational images.

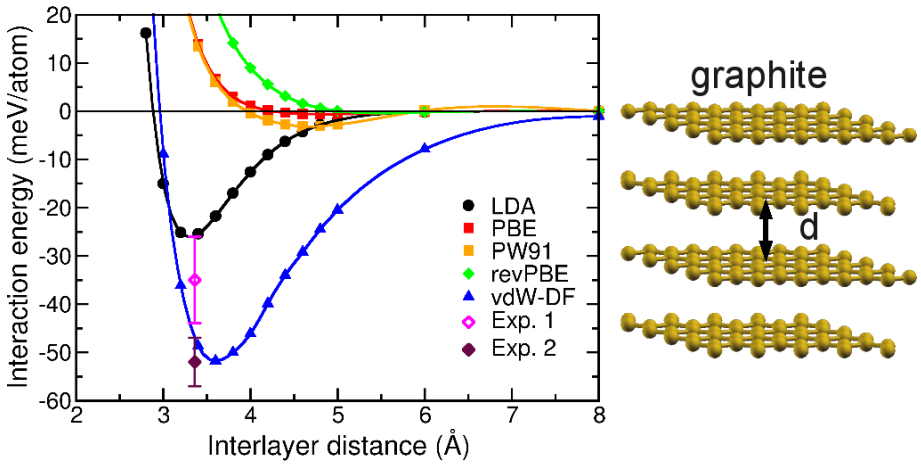

Figure 4.5: Binding energy of graphene sheets in the graphite crystal as a function of inter-layer separation. For comparison, the results for different exchange-correlation potentials and experimental data Exp. 1 [87] and Exp. 2 [88] are also included.

with experiment for both the binding energy and the equilibrium layer separation. All these findings together with the computational efficiency of vdW-DF open the possibility to handle more challenging systems such as molecular solids.

4.2.4 Other tests

To give the reader an idea about the computational complexity of the vdW-DF calculations applied to molecular crystals and organic molecule/metal interfaces to be discussed in the next chapters, an overview is provided below, regarding the convergence of the results and the corresponding computing times.

First, the nonlocal energy and the corresponding contribution to the molecular cohesive energy of naphthalene are examined. The results for different levels of accuracy in the integration, determined by the parameter ϵ, are summarized in Table 4.3. One can see that an accuracy level achieved by $\epsilon = 10^{-3}$ Ha is sufficient to obtain convergent values of the cohesive energy to within 5 meV, which takes only around 5 min on an Opteron desktop machine. The computational time increases exponentially with the integration accuracy. Thus, very small values of ϵ can lead to a waste of computer power[2].

The next test dedicated to the convergence with the number of periodical images (Table 4.4). The results of this test show rather fast convergence of the nonlocal energy with the integration volume. The integration carried out in Eq. (3.54) over the crystal volume by considering the nonlocal interactions up to the next nearest neighboring unit cell in all three dimensions ($n_x\ n_y\ n_z = 222$, corresponding to

[2]Moreover, one could expect numerical instabilities in this case.

	Isolated molecule		Crystal ($n_x\ n_y\ n_z = 1\ 1\ 1$)		
ϵ [Ha]	E_c^{nl} [Ha]	CPU time	E_c^{nl} [Ha]	CPU time	E_{coh}^{nl} [eV]
10^{-1}	0.23495	0 min 4 sec	0.42441	0 min 9 sec	6.4541
10^{-2}	0.44949	0 min 49 sec	0.77901	1 min 4 sec	1.6316
10^{-3}	0.46030	1 min 47 sec	0.80778	4 min 58 sec	1.5344
10^{-4}	0.46214	13 min 58 sec	0.81107	26 min 3 sec	1.5397
10^{-5}	0.46227	54 min 30 sec	0.81140	264 min 26 sec	1.5389

Table 4.3: The nonlocal correlation energy E_c^{nl} and the corresponding contribution to the cohesive energy, E_{coh}^{nl}, of 2A for different levels of accuracy of the integration, which is determined by the parameter ϵ. The corresponding data for the isolated 2A molecule are also included. The CPU times refer to a desktop machine using a single Opteron processor. n_x, n_y, n_z denote the numbers of the periodical images taken into account in the evaluations of E_c^{nl}.

	$\epsilon = 10^{-3}$ Ha			$\epsilon = 10^{-4}$ Ha		
$n_x\ n_y\ n_z$	E_c^{nl} [Ha]	Time	E_{coh}^{nl} [eV]	E_c^{nl} [Ha]	Time	E_{coh}^{nl} [eV]
0 0 0	1.04563	3 min 22 sec	-1.7005	1.04696	20 min 3 sec	-1.6685
1 1 1	0.80778	4 min 58 sec	1.5344	0.81107	26 min 3 sec	1.5397
2 2 2	0.80783	4 min 46 sec	1.5336	0.80982	24 min 26 sec	1.5568
3 3 3	0.80592	5 min 5 sec	1.5596	0.80958	26 min 11 sec	1.5599
4 4 4	0.80763	4 min 41 sec	1.5364	0.80972	25 min 0 sec	1.5580
5 5 5	0.80648	4 min 38 sec	1.5520	0.80966	24 min 12 sec	1.5588

Table 4.4: The nonlocal correlation energy E_c^{nl} and the corresponding contribution to the cohesive energy E_{coh}^{nl} of the 2A crystal with respect to the number of translational images. The CPU times refer to a desktop machine using a single Opteron processor.

a doubling of the unit cell in each direction) is sufficient to produce the cohesive energy within 2 meV. As in the case of graphite, there is almost no dependence of the computing time on the volume size due to the very efficient algorithm used in the DIVONNE subroutine to divide the integration area into subregions and treat only the ones that contribute the most to the integral within a required integration accuracy. It is also interesting to note that the characteristic fluctuations of the values (see, e.g., the third column of Table 4.4) are of the order of the requested integration accuracy. This has already been shown for the Ar dimer and is typical for the MC integration scheme.

In general, our implementation has been found to be very efficient for the treatment of molecular crystals. The situation is more complicated for another test system consisting of a 1T molecule on top of the Cu(110) surface. We consider

ϵ [Ha]	E_c^{nl} [Ha]	CPU time	E_{ads}^{nl} [eV]
10^{-1}	2.73533	0 min 45 sec	7.8361
10^{-2}	3.54851	4 min 30 sec	0.6359
10^{-3}	3.59613	21 min 54 sec	-0.1178
10^{-4}	3.60104	174 min 9 sec	-0.0668
10^{-5}	3.60120	1340 min 27 sec	-0.0622

Table 4.5: The nonlocal correlation energy E_c^{nl} and the corresponding contribution to the adsorption energy E_{ads}^{nl} of the 1T molecule on the Cu(110) surface with respect to the integration accuracy parameter ϵ. The CPU times refer to a desktop machine using a single Opteron processor. The integration volume is confined to one unit cell only ($n_x\ n_y\ n_z = 000$ in our denotation).

a configuration (Fig. 6.1), where the molecule - metal distance is 4.9 Å. An accuracy parameter of 10^{-4} is required to obtain convergent values of the nonlocal energy and hence the nonlocal contribution to the adsorption energy E_{ads}^{nl} (see Table 4.5). The interaction is also more long-ranged, requiring more translational images to achieve convergence with respect to the integration volume (Table 4.6). A reliable combination is found to be $n_x\ n_y\ n_z = 440$.

$n_x\ n_y\ n_z$	E_{nl} [Ha]	CPU time	E_{ads}^{nl} [eV]
0 0 0	3.59613	21 min 54 sec	-0.1178
1 1 0	3.17768	28 min 59 sec	0.0869
2 2 0	3.17640	26 min 2 sec	-0.1229
3 3 0	3.17430	26 min 44 sec	-0.1165
4 4 0	3.17511	26 min 58 sec	-0.0990
5 5 0	3.17576	31 min 26 sec	-0.0979

Table 4.6: The nonlocal correlation energy E_c^{nl} and the corresponding contribution to the adsorption energy E_{coh}^{nl} of 1T on Cu(110) with respect to the number of translational images. The CPU times refer to a desktop machine using a single Opteron processor. The integration accuracy $\epsilon = 10^{-3}$ Ha has been used.

Chapter 5

Cohesive and surface energies of organic crystals

5.1 Introduction

The charge transport characteristics of electronic devices based on organic semiconductors strongly depend on the thin film morphologies. A high level of purity and order is required to achieve the highest values of electron and hole mobilities. Therefore, considerable experimental effort has been put into the investigation of the conditions of controlled organic thin film growth [89–91].

Ideally, one is looking for defect-free layer-by-layer growth with a desired orientation of the molecules on a substrate. Key parameters for understanding growth mechanisms are diffusion barriers and surface energies, which are, however, experimentally difficult to access. Hence, support from the theoretical side is needed to give an insight into the energetics governing intermolecular and molecule/substrate interactions. However, a reliable treatment on an *ab-initio* level has remained problematic. The computational complexity of first-principles methods connected with the large number of atoms for these molecular crystals is one of the main obstacles for efficient simulations. Moreover, the binding in molecular crystals is mainly due to weak van der Waals interactions that could not be treated by any standard approaches for the exchange-correlation energy. While LDA and GGA pose no severe restriction when exploring the electronic and optical properties of organic semiconductors at their experimental lattice constants [31, 92, 93], an *ab-initio* treatment of intermolecular binding has been completely absent so far.

It has only recently become possible to incorporate nonlocal dispersion forces into a DFT framework [10] as described in Chapter 3. This van der Waals density functional has proven to yield reliable binding energies for a variety of systems

(for a review see, e.g., Ref. [13]). In view of these results, the investigation of the organic crystals' energetics has come into reach.

5.2 Theoretical approaches

Computational details

All ab-initio calculations are performed with the plane-wave package QUANTUM-ESPRESSO [85] utilizing ultrasoft pseudo-potentials [94]. A plane-wave energy cutoff of 40 Ry has been proven sufficient to produce converged results for cohesive energies within 1 meV and total forces within 0.5 mRy/au. For Brillouin zone integrations, the Monkhorst-Pack scheme [95] with a 3×3×2 mesh is employed. Different types of the exchange-correlation potential are used, which are the LDA [96] and two types of the generalized gradient approximation, i.e. PBE [50] and revPBE [52]. In addition, two methods that treat the vdW interactions are explored. One is the nonlocal van der Waals density functional [10] and the other is the semiempirical vdW correction by Grimme [8, 66]. The methodology and implementation of both methods are described in details in Chapter 3 and Chapter 4.

Cohesive energy

The cohesive energy is an important quantity for the characterization of the bulk phase. In molecular crystals, the cohesive energy, E_{coh}, is defined as the energy gain upon formation of a crystal from isolated molecules. This quantity can be easily measured experimentally and evaluated theoretically.

The molecular cohesive energy is defined by the expression

$$E_{coh} = E_{mol} - E_{bulk}/n, \tag{5.1}$$

where E_{mol} and E_{bulk} denote the total energies of the isolated molecule and the molecular crystal, respectively. Thereby, the bulk energy is computed by adopting the experimentally known space groups and lattice constants. The divisor n takes into account the number of molecules in the unit cell. By this definition the cohesive energy is positive for any stable crystal. To calculate the total energy of the isolated molecule, E_{mol}, the supercell approach is used (Fig. 5.1, left). The molecule is put in a box of sufficient size to avoid interaction between translational images.

Experimentally, E_{coh} can be extracted from phase transformation properties, such as the melting temperature, enthalpy of sublimation or evaporation, and thermal desorption measurements. In this work, the available experimental cohesive energies are estimated using a compendium of sublimation enthalpies ΔH_s of organic

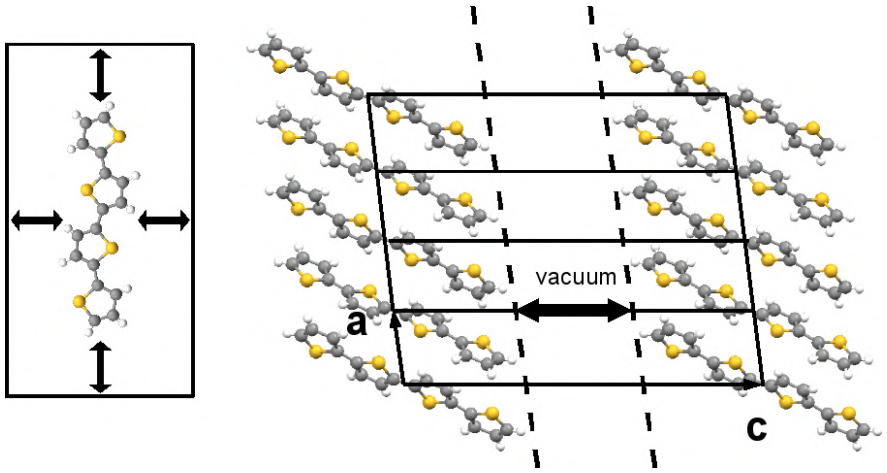

Figure 5.1: Supercell (left) and slab geometry (right) for treating an isolated molecule and a surface in 3D periodical conditions.

compounds reported in Ref. [97]. The enthalpy of sublimation, or heat of sublimation, is defined as the energy required to sublime one mole of the substance at a given combination of temperature and pressure. The cohesive energy is equal to the enthalpy of sublimation at 0 K. To estimate this quantity we make use of the following relation [98]:

$$E_{coh} \approx \Delta H_s + 2RT, \tag{5.2}$$

where the term $2RT$ accounts for the difference between the gas phase enthalpy of an ideal gas, $pV + 3RT$, and the estimated vibrational contribution to the crystal enthalpy ($6RT$). One should note that this estimation is valid only for molecules which are sufficiently rigid.

Surface energy

By definition, the surface energy is the work required to cleave a bulk crystal in a given direction per unit area of the newly created surface. Surface energies are calculated with the repeated slab approach (Fig. 5.1, right). In this approach, surfaces are simulated by slabs that preserve two dimensional crystalline periodicity in the plane given by the Miller index (hkl) and are separated by vacuum perpendicular to it. Again, the vacuum distance is chosen large enough to remove all interactions between the periodically repeated layers.

Thus, the surface energy is determined as

$$\gamma = \frac{1}{2A}(E_{slab} - E_{bulk}). \tag{5.3}$$

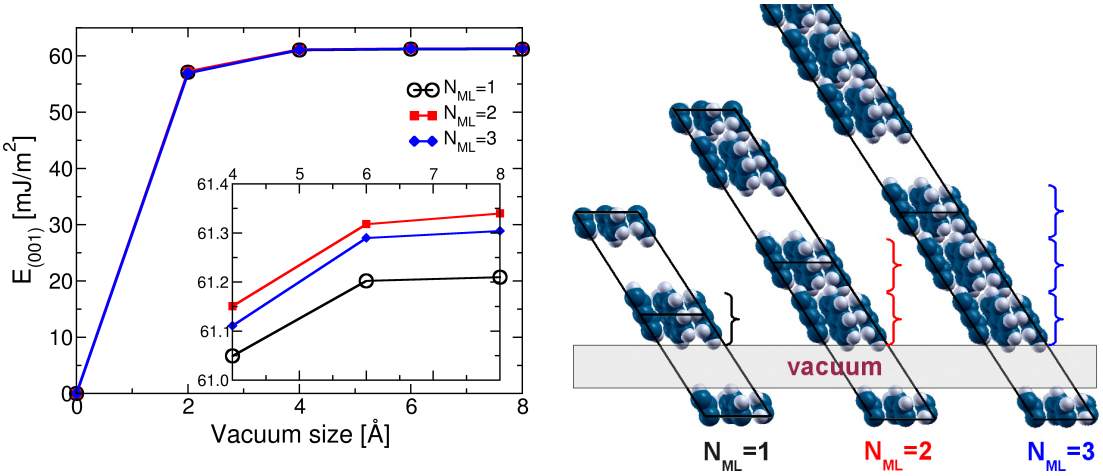

Figure 5.2: The naphthalene (2A) (001) surface energy as a function of vacuum separation for different slab thicknesses calculated within the LDA. N_{ML} stands for the number of molecular layers and defines the thickness of the slab. The inset shows the same data with an expanded energy axis.

Here, the factor 1/2 takes into account the fact that the slab contains two surfaces. E_{slab} denotes the total energy of the slab configuration and A is the surface area.

Besides the vacuum separation, another important parameter is the thickness of the slab which mimics the semiinfinite crystal. In the case of molecular crystals this parameter cannot be chosen in terms of atomic layers used for inorganic materials but as an integer number of molecular layers. The (001) surface is special as it represents a standing orientation of the molecules within a layer. The corresponding surface energy of naphtalene as a function of the vacuum separation is plotted in Fig. 5.2 for different slab thicknesses. Since the behavior does not depend on the underlying xc functional, the LDA results are displayed. Later it will be shown that the (001) surface energy is minimal for all series of rod-like molecules under investigations. The respectively weak interaction between the slabs in this direction leads to a rather sharp convergence of the surface energies as a function of thickness and vacuum distance. Similar tests performed for other low-index planes have revealed that only one molecular layer and the vacuum size of 8 Å are adequate for surface energy convergence to within 1 mJ/m^2.

Equilibrium shape of crystals

When considering the equilibrium of a small crystal with the ambient phase (vapor, solution or melt) there exists a shape which is most favorable from a thermodynamic point of view in the sense that the work of formation is minimal for a given crystal volume. The work of formation of a crystal consists of two

parts: The first one is a volume contribution $(P_c - P_v)V_c = n(\mu_v - \mu_c)$, which is gained when transferring n atoms or molecules from the ambient (vapor) phase with chemical potential μ_v to the crystal phase with lower bulk chemical potential μ_c when the crystalline phase is the stable one ($\mu_c < \mu_v$). The second part γS is due to the formation of a new phase-dividing surface, where γ is the work spent to create a unit area of a new surface or, in other words, the surface free energy. The volume part depends only on the volume of the crystal or on the number of atoms transferred. At constant volume, the surface part only depends on the crystal shape. Thus, the condition for the minimum Gibbs free energy change connected with the crystal formation at a constant volume, which determines the equilibrium shape, is reduced to the minimum of the surface energy. The equilibrium shape of a liquid droplet is evidently a sphere. The case of a crystal is more complicated since it is confined by the crystal faces with different crystallographic orientations with their specific surface energies.

Consider first the case of a crystal in a three-dimensional homogeneous medium (vapour, solution or melt). The general condition for the equilibrium of a single crystal is the minimum of the Helmholz free energy at constant temperature and volume [99]:

$$dF = 0,\ dV = 0. \tag{5.4}$$

Assume that the crystal is a polyhedron confined by a limited number of different crystal faces with areas S_n and corresponding surface energies γ_n. The equilibrium condition (5.4) is then

$$dF = -P_v dV_v - P_c dV_c + \sum_n \gamma_n dS_n = 0, \tag{5.5}$$

where P_c is the inner pressure of the crystal, P_v is the pressure of the vapor phase, and V_v and V_c are the volumes of the vapor phase and the crystal, respectively. Taking into account $V = V_v + V_c = \text{const}$, i.e. $dV_v = -dV_c$, the above equation is reduced to

$$dF = -(P_c - P_v)dV_c + \sum_n \gamma_n dS_n = 0. \tag{5.6}$$

The crystal volume can be considered as a sum of the volumes of pyramids constructed on the crystal faces with a common apex at an arbitrary point within the crystal. Then

$$V_c = \frac{1}{3}\sum_n h_n S_n,$$

and

$$dV_c = \frac{1}{3}\sum_n (S_n dh_n + h_n dS_n),$$

where h_n are the heights of the pyramids. Thus, the change of the volume with accuracy to infinitesimals of second order is equal to the shift of the surfaces S_n

by a distance dh_n, so that

$$dV_c = \sum_n S_n dh_n.$$

Combining the last two equations gives

$$dV_c = \frac{1}{2}\sum_n h_n dS_n. \tag{5.7}$$

Substituting (5.7) in (5.6) results in

$$\sum_n \left[\gamma_n - \frac{1}{2}(P_c - P_v)h_n\right] dS_n = 0.$$

As the changes dS_n are independent from each other, every term in the brackets is equal to zero and

$$P_c - P_v = 2\frac{\gamma_n}{h_n}.$$

The difference $P_c - P_v$ does not depend on the crystallographic orientation, and, for the equilibrium shape, one obtains

$$\frac{\gamma_n}{h_n} = const. \tag{5.8}$$

The relationship (5.8) expresses the geometrical interpretation known as *Wulff's construction* or *Gibbs-Curie-Wulff's theorem*. It states that in equilibrium the distances of the crystal faces from a point within a crystal (called a Wulff's point) are proportional to the corresponding surface energies of these faces. According to this rule the equilibrium shape of the crystal can be constructed by the following procedure. First, vectors normal to all possible crystallographic faces from an arbitrary point are drawn. Then, the distances proportional to the corresponding surface energies are measured on these vectors, where the corresponding normal plane is constructed. The resulting closed polyhedron is the equilibrium crystal shape. Only crystal faces with the lowest surface energies contribute to it.

5.3 Results

5.3.1 Cohesive energies

The cohesive properties of the molecular crystals available in literature were performed mainly within the framework of empirical force-fields methods. The ab-initio study for anthracene and pentacene [100] using LDA resulted in reasonable agreement with experiment, i.e. reproducing the right order of magnitude.

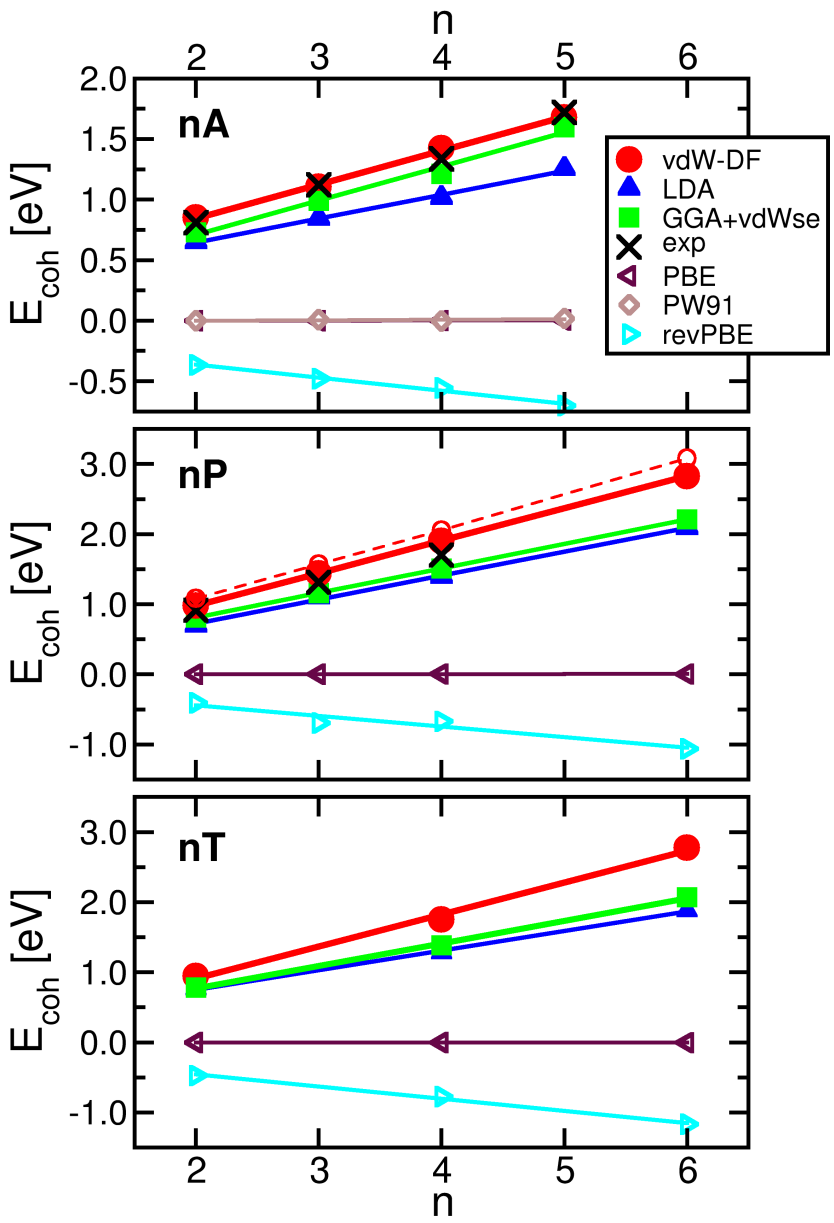

Figure 5.3: Calculated cohesive energies of the oligoacenes nA (top), the oligophenylenes nP (middle), and the oligothiophenes nT (bottom) as function of the oligomer length for different types of the exchange-correlation potential: LDA, different flavors of GGA (PBE, revPBE, and PW91), vdW-DF and a semiempirical vdW correction are compared with available experimental data [97]. The lines are guides to the eye. For the nP oligomers, the open circles represent the values obtained when the isolated molecules are held to be planar.

Here, the cohesive energies for three oligomer series are calculated using different types of exchange-correlation potentials and methods for treating the vdW interactions. In Fig. 5.3 the results are presented together with available experimental values estimated from the enthalpy of sublimation using Eq. (5.2).

Let us first consider the results given by the standard, i.e local or semilocal, exchange-correlation density functionals. One can see that the LDA generally underestimates cohesive energies by as much as 25%. This discrepancy is not surprising, since LDA relies on the wrong physical picture. Only through its general overbinding effect does it mimic a compensation for the missing dispersion interactions. It is noteworthy that GGA completely fails in describing the cohesive properties of these compounds. The observed values are almost zero for PBE and PW91 and even negative when the *revised* version of PBE (revPBE) is used. Thus, although LDA and GGA reveal reliable results for intermolecular conformations for fixed lattice parameters [101, 102] (we will also see this in Chapter 8), these local and semilocal functionals break down when it comes to intermolecular bonding.

In contrast to the standard exchange-correlation potentials, the usage of the new vdW-DF functional gives cohesive energies in excellent agreement with experiment. The cohesive energies for all series are almost linear functions of the oligomer length, which appears to be reasonable owing to the same type of crystalline packing. Since there is no experimental data available for the oligothiophenes, the theoretical values can be viewed as an accurate theoretical prediction. Relating the cohesive energy to the number of carbon atoms per molecule, one finds very similar values for acenes (85, 79, 79, and 76 meV/C atom) and phenylenes (82, 80, 79, 79 meV/C atom). For the oligothiophenes they are higher by roughly 10% due to the presence of the sulfur atoms.

The case of the oligophenylene series (middle panel) deserves special attention. Here, we have to consider the non-planar geometry of the isolated nP molecules, which exhibit twisted interring bonds in the gas phase. The total energies of isolated 2P and 3P molecules for different values of the twist angle (dihedral angle between two consecutive benzene rings) are plotted in Fig. 5.4. There is a pronounced difference in terms of equilibrium torsional angles as well as activation energy barriers between PBE and vdW-DF. While the torsional angle of about 40° obtained from vdW-DF is close to the experimental value of 44°, PBE underestimates this angle by almost 10°. Allowing for such a conformation of the isolated molecules (Fig. 5.3, full symbols, full line) leads to smaller cohesive energies compared to the assumption of planar molecules (Fig. 5.3, open symbols, dashed line). For instance, this effect is found to result in a cohesive energy change of 0.1 eV for biphenyl and 0.13 eV for terphenyl. Despite the very good overall agreement with experiment by considering the non-planarity of the molecules, the cohesive energies for nP are still slightly larger than the reported experimental values. One of the possible reasons for this is the way

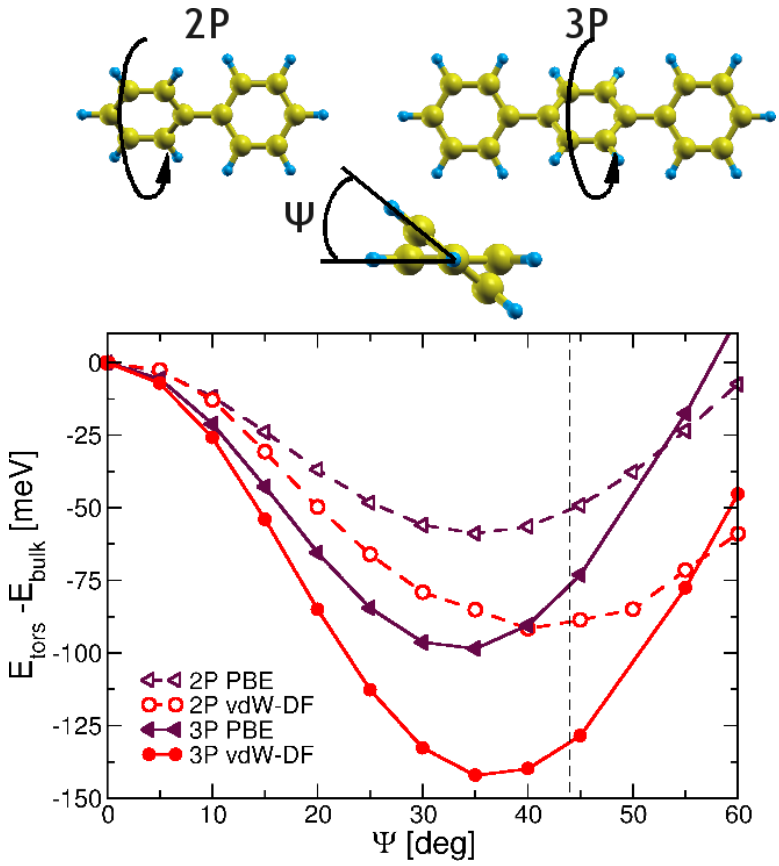

Figure 5.4: The total energy of the isolated 2P and 3P molecules as a function of the torsional angle Ψ. A definition of Ψ is shown on top. The experimental value for 2P $\Psi = 44°$ is depicted by the dashed vertical line.

in which the experimental cohesive energy have been determined. As already mentioned, the rough estimation of the vibrational contribution is only valid for rigid molecules. While this assumption is fully legitimate for the oligoacenes, the more flexible inter-ring bonds in the oligophenylenes may well lead to a deviation from the simple relation given by Eq. (5.2). In particular, the flexibility of the oligophenylenes explains the systematic increase of the difference between experimental and calculated data with larger oligomer size. Therefore, we can attribute the remaing small discrepancy of the vdW-DF results from experiment to an incomplete treatment of the vibrational contribution to the enthalpy.

Now we turn to the comparison between the results obtained using the vdW-DF and the semiempirical correction proposed by Grimme (Eq. (3.33)) [8]. There is an overall good agreement between the cohesive energies by both methods. However, only very small improvement over LDA is observed for the oligophenylene and oligothiophene series in case of GGA+vdWse. The main reason is that the semiempirical correction E_{disp} as defined in Eq. (3.33) is not universal. The em-

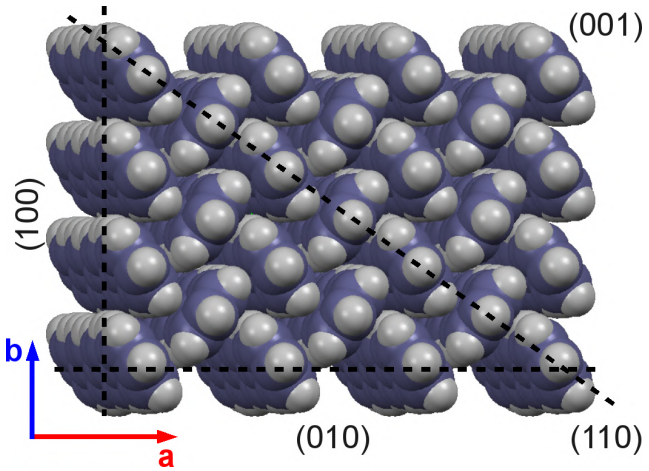

Figure 5.5: Investigated surface planes shown for the example of quaterphenyl.

pirical parameters which describe the vdW interaction are obtained by a fitting procedure for a number of benchmark systems and, hence, can only be reliably applied for the description of a special group of materials. The inclusion of new benchmark compounds and the improvement of the fitting procedure had already led to the new set of parameters in Ref. [66] as compared to Ref. [8]. In any case, the semiempirical correction E_{disp} relies on a summation over C_6 interaction terms between atomic pairs. However, in general the dispersion forces are not pairwise additive. The dispersion energy expressed by Eq. (3.33) is valid for the case of asymptotically separated regimes, e.g., for gases, and can not be regarded as fully reliable in case of crystals. On the contrary, E_c^{nl} from the vdW-DF theory does not contain any adjustable parameter. It depends on the details of the electron density distribution in a system and, hence, generally reflects any kind of binding situation. Such details can matter for the structural properties like torsion angles and the conformation of molecules in the crystalline environment, where small differences can lead to pronounced changes of the electronic structure. Therefore, one can conclude that the vdW-DF should be the basis for the investigation of the cohesive properties of organic crystals.

5.3.2 Surface energies

Experimentally, surface energies for the molecular crystals under consideration are difficult to access. In fact, no data can be found in literature. The excellent agreement between experimental and predicted cohesive energies using vdW-DF, however, allow for a prediction of the former. The (100), (010), (001), and (110) surface energies for the nA, nP, and nT series have been calculated and are presented in Table 5.1. It has been shown [100, 103] that they give the main contribution to the equilibrium crystal shape in the case of pentacene.

Table 5.1: Surface energies of the (100), (010), (001), and (110) planes of the nA, nP, and nT oligomers given in mJ/m^2. Results from empirical force field calculations values are displayed in parenthesis, *ab-initio* DFT data on the LDA level are given in square brackets.

	(100)	(010)	(001)	(110)
2A	102	107	90	120
3A	100	115	81	108
	(88[a])[66[c]]	(118[a])[91[c]]	(76[a])[53[c]]	(90[a])
4A	109	124	84	106
5A	107	130	82	113
	[77[c]]	(140[b])[103[c]]	(76[b])[50[c]]	(150[b])[75[c]]
2P	122	129	97	118
3P	124	136	99	123
4P	124	140	96	124
6P	142	142	107	135
2T	147	123	110	121
4T	134	133	102	125
6T	176	128	115	146

[a] Ref. [104], [b] Ref. [103], [c] Ref. [100]

These surfaces are indicated schematically in Fig. 5.5 for the example of 4P. For monoclinic crystals the planes (110) and (1-10) are equivalent. This is not the case for 4A and 5A, which have triclinic group symmetry. Therefore, the corresponding surface energies are, in principle, different. We calculated the values for both surfaces and found negligible small differences between them (less than 1%). This finding is due to the small deviation of their crystal structures from the monoclinic ones. For this reason the (1-10) results are not displayed.

A common feature for all compounds is that the (001) plane exhibits the lowest surface energy. This strong anisotropy (almost by a factor of two) is typical for the crystals formed by rod-like molecules. The nature of this anisotropy can be understood in terms of the crystalline packing in the (001) direction, which is governed by the weak H–H interlayer interactions. Hence, on substrates with comparably small substrate/molecule interactions, thin films are expected to wet the substrate and to be preferentially (001) oriented, since the total surface free energy is minimized in this case. The comparison of the surface energies obtained using different theoretical methods shows, in general, the same trends as the cohesive energies. From Table 5.1, one can see an almost constant difference of about 30 mJ/m^2 between the LDA [100] and vdW-DF values (see lines 3A and 5A in Table 5.1). This constant shift leads to almost the same equilibrium crystal

shapes obtained using both approaches. Good agreement is found between the vdW-DF and semiempirical force-field [103, 104] surface energies. However, there is big difference in the methodology of the vdW-DF and force-field techniques. The latter is based on the force-field parameters obtained by fitting calculated properties with experimental ones. So the reliability of the force-field method is mainly due to the quality of the empirical parameters. In contrast, the vdW-DF requires no *a priori* knowledge about the system giving a pure theoretical prediction of the physical properties for materials such as molecular crystals. However, the agreement between the values obtained using both methods serves as an additional argument of the reliability of the vdW-DF method.

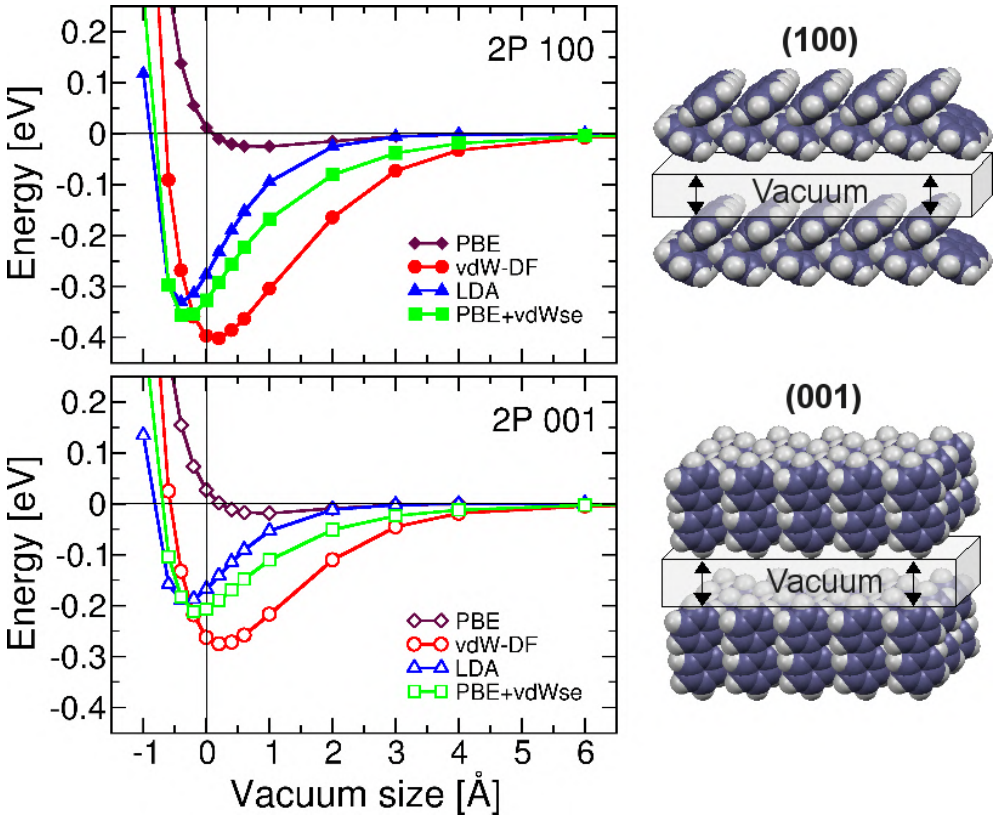

Figure 5.6: Total energy of a biphenyl crystal as a function of the vacuum layer thickness along the (001) and the (100) plane for different xc potentials. The zero energy corresponds to the crystal with "infinite" (10 Å) vacuum separation, i.e. to the energy of an isolated crystal slab.

Let us consider the results obtained by different theoretical methods in more detail. Fig. 5.6 displays the total energy as a function of the inserted vacuum thickness for the (100) and (001) planes of biphenyl, taking the energy of a 10 Å vacuum slab as the reference point (E_{slab} in Eq. (5.3)). As in the case of

the cohesive energies, one can see the superiority and reliability of the vdW-DF in comparison with other exchange-correlation potentials. First, the vdW-DF energy curve has its minimum close to zero vacuum, as it should be, since this geometry simply corresponds to the bulk structure at the experimental lattice parameter. Clearly, this is the case neither for LDA nor for PBE. The former gives rise to a compression along the direction normal to the respective crystal plane corresponding to a negative vacuum separation. In case of the (100) or (001) planes, it obviously leads to reduced equilibrium lattice parameters **a** and **c** by nearly 0.4 Å. GGA, on the other hand, predicts the equilibrium distances to be increased by as much as +1 Å. Second, also the surface energies strongly depend on the choice of the exchange-correlation potential E_{xc}. In Fig. 5.6 the surface energy corresponds to the value of the curve taken at $x = 0$ and divided by the doubled surface unit cell area $2A_{hkl}$ (Eq. (5.3)). Interestingly, irrespective of the index plane under consideration, the values of vdW-DF and LDA differ by approximately 25–30%. In contrast, they are almost zero for PBE which would predict unstable structures.

We now proceed with a discussion of the semiempirical approach that corrects the PBE energies by adding the missing vdW interactions. One can see in Fig. 5.6 that – as in the case of the cohesive energies – this method gives results very similar to LDA. It improves the equilibrium lattice spacings, while the surface energies differ from the vdW-DF ones by around 15%. Since the PBE produces almost no binding, the dispersion energy term (3.33) is solely responsible for the actual values of the cohesive and surface energies. Thus, using thoroughly chosen material-dependent parameters, the dispersion energy E_{disp} alone is already a practical tool to quickly estimate the cohesive properties of a molecular crystal, especially if it consists of a large number of atoms.

5.3.3 Crystal shapes

Using the surface energies as summarized in Table 5.1, one can obtain equilibrium crystal shapes (ECS) based on Wulff's construction as described in Section 5.2. The results are visualized in Fig. 5.7. The finding that the (001) surface energy is minimal for all oligomer series is illustrated by the fact that the (001) crystal faces have the largest area. Compared to experiment, excellent agreement is found with an investigation of the growth of anthracene on graphite [105]. In particular, the (001) orientation of the crystal parallel to the substrate, the appearance of approximately hexagonally-shaped facets of the (100) and (110) planes, and the small (010) facet is consistent with our calculated ECS. Within the acene and phenylene series, the crystal shapes vary only slightly, while the situation is more complicated for the thiophenes. In this series, the anisotropy in surface energies is strongest, as is their variation as a function of oligomer length due to the pronounced changes in crystalline packing with molecular size.

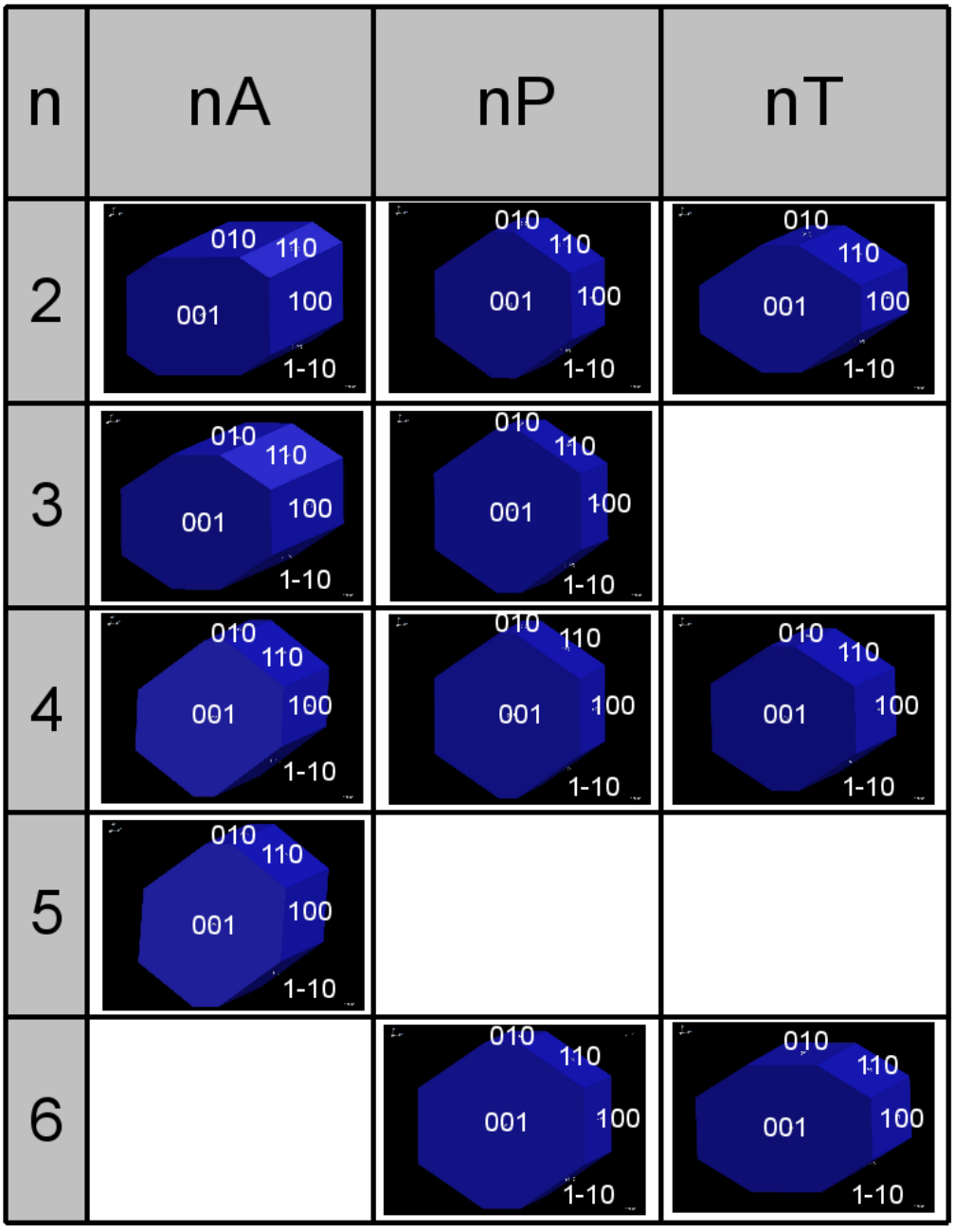

Figure 5.7: Predicted equilibrium crystal shapes of the oligoacene, oligophenylene, and oligothiophene series based on the calculated surface energies of the most important low index surfaces tabulated in Table 5.1.

5.4 Conclusions

An ab-initio study of bonding properties in molecular crystals has been performed consistently taking into account nonlocal van der Waals interactions. The usage of the vdW-DF provides a new level of precision in computing and predicting structural properties of molecular crystals. The calculated cohesive energies agree to within 5% with the experimental ones, while the difference between experimental and theoretical equilibrium lattice parameters is within 0.2 Å. This accuracy of ab-initio calculations is especially important for describing morphologies of organic molecular crystals and films, where subtle energy differences play an important role. Besides capturing the correct intermolecular bonding, vdW-DF opens the possibility to optimize crystal structures, i.e. by finding the optimal lattice parameters. The investigations performed serve as the starting point for future investigations regarding kinetic aspects in organic thin film growth.

An alternative method to treat vdW interactions within DFT, by adding a semiempirical correction [8], also shows rather good agreement with experimental data. Since the main contribution to the intermolecular binding comes from the dispersion forces, this approach is equivalent to any empirical force-field method. Therefore—relying on the fact that there is no covalent bonding—just computing this term can already give a good estimate for the cohesive properties of molecular solids. This is especially helpful considering the fact that it is computationally very cheap and, hence, can be used for systems with a large number of atoms. On the other hand, one should not forget about drawbacks that are inherent to any empirical method. For instance, the empirical parameters are rather system-dependent and can lead to good results in one system and bad ones in another.

Chapter 6

Organic molecules on metal substrates

The performance of organic light emitting diodes (OLEDs) or organic field effect transistors (OFETs) crucially depends on the interface formed between the metal electrodes and the organic semiconductor. This is because the charge carrier injection from the electrode into organic material is determined by the alignment of the electronic levels. Moreover, the strong dependence of charge carrier mobility on the molecular ordering on the substrate and the purity of the material is very important for the performance of the electronic devices based on the organic semiconductors. The interaction between the organic molecules and the metal surface determines the molecular order at the interface and, therefore, the resulting thin film morphology. Thus, investigation of the interfaces opens the possibility to deeply understand electronic and bonding properties of such systems, which, in turn, is a prerequisite for improving and creating new devices with desired properties.

Molecule/metal interfaces represent a hot research field. However, while much effort has been invested in description of the energy level alignment [39, 106], less attention has been paid to the adsorption energy, which is crucial for a proper description of film growth. DFT studies of the adsorption of benzene and thiophene molecules on the highly reactive nickel surface [107, 108] have revealed a reasonable agreement between experimental and theoretical predicted equilibrium geometries and adsorption energies. More recently, the adsorption of the large π-conjugated molecule PTCDA on the Ag(111) surface has also been investigated [109–111]. However, the reported adsorption energies not only contrast each other, but moreover, show rather bad agreement with experimental data.

The approximation for the exchange-correlation energy is the main reason for such discrepancies. The strong interaction between molecules and highly reactive surfaces is expressed by the covalent nature of bonding between these systems.

This type of bonding is well described in the framework of approximations such as GGA or LDA. In contrast, in the case of weakly bound systems, vdW interactions play the main role in the binding. Hence, the case of the molecules weakly interacting with surfaces is also a challenge for DFT.

Different theoretical approaches have been applied to remedy for the lack of long-range interactions in standard xc approximations. Semiempirical vdW corrections have been applied for investigating the adsorption of adenine on graphite [112] as well as pyridine, benzene, and pyrazine molecules on Ag(110) and Cu(110) metal surfaces, where the significant contribution of the vdW forces in binding has been stressed [113, 114]. Among ab-initio schemes, a combination of exact exchange and a solution of the adiabatic connection formula in the random-phase approximation (RPA) for the correlation term has been explored for the investigation of the binding energy of xenon and PTCDA on the Ag(111) surface [115], where the resulting equilibrium distances have been shown to be in close agreement with experiment. The vdW-DF [10] has been successfully applied to calculate the adsorption energy of benzene and naphthalene on a graphene layer [17]. Also for phenol on graphite(0001) and α-Al_2O_3(0001) [116] it was shown that the dispersion forces give a crucial or, at least substantial, contribution to the total adsorption energy.

In this chapter we apply the vdW-DF theory to determine and understand the role of the dispersion interactions in the adsorption mechanism of organic molecules on metals. First, we examine the adsorption of a thiophene ring on the Cu(110) and the reconstructed Cu(110)-(2x1)O surface. Then, a PTCDA monolayer physisorbed on the noble metal surfaces Au(111), Ag(111), and Cu(111) is considered.

It should be noted that the investigation of the adsorption geometry of these organic molecules on surfaces is not part of this thesis. The corresponding calculations have been carried out by Priya Sony in case of 1T on Cu(110) and Cu(110)-(2x1)O [117, 118], and by Lorenz Romaner regarding PTCDA on the noble metals [119]. However, some of the results are presented here for different reasons. First, they have been computed with the vdW-DF code developed within the thesis. Second, the performance of different xc functionals shall be discussed in the following, as was done for the cohesive properties of the organic crystals. And last but not least, the description of molecule/metal junction has an important impact on the understanding of organic film growth. An outlook on this issue based on the results for both the surface energies of the organic materials as well as the molecular adsorption will be provided in Chapter 7. In the following parts of Refs. [117, 119] are reproduced after having been slightly adapted to the structure of this thesis.

6.1 Thiophene on Cu(110) and Cu(110)-(2x1)O

The adsorption of the thiophene molecule on metal surfaces can be considered as a prototypical system for the investigation of the basic properties of an organic molecule/metal interface. Since the vdW-DF is applied as a post-self-consistent field treatment, only the search for the adsorption site and orientation relies on the evaluation of total energies and cannot make use of the calculation of atomic forces. Hence, it is a time-consuming and challenging task for such large systems as molecules physisorbed on substrates. The evaluation has been performed in two steps. First, the adsorption sites and geometries have been explored using PBE. In a second step, various sites and orientations have been recalculated by the vdW-DF. The latter calculations have revealed only small changes compared to PBE [118][1]. Therefore, here, the PBE geometry of the molecule on top of the respective surface is adopted as a starting point for the evaluation of vdW-DF for the adsorption process.

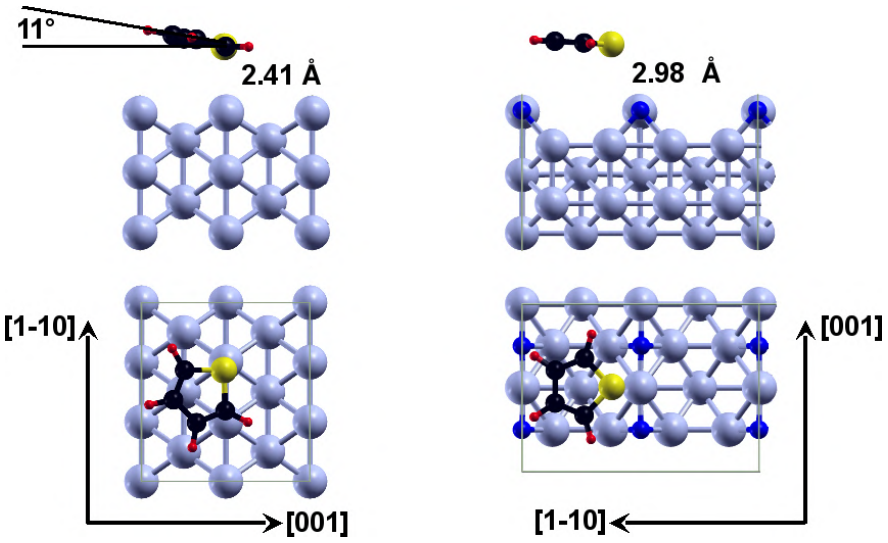

Figure 6.1: The side and top view of the most favorable adsorption geometries of a thiophene ring (1T) on a Cu(110) (left) and a oxygen corrugated Cu(110)-(2x1)O surface.

Side and top views of the adsorption geometries on Cu(110) and Cu(110)-(2x1)O surfaces are depicted in Fig. 6.1. On Cu(110), 1T is rotated by 45° with respect to the [001] direction, such that the sulfur and one of the carbons are located above the copper atoms of the first layer. The shortest distance between the molecule and the surface for the case of Cu(110) surface was found to be 2.41 Å with the molecule tilted by an angle of around 11°. Comparing the calculated bond lengths of the isolated and the adsorbed thiophene molecule, the strongest

[1]These findings are not expected to apply in general.

effect is found for the S–C bonds which are increased in length by 1.3% (0.3%) for the bond parallel (perpendicular) to the $[1\bar{1}0]$ direction. All other changes in the intramolecular bond lengths are below 0.2% indicating the comparably weak molecule/substrate interaction.

A different adsorption geometry is found for the 1T molecule on the Cu(110)-(2x1)O surface. Here, the molecule avoids the vicinity of the oxygen atoms, but prefers to be closer to copper. The shortest Cu-S, O-S, and molecule-metal distances are obtained as 2.98 Å, 3.48 Å, and 2.71 Å, respectively, with the molecule lying flat on the surface. Thus, due to a compromise between repulsion from oxygen atoms and attraction to copper atoms, 1T prefers a position surrounded by four equally spaced oxygen atoms (see Fig. 6.1 (right))[118]. This is in contrast to the situation of the clean Cu(110) surface, where the molecule rotates and adopts the adsorption site in which sulfur lies above the copper atom.

The adsorption energy E_a is calculated according to the definition

$$E_a(d) = E(d) - [E_{1\mathrm{T}} + E_{\mathrm{surface}}], \tag{6.1}$$

where $E(d)$ is the total energy of the combined system and d denotes the adsorption distance which is defined as the z-projection of the shortest molecule–metal distance. $E_{1\mathrm{T}}$ and E_{surface} are the total energies of the thiophene molecule and the underlying surface, respectively, which are calculated by adopting the unit cell size and convergence parameters as for the interacting system.

The adsorption energies, $E_a(d)$, obtained by PBE, revPBE, and vdW-DF for both 1T on Cu(110) (left) and Cu(110)-(2x1)O (right) as a function of the molecule-metal distance, d, are displayed in Fig. 6.2. One can see that PBE leads to an adsorption energy of -0.26 eV at an equilibrium distance of 2.4 Å for 1T on Cu(110) and -0.08 eV at 2.7 Å for 1T on Cu(110)-(2x1)O. In contrast, revPBE does not give rise to any binding for both systems. The discrepancy between the results obtained by the different flavors of GGA is due to the parameterization of their exchange parts, as discussed in Section 3.2.2. Similiar to PBE, PW91 binds the van der Waals systems due to the wrong reason.

On applying vdW-DF, the adsorption energy of -0.50 eV at a molecule–surface distance of around 2.8 Å is obtained for 1T on Cu(110). A slightly smaller value of -0.42 eV is found for 1T on Cu(110)-(2x1)O with a bond length of 2.9 Å. Upon addition of the nonlocal correlations, we find the equilibrium metal/molecule separation to be increased by 0.4 Å for Cu(110) and 0.2 Å for Cu(110)-(2x1)O with respect to the PBE results, while the adsorption energy is almost twice the PBE value for Cu(110) and almost five times as large in the Cu(110)-(2x1)O case. These striking differences clearly demonstrate that nonlocal dispersion forces are the main physical origin for the adsorption in these systems. Moreoever, they reflect the poor performance of PBE. One can conclude that standard GGA functionals do not only underestimate the adsorption energies but also provide

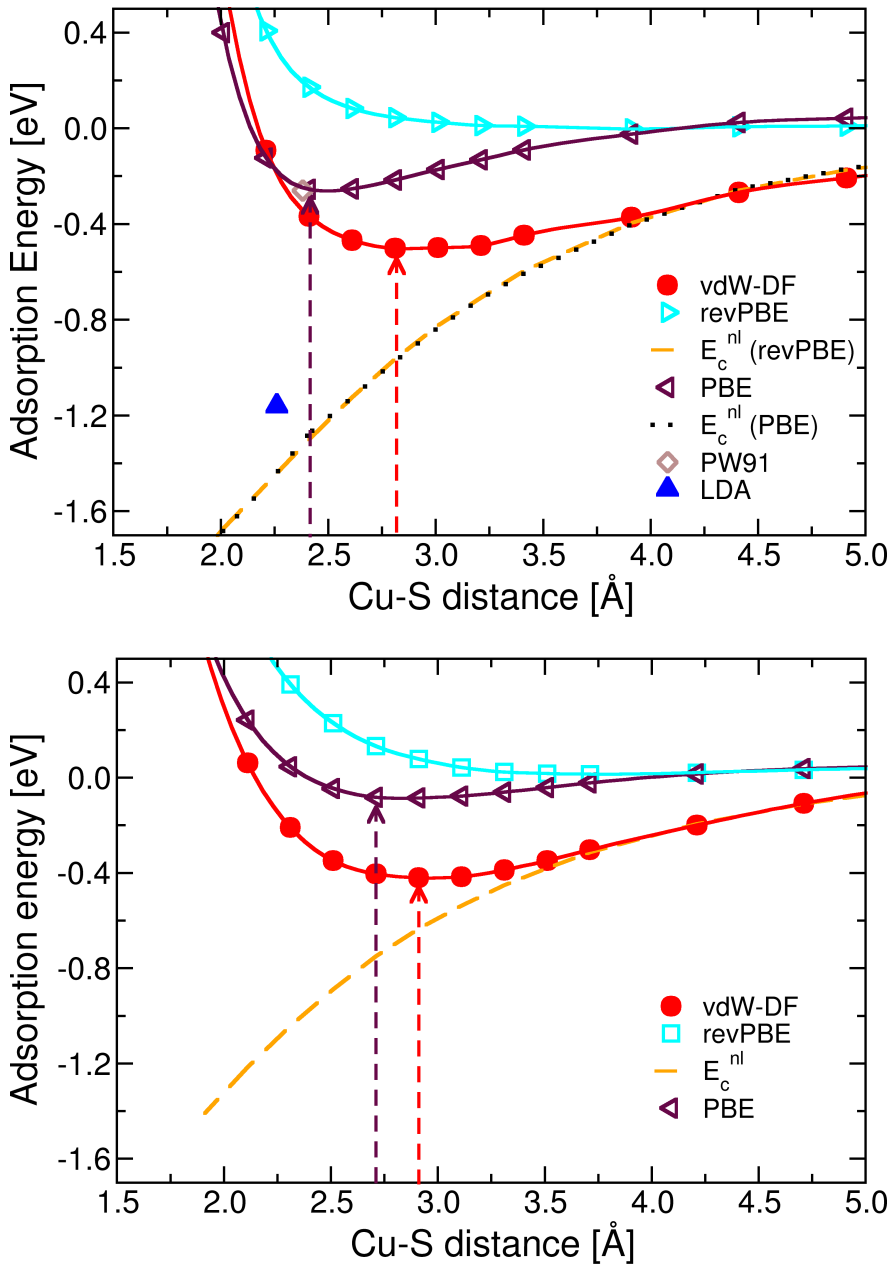

Figure 6.2: Calculated adsorption energy of a thiophene ring on the Cu(110) (top) and Cu(110)-(2x1)O (bottom) surfaces as a function of the shortest Cu-S distance for various exchange-correlation potentials.

an incoherent physical picture of the binding mechanism. Hence, the possible success of PBE in such weakly bound systems remains a mere coincidence. These findings are of relevance not only for weakly adsorbed molecules but also for more strongly bound molecule/metal junctions. In general, a correct treatment of nonlocal correlations should increase the reliability of predictions for adsorption energies and molecule/metal distances.

Fig. 6.2 (top) also shows that there is almost no dependence of the nonlocal correlation energy on the type of GGA used for obtaining the self-consistent density. In particular, PBE and revPBE lead to almost identical charge densities. Therefore, the electronic properties are not sensitive to the choice of the functional. For the sake of completeness, we also mention the equilibrium bond distance and binding energy obtained within the LDA, which are -1.16 eV and 2.26 Å, respectively. The LDA considerably overestimates the binding energy while it underestimates the metal/molecule distance compared to vdW-DF and experiment.

Experiments have been performed for 1T on Cu(100) and Cu(111), but no data is available for Cu(110). However, calculations by Mittendorfer et al. [107] for benzene on low-index Ni surfaces have demonstrated that the difference in the adsorption energies corresponding to the (100) and (110) surfaces is around 10–15%, while the bond distance is hardly affected. Expecting a similar behavior for Cu, one can compare the theoretical results with the available experimental data reporting a flat adsorption geometry and Cu–S distances between 2.50 ± 0.02 Å [120] and 2.60 ± 0.05 Å [121] on Cu(111), while a slightly lower value of 2.43 ± 0.03 Å has been found for the adsorption of 1T on the Cu(100) facet [122]. Thermal desorption spectroscopy applied to a thiophene monolayer on Cu(100)[123] revealed an adsorption energy of -0.63 eV. Considering all measured data, the vdW-DF results for the adsorption energy and distance for 1T at Cu(110) are in good agreement with available experiments, although no direct comparison can be made. Also the passivation of the Cu(110) surface by oxygen leading to a smaller adsorption energy for the oxygen-reconstructed substrate is in agreement with experimental observations [124].

Regardless of the success of vdW-DF to properly describe weak interactions of molecules with metal substrates as demonstrated above, one has to note that the theoretically obtained equilibrium distances are found to be somewhat larger than experimental values, the deviation being of the order of 0.2 – 0.4 Å. A systematic overestimation of equilibrium bond lengths has already been observed in literature [13] and confirmed for our test systems discussed in Section 4.2. We shall return to this issue at the end of this chapter.

6.2 PTCDA on Ag(111), Au(111), and Cu(111)

3,4,9,10-perylene-tetracarboxyl acid diahydride (PTCDA) is one of the best characterized molecules of large size [125]. In particular, recent photoemission and x-ray standing wave (XSW) experiments carried out for PTCDA adsorbed onto Ag(111), Au(111), and Cu(111) have shown characteristic trends for work-function change, alignment of molecular levels, and vertical binding distances.

Previous investigations based on DFT for PTCDA on Ag(111) have revealed a number of different results showing that a proper description of the present systems is demanding. Studies employing the generalized gradient approximation (GGA) [109, 110, 126] reported adsorption distances much larger than the ones observed in experiment, together with unrealistically small adsorption energies. In Ref. [111], the authors found better agreement with experiment, however, in connection with a strong arching of the molecule. Studies based on the local density approximation (LDA) [127, 128] show very high binding energies of about 2.5 eV per molecule and adsorption distances in quite good agreement with experiment. Furthermore, an approach employing exact exchange and the random phase approximation (RPA) yielded a reasonable binding energy together with a somewhat overestimated bond distance on Ag(111) [115].

A top view of a PTCDA monolayer adsorbed on Ag (left) and Cu (right) is shown in Fig. 6.3. PTCDA on the Ag(111) surface forms a monolayer commensurate with the substrate [129, 130] and has the $\begin{pmatrix} 6 & 1 \\ -3 & 5 \end{pmatrix}$ surface unit cell containing two inequivalent PTCDA molecules and 33 atoms per metallic layer. The adsorption site is chosen in agreement with previous investigations [127].

Investigations of PTCDA on Au(111) have revealed that molecules do not form monolayers commensurate with the substrate but exhibit a point-on-line growth on the $(22 \times \sqrt{3})$ reconstructed surface [131–134]. To take into account these effects in the calculations would require an excessive computational effort since one would have to choose a huge supercell size. Therefore, we adopt the same unit cell as used in the Ag case. This approach can be regarded as reasonable since the lattice constants of Au and Ag are almost the same (2.95 Å for Au vs 2.94 Å for Ag).

On the Cu(111) surface the PTCDA monolayer has also been found to form a herringbone structure [135] with a larger $\begin{pmatrix} 6 & 3 \\ -4 & 6 \end{pmatrix}$ surface unit cell (Figure 6.3, right panel) induced by the significantly smaller lattice parameter of Cu of 2.57 Å compared to Ag.

The adsorption energy, $E_{ads}(d)$, is calculated in the following way:

$$E_{ads}(d) = \frac{1}{2}[E_{met+mono}(d) - (E_{met} + E_{mono})], \tag{6.2}$$

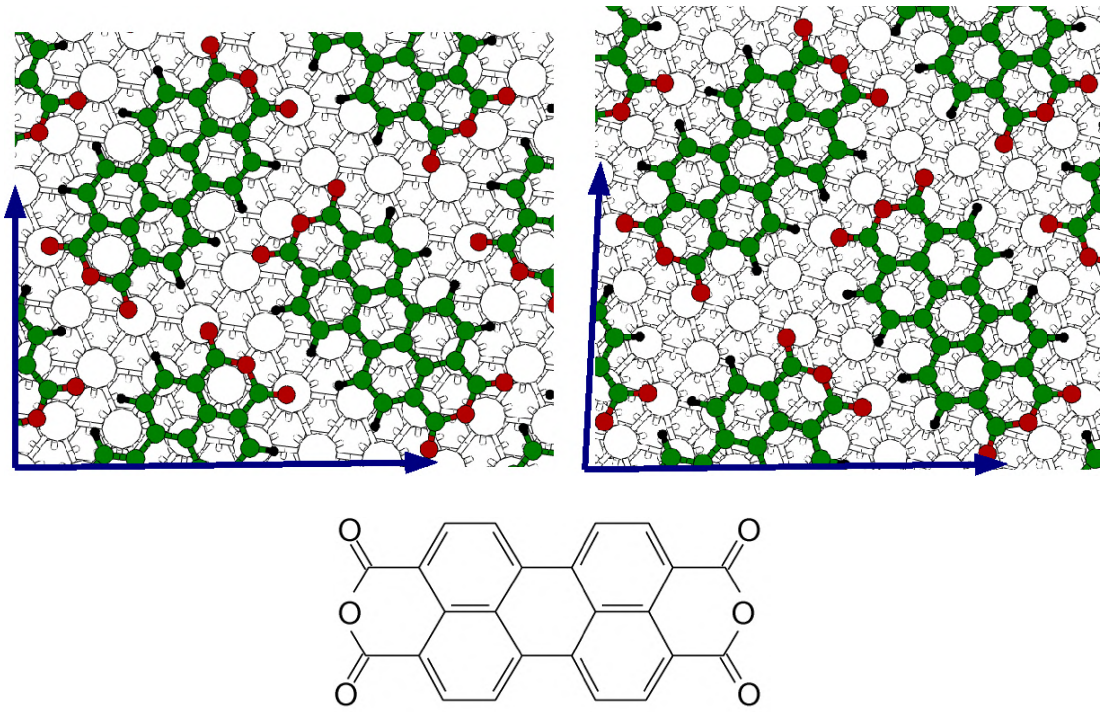

Figure 6.3: Top: Top view of PTCDA adsorbed on metal surfaces. On the left, PTCDA on Ag(111) is illustrated, and on the right PTCDA on Cu(111) is depicted. The large blue arrows indicate the surface unit cell vectors. The metal surface atoms are represented by white circles while the carbon atoms are colored green, the hydrogen atoms black, and the oxygen atoms red. Bottom: Representation of the chemical structure of PTCDA.

where $E_{met+mono}(d)$ is the energy per unit cell of the metal-monolayer system when the monolayer is placed at a specific distance d to the surface. E_{met} is the energy of the isolated metallic slab, and E_{mono} is the energy of the isolated monolayer.

As shown in Fig. 6.4, the adsorption energy produced by PBE is found to be largely repulsive for all three metals, where a very small binding contribution can be observed at large distances to the surface (about 4 Å). For the Ag substrate this has already been described in Refs. [115, 126, 136]. The E_{ads} curves strongly contrast with the XSW results which show that the monolayer should be adsorbed much closer to the surface for all three metals. Experimentally, the desorption energy of PTCDA is not accessible as the molecule dissociates prior to desorption (see, e.g., [130]). However, for NTCDA, which has a naphthalene instead of perylene building block in the molecular center, thermal desorption spectroscopy at submonolayer coverage has reported desorption energies of 1.2 eV [137]. As NTCDA is about half the size of PTCDA one can expect that the adsorption energies should be as large or even larger.

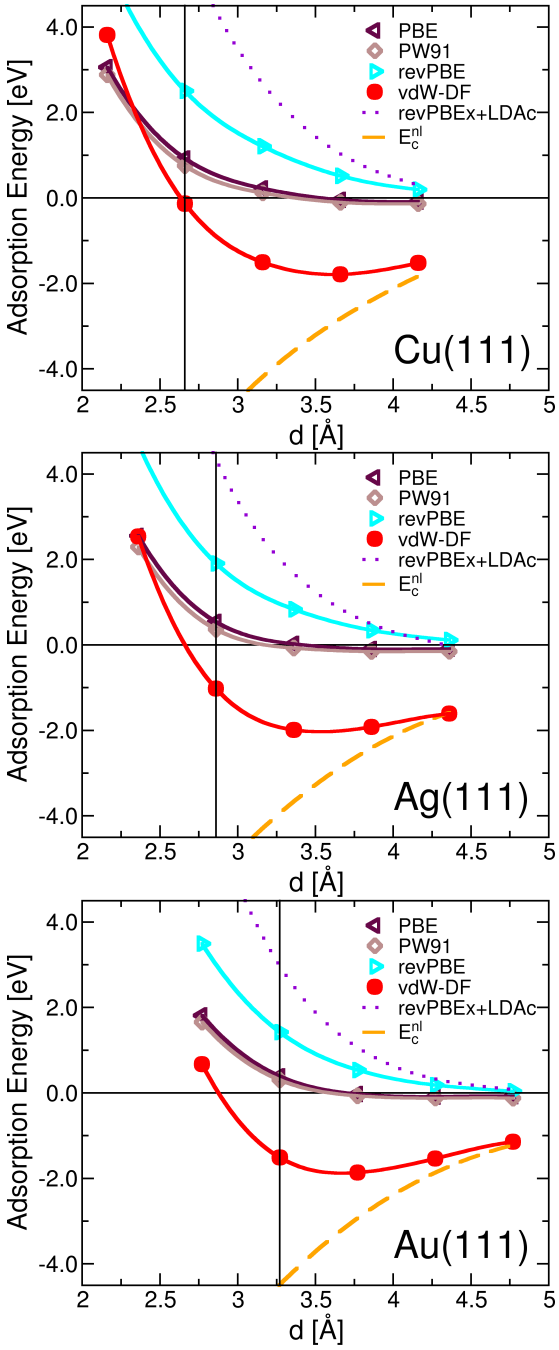

Figure 6.4: Adsorption energy calculated using different types of exchange correlation potentials: PBE, PW91, revPBE, the exchange part of revPBE together with the LDA correlation, from dispersion forces (E_c^{nl}) solely, and with the vdW-DF. All quantities have been calculated from the PBE self-consistent charge density. The experimentally measured (XSW) equilibrium distances for the Ag, Cu, and Au surfaces are given for comparison (vertical lines).

The PW91 functional gives results very similar to those of PBE, producing very weak binding energies at rather large equilibrium distances. This is not the case for the LDA. In agreement with earlier works [127, 128], a structural optimization of the monolayer on top of Ag, where no constraints are imposed on the molecule, gives binding distances in reasonable agreement with XSW experiments and realistic negative values for the adsorption potential (-3.04 eV, -3.20 eV, and -1.80 eV for the Ag, Cu, and Au surface, respectively). The reasons for this behavior are rooted in the unconstrained structural optimization which leads to arching [119], as is the case also here.

Proceeding now to vdW-DF, we observe that the dispersion forces yield a very strong binding contribution of about 5–6 eV per molecule at the experimental distances. The dashed lines in Fig. 6.4 present the adsorption energy calculated from E_c^{nl} alone. These curves are purely attractive for the three different substrates and rather similar for all three surfaces, i.e. Au gives a slightly stronger attraction than Cu and Ag.

Finally, the vdW-DF adsorption energies are presented as red circles. For all substrates, the corresponding curve exhibits a pronounced minimum of about -2 eV at around 3.5 Å. In the Ag case, the result can be compared to Ref. [115] where E_c^{nl} calculated within the RPA is combined with an exact exchange approach. In this way, a similar adsorption potential was obtained giving a somewhat smaller binding distance of 3.2 Å and a comparable adsorption energy of 2.5 eV. Furthermore, a study based on an embedded atom model reported an adsorption energy of about 3.5 eV for PTCDA on Ag(111) [138].

Compared to the experimental situation the bonding distances are systematically overestimated with the biggest deviations obtained for the Cu surface. Hence the vdW-DF corrects the failure of the GGA functionals insofar as it results in reasonable binding energies, but it still shows a tendency to bind the monolayers at too large distances.

6.3 Conclusions

In this Chapter, the adsorption of organic molecules on metal substrates has been investigated. To this intent two different prototypical systems have been studied. The first one consists of thiophene physisorbed on the Cu(110) and oxygen reconstructed Cu(110)-(2x1)O surfaces. For both cases, the binding has been found to be purely due to vdW interactions. The standard GGA functionals underestimate the adsorption energy and, hence, provide a wrong physical picture for the binding. The vdW-DF results are supported by experimental data for 1T on Cu(100) and Cu(111). Based on these findings one can conclude that nonlocal correlations are crucially important for thin film growth, other surface reactions, and catalytic processes.

Similar results have been obtained for the adsorption of the PTCDA molecule on the (111) surfaces of the three coinage metals Ag, Cu, and Au. In these structures, the calculated adsorption distances and binding energies have also revealed a strong sensitivity to the xc-functional. Again, as in the case on 1T on Cu(110) and Cu(110)-(2x1)O surfaces, GGA, which is not capable of describing dispersion forces, leads to clearly wrong adsorption energies, while LDA, which suffers from the same short-coming, gives results rather close to the XSW data, however, due to a fortuitous cancellation of errors. The attraction arising from dispersion forces amounts to several eV for all three substrates. Including this nonlocal effect, the GGA results can be improved and give adsorption energies of about 2 eV per molecule together with adsorption distances of about 3.5 Å for all substrates. The latter are, however, not fully consistent with XSW results.

This observation indicates shortcomings regarding the construction of the vdW density functional. To summarize, a systematic overestimation of bond lengths has been found for both systems under investigation, i.e. 1T on clean and oxygen-modified Cu surfaces as well as PTCDA on the three coinage metals. As already mentioned above, this behavior of vdW-DF is known in literature [13] and is currently a hot topic of research [72]. One of the main reasons for this lies in the approximation for the exchange energy used in the vdW-DF. The argument as to why the revPBE exchange part is used in the vdW-DF expression (3.63) is the similarity of the latter with the exact (or Hartree-Fock) exchange. This result has, however, been obtained for a limited number of systems and, therefore, this point needs further investigations. And finally, the "local" correlations, i.e. that part of the correlation effects which is not covered by the long-range contribution E_{nl}, is not necessarily local, hence, requiring the derivation of gradient corrections. Furthermore, the plasmon pole model used to describe the polarizability might be too approximative to capture the attraction from dispersion forces correctly. However, the good agreement with Ref. [115] suggests that the error induced in this manner is most likely not significant for these systems. Furthermore, the role of a self-consistent treatment of the vdW-DF [70] should be explored even if the effect can be expected to be small. As a matter of fact, vdW-DF is a very good starting point but further developments from the theoretical side are still required.

Chapter 7

Outlook on organic thin film growth

An understanding of organic thin film growth is the ultimate goal of the current investigations. In spite of the enormous effort aiming at the improvement of the quality of materials and the functioning of organic devices, the underlying growth mechanisms are not well understood yet. One the one hand, the weak intermolecular bonding goes hand in hand with shallow energy potentials leading to polymorphism, since different molecular conformations exhibit only small energy differences. Moreover, the pronounced anisotropy and complex nature of the molecules as the building blocks make organic film growth fundamentally different from the inorganic counterpart. As a matter of fact, molecule-molecule as well as molecule-substrate interactions strongly depend on the relative orientations of the interacting objects. The deposition of a molecular layer on top of a substrate is determined by a delicate balance between the weak interactions among the molecules as well as between molecule and substrate. It is this interplay which governs thin film morphology. For example, depending on the nature of the substrate, the orientation of deposited pentacene molecules can vary from islands of standing molecules on inert and flat substrates, to flat lying molecules on metal surfaces [139]. Moreover, the morphology of 6P on a single substrate can be different as a function of the growth conditions [140]. A more recent report by Hlawacek et. al [141] has revealed a multilayer growth of 6P on mica in the form of terraced mounds, where a combined experimental and theoretical analysis has exposed a sizable Ehrlich-Schwoebel barrier.

Investigation of the energetics of organic molecular crystals as well as their interaction with metal substrates allows some conclusions to be drawn in terms of thin film growth close to equilibrium where the surface energies of the respective constituents as well as the interface energy between the film and the substrate play important roles [99, 142]. First, a short overview of thin film growth from a thermodynamic point of view will be provided. Based on this, the results ob-

tained within this thesis are evaluated to draw some first conclusions about film growth of organic molecules on metal substrates.

7.1 Theory of thin film growth close to equilibrium

Thin film deposition is a special case of epitaxial growth. The term *epitaxy* is used for the growth of a crystalline layer on (*epi*) a crystalline substrate, where the crystalline orientation of the substrate imposes an order (*taxis*) on the orientation of the deposited layer.

The orientation of the deposited layer is determined by the constraint to minimize the contribution to the interface energy which arises from a possible mismatch between the substrate and the crystal structure of the deposited material. In the case when the two materials are different, the term *heteroepitaxy* is used. When the growth of a crystalline layer on a chemically identical, crystalline substrate is considered, the term *homoepitaxy* is commonly employed.

There is a classification of epitaxial growth based on thermodynamic considerations, which therefore applies to growth near thermodynamic equilibrium [142]. Different growth modes may be distinguished according to the balance between the surface free energy γ_D of the deposited material, the surface free energy γ_S of the substrate, and the interface free energy γ_{int}. The interface energy is defined by the Dupré-relation

$$\gamma_{int} = \gamma_S + \gamma_D - \beta_{SD}, \tag{7.1}$$

where β_{SD} is the work required to separate substrate and deposited crystals in their actual orientations and with actual atomic distances [143].

Let us consider the case

$$\gamma_S < \gamma_D + \gamma_{int}. \tag{7.2}$$

The energy balance requires minimization of the area covered by the deposited material, which will grow in the form of three-dimensional islands on the substrate. This mode is called *Volmer-Weber growth* (Fig. 7.1a). The opposite condition

$$\gamma_S > \gamma_D + \gamma_{int} \tag{7.3}$$

leads to maximization of the area covered by the deposited material and the film will initially grow smoothly, i.e. layer by layer. In case of heteroepitaxy, after deposition of a certain number of layers, the condition (7.3) must break down because the original influence of the substrate is screened by the deposited material. At some moment the two surface energies γ_S and γ_D will be nearly equal. However, the elastic influence of the substrate, for example, will give rise to a positive, nonzero interface energy γ_{int} between two successive layers. Thus, we

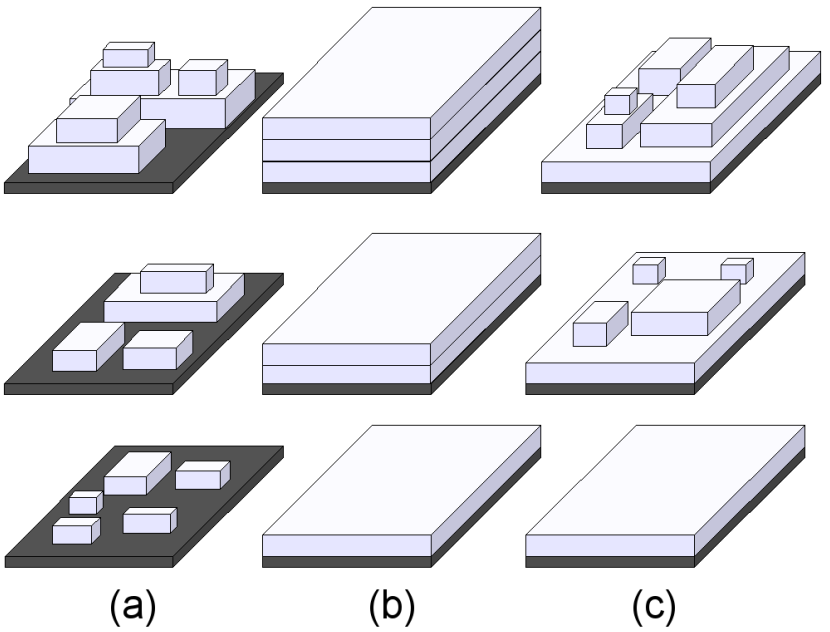

Figure 7.1: The three epitaxial growth mechanisms close to thermodynamic equilibrium: (a) Volmer-Weber, (b) Frank-van-der-Merwe, and (c) Stranski-Krastanov growth mode.

return back to the case (7.2), where three-dimensional islands will form starting at some film thickness. This scenario defines the *Stranski-Krastanov growth* mode, where 3D islands are formed on a wetting layer (typically a monolayer).

Finally, the limiting condition

$$\gamma_S = \gamma_D + \gamma_{int} \tag{7.4}$$

can only be fulfilled for homoepitaxial growth systems, where $\gamma_{int} = 0$ by definition. The corresponding *Frank-van-der-Merwe growth* mode is characterized by layer-by-layer growth of unlimited duration.

Introducing the quantity

$$\Delta\gamma = \gamma_D - \gamma_S + \gamma_{int} = 2\gamma_D - \beta_{SD}, \tag{7.5}$$

where for the last expression the Dupré relation (7.1) has been used, the growth mode conditions (7.2), (7.3), and (7.4) can be reformulated. The sign of $\Delta\gamma$ determines the corresponding growth mechanism: positive values corresponds to the Volmer-Weber growth mode, negative corresponds to the Stranski-Krastanov mode, and the case of equality to zero results in the Frank-van-der-Merwe mode.

One should stress that the classification scheme stated above describes near-equilibrium growth modes. In many cases, experimentally observed film morphologies can be easily associated with the Volmer-Weber, Stranski-Krastanov

or Frank-van-der-Merwe scenarios. However, the real nature of the morphology can have a predominantly kinetic origin due to growth conditions far from equilibrium (e.g., deposition and diffusion rates) or be caused by heteroepitaxy energetic effects such as the lattice mismatch or differences in surface energies.

7.2 First conclusions on organic thin film growth

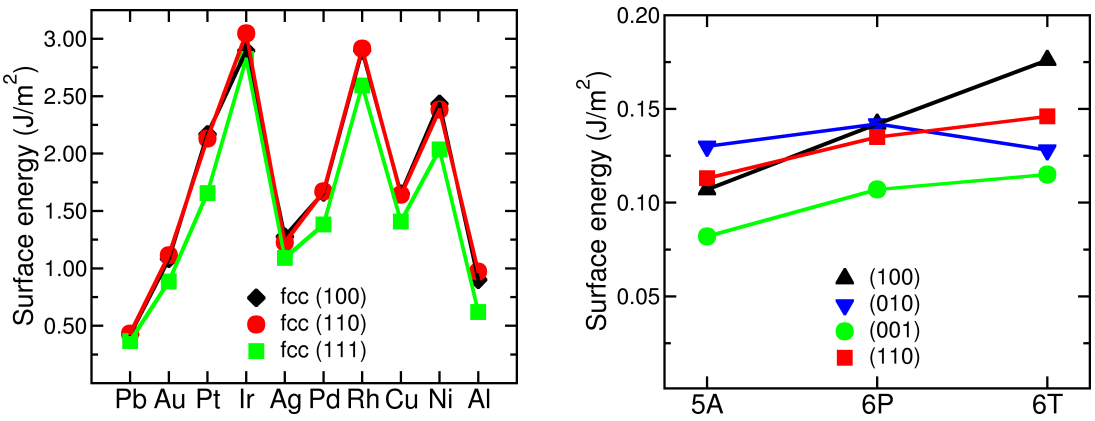

Figure 7.2: Surface energies of fcc metals taken from Ref. [144] (left panel) in comparison with surface energies of pentacene (5A), sexiphenyl (6P), and sexithiophene (6T) crystals (right panel) for selected orientations.

Using the theory of near-equilibrium crystal epitaxial growth described in Sec. 7.1, we are able to give several conclusions about the growth of organic crystals on metal substrates, for which the respective surface energies are some of the most important quantities. In Fig. 7.2, the surface energies of fcc metals [144], γ_S, and some of the more technologically important organic solids, γ_D, are depicted for comparison. As one can see, the surface energies of metals are as much as one order of magnitude larger than the surface energies of molecular crystals.

Another crucial parameter is the interface energy, γ_{int} (7.1), which we can roughly estimate by using the results of Chapters 5 and 6. From Table 5.1 one can see a rather weak dependence of the surface energies on the oligomer size and surface orientation. We suppose, therefore, that the 1T crystal has similar values of surface energies to 2T and hence adopt its average value 0.12 J/m^2. Moreover, the adsorption energy of 1T on Cu(110) has been found to be 0.5 eV. Estimating approximately the effective contact area between 1T and the substrate (assuming a circular shape of the lying molecule) one obtains about 0.5 J/m^2 for the specific adhesion energy.

Using the results obtained above and Eq. (7.1) one can now estimate the interface energy:

$$\gamma_{int} = 1.64 + 0.12 - 0.5 = 1.26 \text{ J/m}^2.$$

It is found to be of the same order as the substrate surface energy and as much as one order of magnitude larger than the characteristic surface energies of molecular crystals.

Using the condition determining the growth mode, Equation (7.5), one obtains,

$$\Delta\gamma = 2 \cdot 0.12 - 0.5 = -0.26 \text{ J/m}^2 < 0.$$

The negative value of $\Delta\gamma$ predicts a Stranski-Krastanov growth mode (see Fig. 7.1c). However, taking into account the simplicity of the estimation and the rather small value of $\Delta\gamma$, we conclude that the growth mode could be close to the "ideal" layer-by-layer Frank-van-der-Merwe type. In fact, in such a case a strong influence of the growth kinetics (temperature and growth conditions) on the resulting thin film morphologies can be expected. As demonstrated recently, peculiarities which are not known from inorganic epitaxy are observed as a consequence of the complexity and anisotropy of the building blocks [141].

Chapter 8

Structure solution of organic thin films

8.1 Introduction

A detailed knowledge of thin film formation is of major importance since the optoelectronic properties are strongly influenced by the structure and morphology of the deposited material. In particular, a strong dependency of the optical and charge transport properties is observed on the preparation conditions [145, 146]. This finding is related to the strongly pronounced anisotropy of the optical spectra in these low-dimensional systems as shown for a variety of molecular crystals by ab-initio calculations [101, 147, 148].

The interaction of the deposited material with a substrate can lead to the formation of structures which differ from the well-studied single crystal ones. These surface-induced polymorphs are limited to the first layers of the grown films and, therefore, impose limitations on standard experimental techniques for crystal structure determination such as an x-ray diffraction.

In this chapter, a combined experimental-theoretical method is described aiming at the structural solution of organic materials. From the experimental side, a combination of specular x-ray diffraction with grazing incidence diffraction is used to observe characteristic diffraction peaks in reciprocal space. The dimensions of the crystallographic unit cell are determined by indexation of reciprocal space maps. These experimental parameters are used as an input for *ab-initio* calculations within the framework of DFT to determine the molecular packing inside the crystallographic unit cell. This method has been successfully applied to the investigation of the thin film structures formed by pentacene [149] and *para*-cyano-quaterphenylene [150] molecules.

The task for the theoretical side was to reveal an unknown packing of molecules inside an experimentally determined unit cell. The x-ray diffraction experiments

followed by the indexation procedure have been performed by Oliver Werzer for the pentacene [149] and Armin Moser for the *para*-cyano-quaterphenylene [150] thin films in the group of Roland Resel at the Institute of Solid State Physics at the Graz University of Technology. For sake of completeness, an overview of the experimental details and results used in this chapter are given below. More information concerning the experimental part can be found in the corresponding references or in Refs. [151, 152].

8.2 Methods

8.2.1 Experimental approach

Two-dimensional powder

The morphology of the organic thin films prepared by physical vapor deposition onto isotropic surfaces is often characterized as a two-dimensional powder. This is an intermediate case between a single crystal and a crystalline powder. The specifics of such morphology is that the crystallites have a preferred orientation of one of the growth planes (typically (001)) parallel to the substrate surface, at the same time showing no in-plane alignment (for more details see Ref. [151]). In this case, the powder of crystallites is said to have a texture. A texture where only one degree of freedom (here the rotation around the surface normal) is present is called fiber-texture. This preferred orientation is the fiber axis [153]. Such specifics of textured thin films leads to the fact that the reciprocal lattice consists of a set of rings where the radii are determined by the in-plane component of the scattering vector, $q_p = \sqrt{q_x^2 + q_y^2}$. The latitude of the rings correspond directly to q_z. Therefore the procedure of the reciprocal space mapping is to perform radial scans along q_p for different detector elevations.

Grazing incidence diffraction

X-ray diffraction is a very efficient tool to investigate the structures of bulk crystalline materials. X-rays weakly interact with matter and, therefore, have a number of advantages such as significant penetration into the material (typically of 0.1-10 mm, depending on the substance and the x-ray energy) allowing the measurement of microscopic structural information averaged over a large ensemble of atoms and molecules. However, this advantage of x-rays for bulk studies turns into a disadvantage when the structure of surfaces and interfaces is concerned. In spite of this, the x-ray diffraction technique can be modified to overcome this limitation. Grazing-incidence diffraction (GID) has been shown to be a powerful tool for dealing with monolayers and thin films [154]. The GID geometry makes

x-ray scattering surface sensitive, i.e. largely avoids scattering from the substrate. Moreover, radiation damage is essentially reduced, as the power density of the beam is spread over a large scattering area. GID is based on the fact that the reflective index for most materials is slightly less than 1.0 at x-ray energies. Therefore, if the incident angle is small enough (typically 0.05-1.5°, depending on the substrate electron density and the x-ray energy), one can observe total external reflection from a surface. With this geometry, the penetration depth is extremely sensitive to the incidence angle. Therefore, very low penetration depths can be achieved which enables scattering mainly from the top layers, i.e. the organic film. The penetration depth is below 1 nm for angles smaller than the critical angle of total external reflection. More details about the GID technique can be found in textbooks [153, 155].

Experimental details

Details concerning sample preparation, x-ray specular diffraction and GID of the pentacene and the *para*-cyano-quaterphenylene thin films are described in Ref. [149] and Ref. [150], respectively.

The results of the GID experiments are typically presented as reciprocal space maps, i.e. diffraction patterns as a function of the q_z and the in-plane-component, q_{xy} of the scattering vector [152]. Indexation of these maps is performed by a visual comparison of calculated Bragg peak positions with the experimentally observed ones. The reliability of the structure solution is checked by comparing the calculated structure factors with the measured intensities. The structure factors used in this work are computed by the software package PowderCell [156] and corrected by Lorentzian L and polarization P_H factors taking the used experimental setup into account [150, 157].

8.2.2 Theoretical approach

Internal geometry optimization

The fact that bonding in molecular crystals is characterized by strong intramolecular and comparably weak intermolecular forces allows a division of the procedure of geometry relaxation into two steps. First, the internal geometry of the isolated molecule is relaxed. Then, following a procedure described below, the orientations of the molecules are optimized within the unit cell considering the molecules as rigid. The lattice parameters serve as the only input for this procedure and are provided by the indexation of the GID reciprocal space mapping.

Considering the molecules as rigid, the Euler angles are the natural choice for describing the molecular orientation within a cell. However, due to the layered

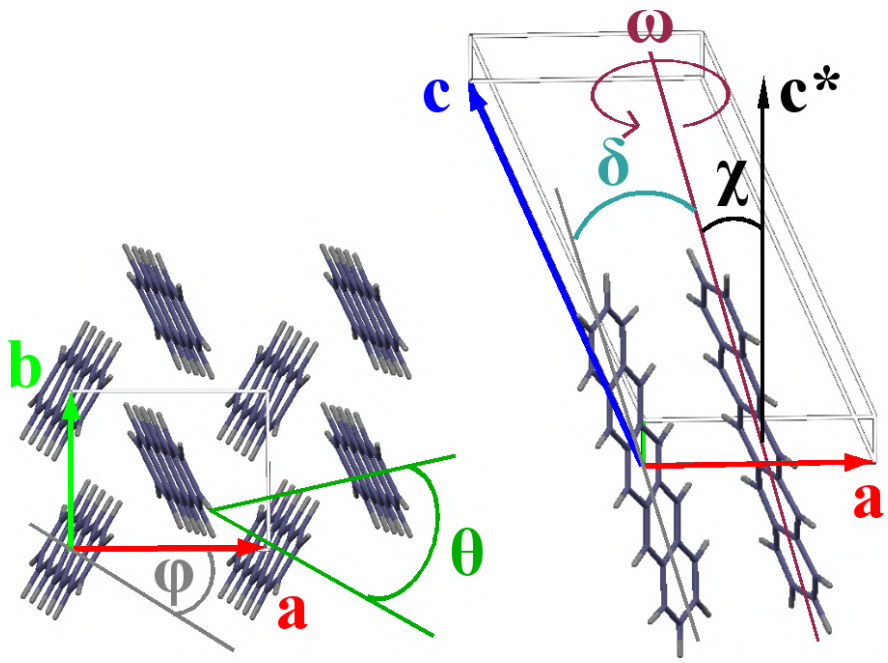

Figure 8.1: Crystal structure of pentacene. The herringbone arrangement of the molecules in the (**ab**) plane and the orientation angles are shown. ω describes a rotation of the molecule around a long molecular axis, χ is a tilting angle, and ϕ is a in-plane polar angle. θ stands for the herringbone angle and and δ is the angle between the long molecular axes of the two molecules inside the unit cell.

stacking of the molecules inside the molecular crystals, it is more convenient to use a definition of the angles as depicted in Figure 8.1. There, two angles define the orientation of the long molecular axis in a reference frame where the (**xy**) plane coincides with the herringbone plane (labeled **ab** plane in the figure), and the third axis is perpendicular to it (labeled **c***). These angles are the in-plane polar angle ϕ and the out-of-plane tilt angle χ. The third angle ω describes the rotation around the long molecular axis. The angle θ denotes the so-called herringbone angle, i.e. the angle between the normal vectors of the molecular planes of two inequivalent molecules, and δ is the angle between the long molecular axes of the two molecules inside the unit cell. This way the number of degrees of freedom required to describe the internal geometry of the molecular crystal is $3N$, where N is the number of inequivalent molecules. Making use of symmetry (the molecular crystals considered mostly have monoclinic space groups) and assumptions concerning possible molecular orientations inside the cell allows a reduction of this number. Hence, the procedure of the internal geometry optimization consists of the search for the minimum total energy as a function of these orientation angles.

Computational details

The computational procedure starts from the relaxation of the atomic positions inside the isolated molecule until the remaining atomic forces become less than 1 mRy/au. As mentioned in Chapter 5, isolated molecules are treated in the supercell approach. As a next step, a series of crystal structures (with the lattice parameters fixed according to experiment) is generated which differ by the orientation of the two inequivalent molecules inside. Now a number of numerical methods can be used to search for the minima of the energy surface. However, the knowledge of well-defined bulk crystal structures can serve as a very good starting point in the search for thin film polymorphs. Exploring the subspace of the orientation angles close to those of the known structures provides a rather fast and reliable way to find the structural solution. Such a relaxation procedure has been proven successful for structure optimization of anthracene under pressure [158] and is outlined in the following: First, the total energy of the crystal is minimized by rotating the inequivalent molecules around their respective long axes and keeping the values of the polar angles constant. Subsequently, one fixes the value of ω corresponding to the minimum energy and successively change the angles χ and ϕ. As a final step for the internal geometry minimization, the atomic positions of the molecules are allowed to relax again such that the remaining forces are below 1 mRy/au.

All calculations are performed using QUANTUM-ESPRESSO [85]. Ultrasoft pseudopotentials [94] with a plane-wave energy cutoff of 40 Ry are employed. Exchange and correlation effects are treated by PBE [50]. Brillouin zone integrations are carried out by the Monkhorst-Pack scheme [95] with a $4 \times 4 \times 3$ mesh.

8.3 Crystal and electronic structure of pentacene thin films

8.3.1 Motivation

Pentacene is one of the most prominent materials used in organic electronics (Chapter 2). The high reproducibility of thin films by vacuum deposition of the molecules combined with advantageous electronic properties like high mobilities make them perfect candidates for exploration in the construction of organic devices [159].

The growth of pentacene films shows a variety of crystalline phases, where three different polymorphic structures have been reported [160, 161]. Only for two structures, namely the Campbell or "bulk" phase [162], and the so-called "single

crystal" phase [163, 164], complete structural solutions have been known. Although the thin film phase is crucial for the charge transport within thin film transistors, the geometry of this structure is still subject of ongoing research [165, 166]. The reason is that it is only formed on isotropic surfaces and the subsequent appearance of a pentacene bulk phase [167, 168] does not allow for the growth of single crystals of a size sufficient for a full structure solution. Moreover, isotropic surfaces like silicon oxide or polymer surfaces lead to the formation of domains in the thin film phase with a preferred orientation of the crystallites with the crystallographic (001) plane oriented parallel to the substrate surface [169, 170].

Therefore, the combined experimental / theoretical approach for determining thin film phases provides a good tool for resolving the details of the pentacene thin film phase, and, in fact, led to a successful determination of the crystalline parameters as will be seen below.

8.3.2 Experimental facts

The specular x-ray diffraction scans reveal the typical diffraction features of a pentacene thin film grown on silicon oxide [171, 172]. Two series of diffraction peaks are observed. The dominating ones arise from an interplanar distance $d_{001} = 1.544 \pm 0.003$ nm which can be identified as the $00L$ peaks of the thin film structure. This observed value is in excellent agreement with literature data [139]. The second peak series is of much lower intensity and comes from an interplanar distance of 1.443 ± 0.003 nm. This value does not fit to the "single crystal" structure obtained by Holmes [163, 164], but is close to $d_{001} = 1.450$ nm of the "bulk" structure of Campbell [162]. The presence of the Campbell's structure besides the thin film structure has already been proven experimentally [173].

The grazing incidence diffraction studies reveal randomly distributed crystallites (two-dimensional powder). A typical diffraction pattern is depicted in Fig. 8.2. The diffraction peaks marked by crosses are calculated positions arising from the Campbell structure taking into account the preferred orientation of the crystallites. All expected peaks with sufficiently high intensity are observed, which reveals that the Campbell structure is definitely present in the film.

The residual peaks can be used for an indexation of the pentacene thin film phase. Since the sample shows a strong (001) preferred orientation, the observed q_{xy} values of the diffraction peaks can be used to determine the Miller indexes hk according to literature data [174]. Also considering the q_z part of the diffraction peaks the complete indexation of hkl were obtained by determining the unit cell parameters of the reciprocal lattice. The fact that the length of the reciprocal unit cell vector $\mathbf{c}^*$ is known accurately from the specular scan simplified the indexation

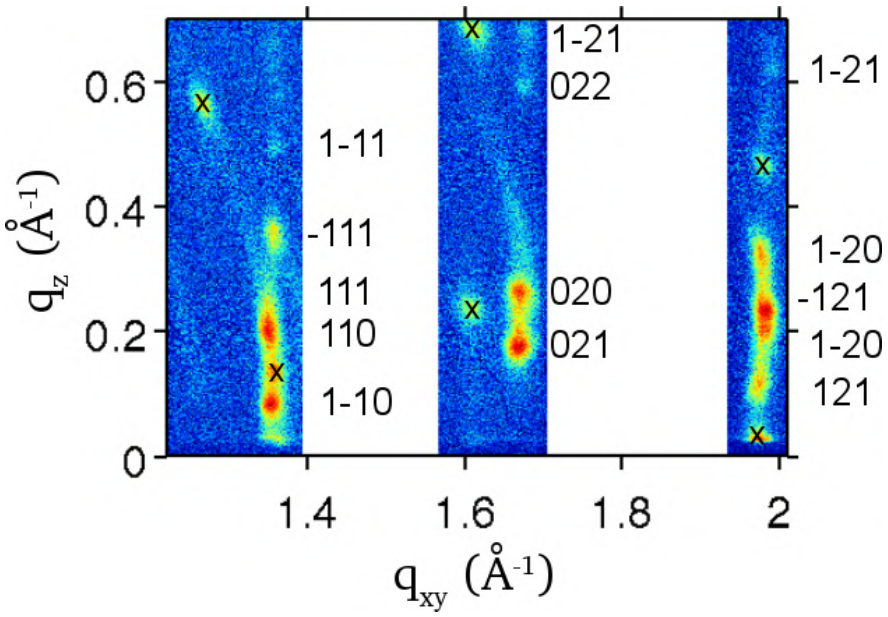

Figure 8.2: Grazing incidence diffraction pattern of a 180 nm thick pentacene thin film, where the intensities of the diffraction spots are square-root scaled. Diffraction spots arising from the Campbell phase are marked by crosses. The indexes of the diffraction peaks are given only for the thin film phase. This picture is taken from Ref. [149].

procedure considerably [175]. The obtained lattice constants are $a = 0.592$ nm, $b = 0.754$ nm, $c = 1.563$ nm, $\alpha = 81.5°$, $\beta = 87.2°$, and $\gamma = 89.9°$ and are compared with those of the Campbell phase in Table 8.1. The values are quite close to data obtained from electron diffraction on microcrystals [176] and are in excellent agreement with results of other recent x-ray diffraction experiments [165, 166].

8.3.3 Geometry relaxation

Since the pentacene crystal has triclinic symmetry, the procedure of internal geometry optimization requires a search for the total energy minimum in a 6-dimensional space. However, using assumptions regarding possible orientations of the molecules inside the crystal as described below, this number of degrees of freedom can be reduced to only three, i.e. the angles θ, ϕ, and χ, depicted in Fig. 8.1.

From the existing experimental structure data of the pentacene polymorphs it is known that the angle between the long molecular axes (in our notation δ) does not exceed 1.5° [161]. Due to this fact we only consider those geometries

Table 8.1: Triclinic lattice parameters a, b, c, α, β, γ, and the unit cell volume V of the thin film pentacene polymorph as determined from x-ray measurements. For comparison the lattice constants of Ref. [165] and Ref. [166] as well as the bulk phase (Ref. [162]) are given. A different choice of the unit cell vectors for the bulk phase with respect to Ref. [162] is used.

Phase	a(nm)	b(nm)	c(nm)	α(deg)	β(deg)	γ(deg)	V(nm^3)
Thin film:							
This work [149]	0.592	0.754	1.563	81.5	87.2	89.9	0.689
Yoshida et al. [165]	0.593	0.756	1.565	98.6	93.3	89.8	0.693
Schiefer et al. [166]	0.5958	0.7596	1.561	81.25	86.56	89.80	0.697
Bulk [162]	0.606	0.790	1.501	81.6	77.2	85.8	0.692

as a starting point for the optimization, where the long molecular axes of both inequivalent molecules are parallel. Moreover, the herringbone style of packing suggests a rotation of both pentacene molecules around their long molecular axes in a consistent way, i.e. the first molecule is rotated by the angle $\theta/2$ and the second one by the angle $-\theta/2$. One should note that during the final relaxation of the atomic positions, the molecule as a whole is allowed to rotate by some small angle. Therefore, after this last relaxation step the two inequivalent molecules do not necessarily have the same orientation with respect the long axes anymore leading to δ slightly deviating from 0°.

To estimate the accuracy of our two-step procedure for the geometry optimization as described above, the approach has been tested for the pentacene bulk structure, for which the internal geometry is well known [162]. For this purpose two pentacene molecules have been placed in a unit cell with experimental lattice parameters determined by Campbell. Results of this procedure are plotted in Fig. 8.3, and the optimal values of the orientation angles are compiled in Table 8.2. The comparison of the experimental and optimized internal geometry in shows good agreement and allows us to reliably apply this optimization procedure to the search for the internal geometry of the thin film phase. The biggest deviation of about 2° is observed for θ and δ which might be explained by the fact that we have omitted the degrees of freedom connected with the inequivalence of the two pentacene molecules in the optimization procedure. This deviation, hence, can be regarded as an error bar of the optimization procedure.

Starting from the lattice parameters as measured by x-ray diffraction (Table 8.1), the optimization of the molecular orientations of the unknown thin film phase is performed using an analogous search algorithm as described above. The results are given in Table 8.2. The comparison with the bulk phase data shows the following characteristic features (see Fig. 8.4). First of all, there is a pronounced

Table 8.2: Calculated orientation angles of the molecules in bulk and thin film pentacene in comparison with experimental data for the bulk phase. The total energies for both structures are shown in the last row.

	Bulk (exp)[a]	Bulk (opt)	Thin film (opt)
θ (deg)	52.5	50.9	54.1
χ_1 (deg)	22.4	21.9	3.1
χ_2 (deg)	20.5	20.9	2.9
δ (deg)	2.2	1.0	0.3
E_{total} (Ry)	-533.8978	-533.8976	-533.8973

[a] Ref. [162]

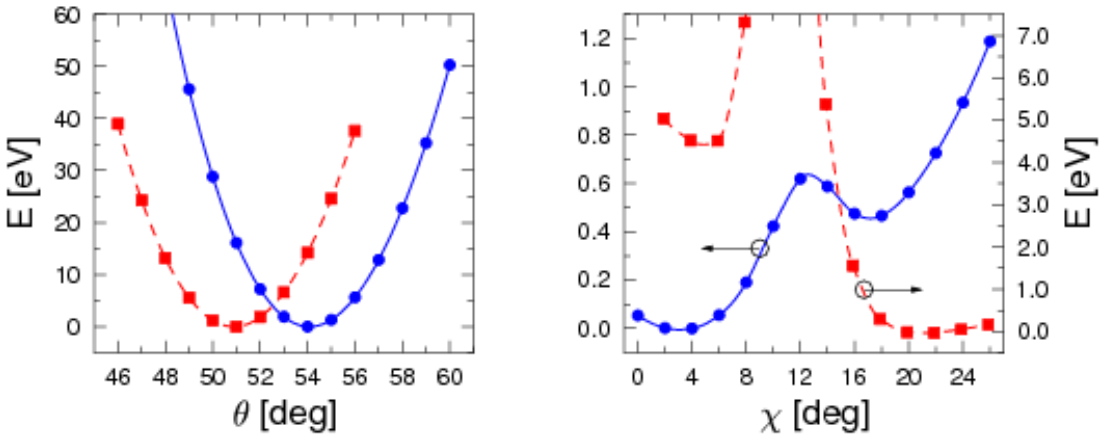

Figure 8.3: Total energies of the thin film phase (blue line) and the bulk phase (red line) as a function of the herringbone angle θ (left) and the tilt χ angle (right). The origin of the energy scale is taken at the absolute energy minimum of the respective curve.

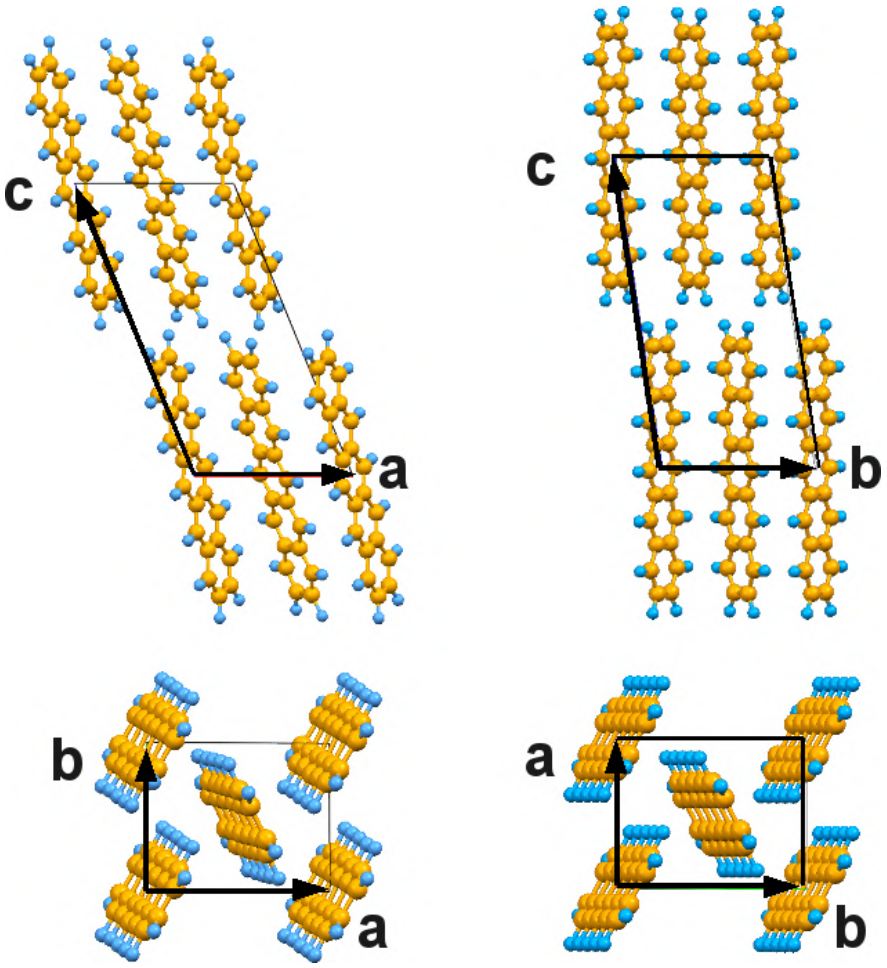

Figure 8.4: Crystal structure of the bulk (left) and the thin film phase of pentacene (right).

difference in the tilt angle χ, which is $\approx 20°$ for the bulk and only $\approx 3°$ for the thin film phase. The main reason for this behavior can be found in the smaller interlayer separation of the bulk phase (1.45 nm) as compared to the thin film phase (1.543 nm). On the other hand, the herringbone angle $\theta = 54°$ for the thin film phase is close to the corresponding quantity for the oligoacene series ($\approx 52°$), where the a and b lattice parameters are almost constant.

Another interesting feature is the dependence of the total energy on the tilt angle. The presence of two local minima at about 3° and 18° for the thin film phase is clearly observed. This behavior is seen for the bulk phase as well, where the minima are located at $\approx 5°$ and $\approx 21°$. In contrast to the thin film phase, the deepest minimum is the second local minimum at a tilt angle of 22°. Moreover, different energy barriers between the minima are revealed. For the thin film phase this barrier is about 0.4 eV, whereas for the bulk phase it is an order of magnitude

larger (about 5 eV). Comparing the total energies of the two structures one can observe that the energy difference is only 6.5 meV, which shows that both phases are likely to coexist in the real material.

The revealed thin film structure of pentacene is in good agreement with other studies performed concurrently by Yoshida *at al.* [165] and Schiefer *et al.* [166]. Using x-ray diffraction, the former group has determined lattice parameters very close to the ones reported by us. Their theoretical investigations of the internal molecular geometry by means of an empirical force field method revealed a herringbone angle of 50° and tilting angles of 5.7° and 6.8°, respectively. The latter group independently performed GID measurements on a pentacene thin film deposited on different substrates. Their results for 5A on SiO_2 revealed similar cell parameters. To determine the molecular arrangement, a fit of calculated x-ray intensities to the measured ones was performed in Ref. [166]. In this way, a herringbone angle of 54.3° and tilting angles of 5.6° and 6.0° were found.

8.3.4 Comparison between theory and experiment

Based on the theoretically determined molecular packing, a diffraction pattern is computed and compared with line scans at constant q_{xy} from the experimental diffraction pattern in Fig. 8.5. The intensities are calculated with the assumption of randomly distributed crystallites. In Fig. 8.5 the theoretical powder spectra for two different molecular orientations characterized by $\chi = 3°$ (black bars) and $\chi = 18°$ (gray bars) are compared with the experimental data (lines). An overall good agreement with experiment is found only for the theoretical intensities corresponding to the $\chi = 3°$ case. In particular, the most pronounced diffraction peaks, namely (1-10), (110), (021), and (020), strongly favor this solution, which is also the optimal structure from the DFT total energy point of view. At $\chi \approx 18°$, on the other hand, the (1-10), (110) and (021) reflections are considerably underestimated while the (020) is predicted to be highest in intensity. Also the relative intensities of (1-10) vs. (110) and (021) vs. (020) are in excellent agreement only for the 3° structure. There remain some small deviations between calculated and experimental intensities, e.g. the ratio between the (-121) and (121) peak heights (Fig. 8.5c). This can be explained by the fact that the peak height of (121) is decreased due to peak broadening, but the overall intensities are comparable with the relative intensities given by the bars. From theoretical considerations, the differences in the diffraction intensities can be caused by neglecting additional degrees of freedom in the structure optimization procedure as outlined in the previous section.

Finally, one should note that the calculations above have been carried out by standard xc potentials, i.e. the PBE. As mentioned earlier, this is justified when only internal degrees of freedom are concerned. However, it would be desirable for future work to carry out such investigations with more advanced techniques as

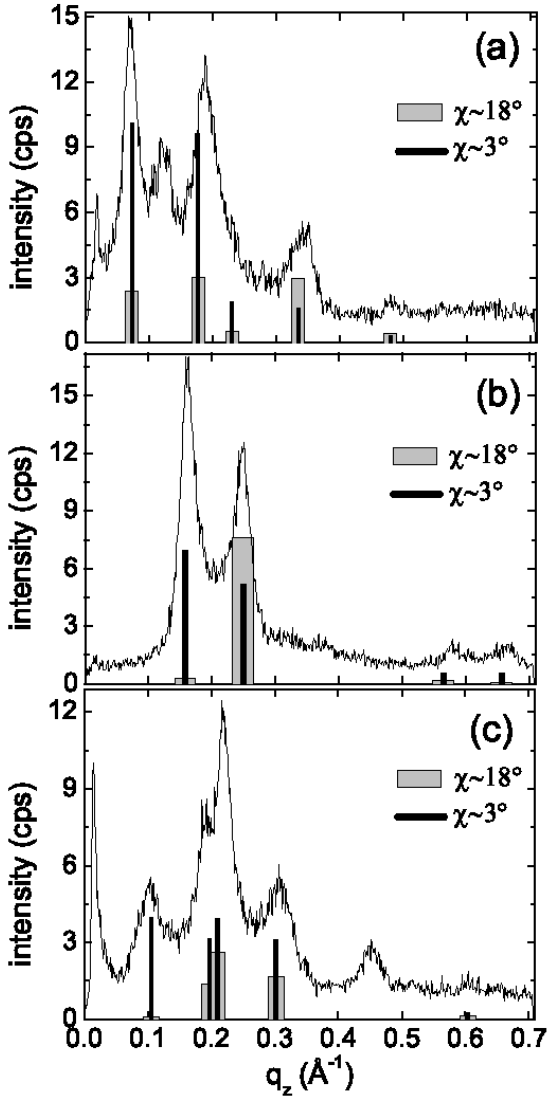

Figure 8.5: Integrated diffraction intensities of Fig. 8.2 taken in the q_{xy} range (1.33, 1.38) (a), (1.63, 1.70) (b) and (1.93, 2.01)(c) and normalized to a single line scan. Calculated peak positions and relative intensities are given by bars for the two structural solutions $\chi \approx 3^\circ$ and $\chi \approx 18^\circ$.

the vdW-DF in order to evaluate nonlocal correlation effects on the conformation of molecules inside the unit cell. Even if the changes are expected to be not significant, they could clarify the remaining small discrepancies with respect to experimental results.

8.3.5 Electronic band structure

Starting from the structure solution found for the thin film phase as described in the previous sections and the structural data of the Campbell phase, we calculated and compared the electronic structures of both polymorphs. The band structure calculations were carried out for a path in the Brillouin zone connecting the high-symmetry points X, Γ, Y, C, and Z with the internal coordinates of these points being (0.5,0,0), (0,0,0), (0,0.5,0), (0.5,0.5,0), and (0,0,0.5) in units $(2\pi/a,2\pi/b,2\pi/c)$. Note that the $\overline{\Gamma Z}$ direction is normal to the **ab**-plane, i. e. perpendicular to the pentacene layers. Since all triclinic angles are close to 90°, the $\overline{\Gamma X}$ and $\overline{\Gamma Y}$ directions are almost parallel to the crystal **ab** plane, hence, reflect the in-plane dispersion. For the calculation of the density of states (DOS) the **k** space integration was performed by the improved tetrahedron method [177] with a $6 \times 6 \times 4$ mesh.

The results are shown in Fig. 8.6. The subbands corresponding to the uppermost valence band (VB) and the lowest conduction band (CB) pairs, as well as their corresponding density of states (DOS), are displayed in green. One should mention that in the original determination of the Campbell structure, a different setup of the unit cell was used. Here another set of basis vectors is chosen allowing for a direct comparison with the thin film phase (see Table 8.1). The most distinct features of the two band structures are summarized in Table 8.3. The band structure of the thin film phase exhibits a more dispersive character. A denser packing of the molecules in the (**ab**) plane leads to stronger intermolecular interaction. This is responsible for the fact that the bandwidths of both the conduction and the valence bands are significantly enhanced. This finding should have significant impact on the charge carrier mobilities. In particular, we observe a valence bandwidth twice as large as compared to the corresponding bulk polymorph. The largest splittings of the VB and CB of the thin film phase is observed at the Γ point, while in bulk pentacene this is at the C point. The top of the valence band of the thin film polymorph is situated at (0.7, 0.0, 0.0). It is noteworthy that the Kohn-Sham band gap of the thin film phase (0.70 eV) is only slightly smaller than that of the bulk phase (0.74 eV), for which similar values have been reported previously [92, 178]. In both cases, the gap is a direct one.

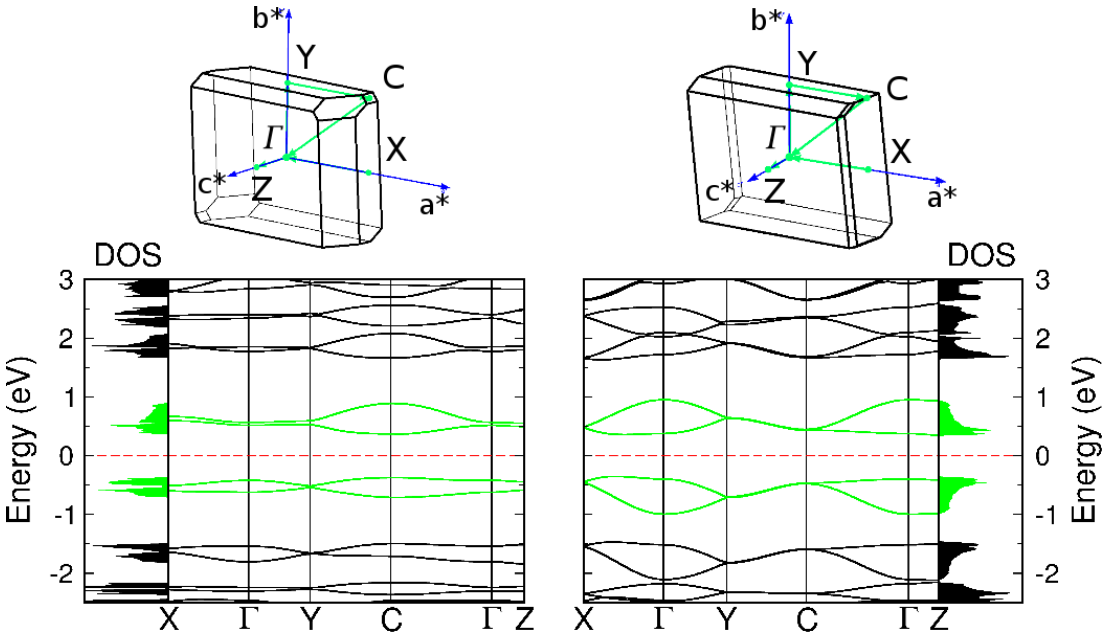

Figure 8.6: Calculated band structures for the bulk (left) and thin film (right) pentacene polymorphs. The high-symmetry points in units (2π/a,2π/b,2π/c) are Γ=(0,0,0), X=(0.5,0,0), Y=(0,0.5,0), C=(0.5,0.5,0), and Z=(0,0,0.5). The Fermi level is indicated by a red dashed line. The subbands of the VB and CB as well as their DOS are given in green. On top the corresponding Brillouin zones are presented.

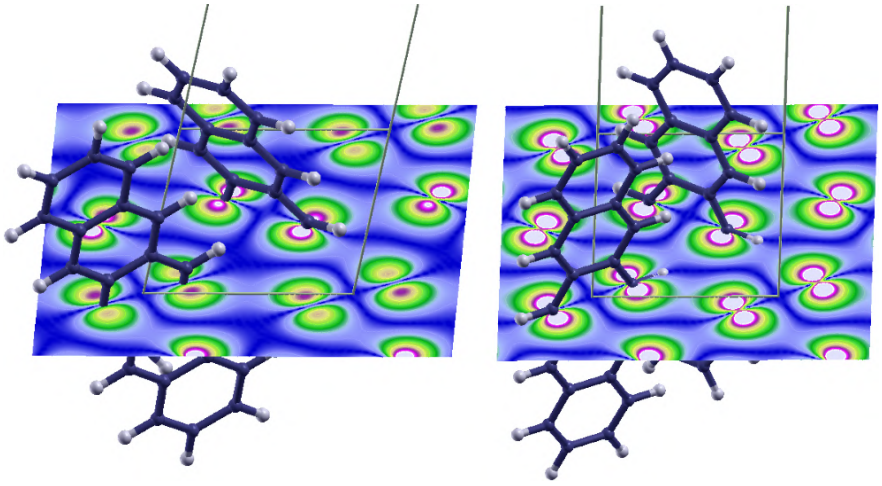

Figure 8.7: Highest occupied molecular orbital (HOMO) of the bulk phase (left) and the thin film structure (right) of pentacene.

	Thin film	Bulk
Kohn-Sham band gap	0.70 eV	0.74 eV
Band width		
VB	0.64 eV	0.34 eV
CB	0.62 eV	0.53 eV
Band gap at point		
Γ	0.77 eV	0.93 eV
C	0.90 eV	0.89 eV

Table 8.3: Calculated Kohn-Sham energy gap and band widths of the highest occupied and the lowest unoccupied pairs of bands for both crystal 5A structures. Additionally, the band gaps calculated at the k points Γ and C are given.

8.4 Crystal structure of CNHP4 thin film

8.4.1 Motivation

Thin films formed by oligophenylene molecules are highly reproducible and chemically stable at ambient conditions. They show optical fluorescence in the blue-visible regime, which is relevant for organic light emitting applications [179, 180]. In particular, *para*-quaterphenylenes are of interest because appropriately functionalized they show enhanced second harmonic generation [181]. In addition, if they are grown epitaxially on muscovite mica or TiO_2, oriented crystalline nanofibers are formed, making them suitable for integration in nanoscaled photonic devices [182, 183].

Within this section the combined experimental and theoretical approach described above is now applied to solve the unknown crystal structure of *para*-cyano-quaterphenylene thin films.

8.4.2 Experimental facts

The *para*-cyano-quaterphenylene (CNHP4) molecule is shown in Fig. 8.8. It consists of four phenyl rings and is terminated on one end by a cyano group. The molecule does not have inversion symmetry which gives rise to the phenomenon of second-harmonic generation. The presence of nitrogen atom leads to a rather inhomogeneous charge distribution in comparison with the quaterphenylene case with charge accumulation at the cyano group. Because of this, one can expect antiparallel orientation of the inequivalent molecules in the bulk phase.

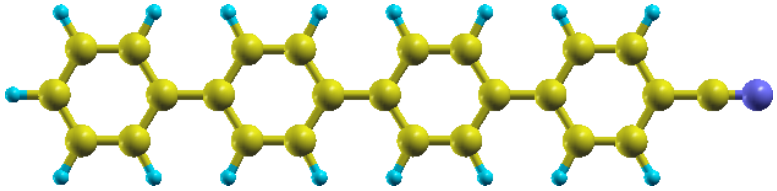

Figure 8.8: The *para*-cyano-quaterphenylene (CNHP4) molecule, where carbon, hydrogen, and nitrogen atoms are marked by the yellow, light blue spheres, and dark blue color, respectively.

Specular scans of CNHP4 thin films prepared under different conditions [150] have revealed interplanar distances which are close to the van der Waals length of the CNHP4 molecule (22.4 Å). This result suggests that the molecules have an upright standing orientation relative to the substrate surface or are slightly tilted and shifted against each other. Moreover, the observation of slightly different interplanar distances (values between 20.7 Å and 23.2 Å) demonstrates the tendency of the molecule to form polymorph phases.

GID experiments performed by Armin Moser Ref. [150] revealed unit cell parameters of $a = 5.56$ Å, $b = 7.67$ Å, $c = 20.85$ Å, and $\beta = 97.4°$ which explained all experimentally observed diffraction spots and the Debye-Scherrer rings. A very detailed description of this indexation procedure can be found in Refs. [150, 152]. From mass density considerations, the presence of two molecules within the unit cell has been deduced. The magnitude of the unit cell parameters a and b together with the fact that the three strongest peaks are indexed with 110, 020 and 120 led to the conclusion that the molecules pack in a herringbone pattern. The presence of those peaks close to the in-plane direction suggest upright standing molecules, as already concluded from the specular measurement. Comparing crystal structures of similar molecules [184] shows that oligophenylene-based molecules with cyano endgroups always arrange in a herringbone pattern with neighboring molecules oriented antiparallel to each other. The space group $P2_1$ was assumed, since it represents the only possibility to generate such a herringbone packing.

8.4.3 Geometry relaxation

The crystal symmetry, $P2_1$, suggested by experiment provides a big advantage for the simulations. It allows the consideration of the three orientation angles as the only degrees of freedom.

Following the algorithm described in detail in Sec. 8.2.2, three possible candidates for the CNHP4 thin film structure have been found. The energy profiles obtained from the ab-initio calculations in the region around to global minimum are shown

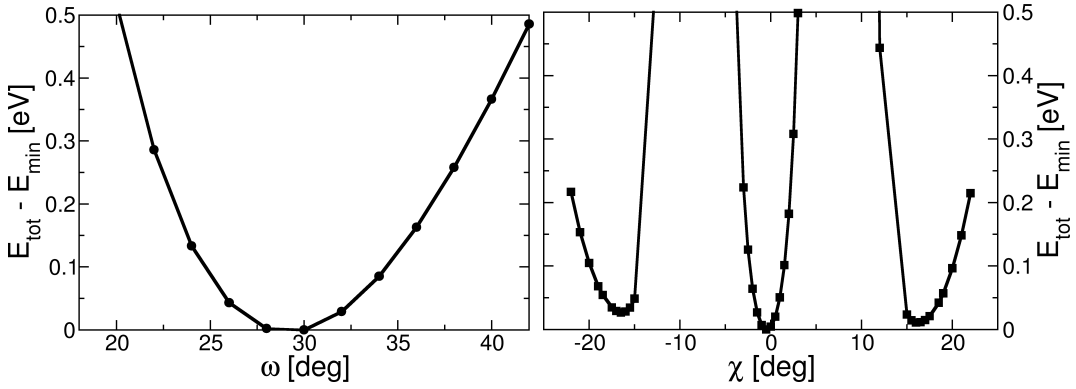

Figure 8.9: Energy dependence of the packing of the *para*-cyano-quaterphenylen molecules on the rotation angle ω (a) and tilt of the molecules within the herringbone layer (b).

in Fig. 8.9. In both plots an energy scale relative to the global minimum is used. The left panel shows the dependence of total energy on the angle ω at fixed ϕ and χ. Only one minimum at $\omega \approx 30°$ is observed. This is not the case for the energy as a function of the tilting angle χ at fixed values of the other angles (right panel). Here, the total energy has three minima that are located at $\chi \approx 0°$ and $\chi \approx \pm 16°$. The global energy minimum corresponds to $\chi \approx 0°$ which means that the long molecular axis is perpendicular to the herringbone layers, i.e. to the (001) plane, and is in agreement with the experimental observation. Since the theoretical considerations reveal three possibilities of molecular arrangement with very similar energy minima (the difference is only about 10 meV), one has to compare the calculated structure factors with the experimental intensities in order to find the final solution.

8.4.4 Comparison between theory and experiment

A comparison of the experimental intensities with the calculated structure factors is shown in Fig. 8.10 for two solutions ($\chi \approx 0°$ and $\chi \approx \pm 16°$). The one with $\chi = 16°$ is nearly identical to that for $\chi = 16°$ and is, therefore, not displayed. The case of $\chi = 0°$ fits considerably better than the solution for $\chi = 16°$. This is clearly visible for the 11L rod in the in-plane direction ($q_z \approx 0$) (Fig. 8.10). The agreement between the measured and calculated intensities for $\chi = 0°$ is good but not perfect. A few calculated structure factors are slightly overestimated. E.g., the peak at $q_p \approx 4$ Å^{-1} and $q_z \approx 0$ seems to be too large. Probably, the assumption of a planar molecule and the separated herringbone layers without interpenetration of the molecules is not strictly fulfilled. A sketch of the molecular packing corresponding to both solutions, $\chi = 16°$ and $\chi = 0°$, is shown in Fig. 8.11.

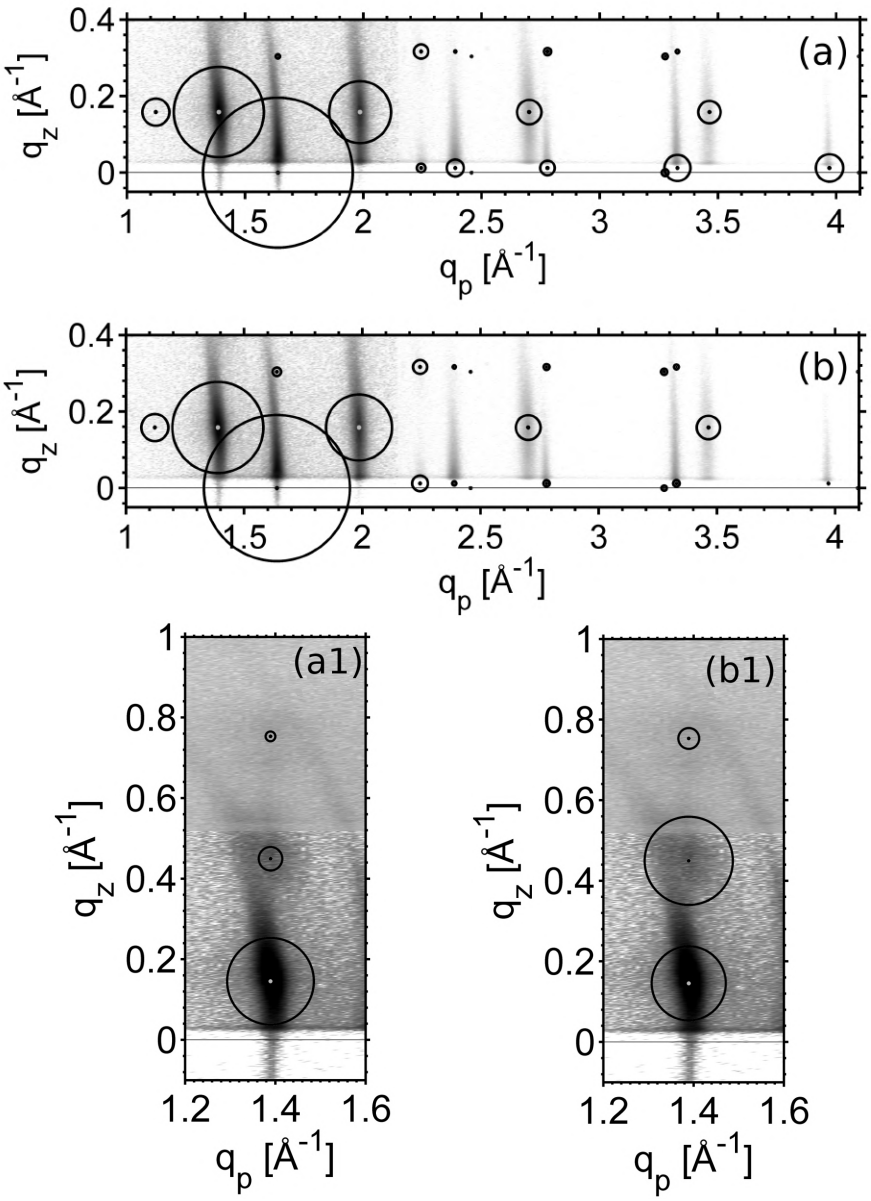

Figure 8.10: Comparison of structure factors based on the calculated molecular packing with the experimental results taken from Ref. [150]. The solution for $\chi = 0°$ (a and a1) is compared with that for $\chi = 16°$ (b and b1). The radius of the ring around each calculated peak position is proportional to the magnitude of the structure factor.

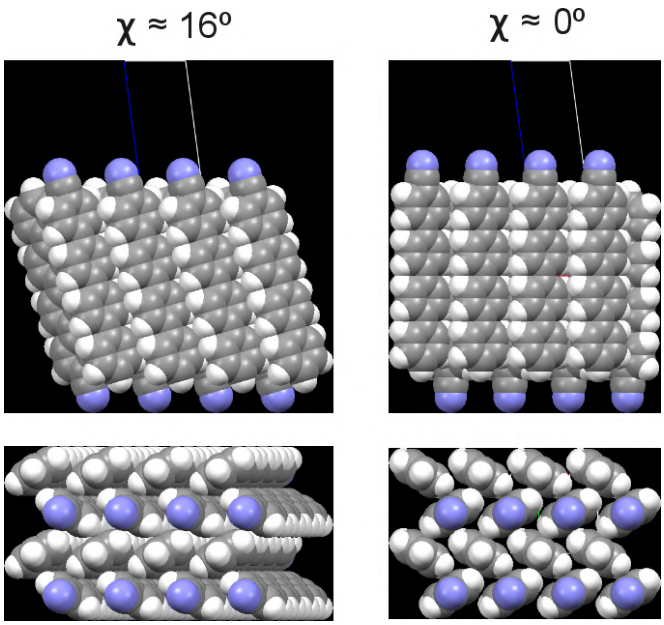

Figure 8.11: Theoretically obtained CNHP4 molecular crystal structures corresponding to $\chi = 16°$ and $\chi = 0°$ values of the tilting angle. Solution $\chi = 0°$ corresponds closely to experiment regarding the comparison of diffraction intensities.

8.5 Conclusions

A combined experimental and theoretical approach has been successfully applied to find the crystal structures of surface-mediated thin films formed by pentacene and *para*-cyano-quaterphenylene molecules. This approach allows resolution of the structure solution of such surface-mediated phases that are limited to the first layers of thin films where standard structure solution methods cannot be applied. Lattice parameters taken from GID measurements together with auxiliary experimentally provided data about number of inequivalent molecules and space group symmetry has served as the input for a theoretical procedure to reveal the molecular packings within the crystal cell.

The procedure has been tested by a comparison with the well-known pentacene bulk crystal structure as determined by Campbell [162], and reasonable agreement for theoretically predicted and experimentally observed molecular orientations has been achieved. The solution found for the pentacene thin film phase is characterized by the same herringbone packing of two inequivalent molecules with the corresponding herringbone angle close to that of the bulk crystal phase. The most pronounced difference is in the value of the tilt angle between the long molecular axis and the normal to the **ab** plane. While this angle is approximately 3° for the thin film phase, it is about 22° for the bulk polymorph. These findings are in good agreement with other recent studies [165, 166]. Almost upright pen-

tacene orientation within a layer in the thin film phase leads to more enhanced intermolecular $\pi - \pi$ overlap and more dispersive valence and conducting bands and hence lower values of the effective hole and electron masses. For instance, the band width of the topmost valence band is twice as large in the thin film phase as compared to the Campbell single crystal structure. These findings are important for understanding the electro-optical properties of devices based on pentacene thin films. Since the active channel in these organic field effect transistors most likely is composed of pentacene molecules in the thin film phase, the structural solution, and the corresponding electronic properties of this phase provided herein, will be highly relevant. Therefore, attempts to understand the charge transport in pentacene should start from the correct underlying structure.

In the case of the CNHP4 thin film, the theoretical structure optimization has revealed two polymorphs that have almost the same total energy but differ in the value of the tilting angle χ. The first solution, as in the case of the pentacene thin film phase, shows almost upright $\chi \approx 0^\circ$ standing molecular packing, while the second one demonstrates a configuration of the molecules tilted by the angle $\chi \approx 16^\circ$. Finally, from comparison of calculated structure factors with the experimentally obtained intensities the $\chi \approx 0^\circ$ case has been selected as the optimal solution.

The approach presented here is of great value since it is likely the only mean to find crystal structures of thin molecular films. Therefore this method will be further explored and developed. One of possible improvements can be to use an efficient algorithm for the numerical search of energy minima in a multidimensional space in which not only orientation angles but any number of additional degrees of freedom (e.g. torsion angles, positions of molecules within a cell etc.) can be easily included.

Acknowledgement

At this point, I would like to acknowledge all people whose support and participation have been important for me during all period of my PhD.
The main words of gratitude I would like to convey to my supervisor Claudia Ambrosch-Draxl. Her enthusiasm, inexhaustible energy and responsive guidance has made my study and work under thesis very interesting and unforgettable. I would particularly like thank Claudia for her great support and patience by formulating and writing this thesis.
I'm extremely grateful to Peter Puschnig for his scientific and simply friendly advice and suggestions which has always been very valuable for me. Additionally, I'd like to thank Peter for his very kind help in the preparation of the manuscript.
I want to express my gratitude to all my co-authors and colleagues from the NFN project, especially to Priya Sony and Lorenz Romaner for our fruitful discussion regarding the adsorption molecules on metal substrates, and Prof. Roland Resel and Prof. Christian Teichert for providing a link between theory and experiment.
Particular gratitude to everyone who has contributed to reading and correcting my thesis, especially to Stephen Berkebile who has been so kind to find the time for reading the thesis and making important remarks concerning my English.
The financial support of Austrian National Research Network (NFN) project "Interface controlled and functionalized organic films" is also gratefully acknowledged.
I'd like to say a very big thank to the "Chair of atomistic modeling and design of materials" for creating an excellent working atmosphere.
And finally, my last but not least gratitude to my parents and especially my wife for their patience, help and steady encouragement during all this time.

List of Abbreviations

nA	Oligoacenes
nP	Oligophenylenes
nT	Oligothiophenes
1T	Thiophene ring
ACF	Adiabatic Connection Formula
CB	lowest Conduction Band
CCSD(T)	Coupled-Cluster with Single and Double and Perturbative Triple excitations
CNHP4	*para*-cyano-quaterphenylene
CPU	Central Processing Unit
DFT	Density Functional Theory
DOS	Density Of States
ECS	Equilibrium Crystal Shape
GGA	Generalized Gradient Approximation
GID	Grazing-Incidence x-ray Diffraction
HOMO	Highest Occupied Molecular Orbital
LDA	Local-Density Approximation
LUMO	Lowest Unoccupied Molecular Orbital
MC	Monte-Carlo integration
MP2	Møller-Plesset theory
NTCDA	1,4,5,8-naphthalene-tetracarboxylic-dianhydride
OFET	Organic Field Effect Transistor
OLED	Organic Light Emitting Diode
PBE	Perdew-Burke-Ernzerhof GGA
PTCDA	3,4,9,10-perylene-tetracarboxyl acid diahydride
PW91	Perdew-Wang 91 GGA
revPBE	Zhang-Yang revised PBE GGA
RPA	Random Phase Approximation
VB	uppermost Valence Band
vdW	van der Waals
vdW-DF	van der Waals Density Functional
vdWse	vdW semiempirical correction
XSW	X-ray Standing Wave experiment

List of Figures

List of Tables

Bibliography

[1] J. M. Shaw, P. F. Seidler, *IBM. J. Res. & Dev.* **45**, 3 (2001).

[2] H. Klauk, ed., *Organic Electronics: Materials, Manufacturing and Applications* (Wiley-VCH, Wienheim, 2006).

[3] K. Müllen, U. Scherf, eds., *Organic Light Emitting Devices. Synthesis, Properties and Applications.* (WILEY-VCH, Weinheim, 2006).

[4] I. Kymissis, *Organic Field Effect Transistors: Theory, Fabrication and Characterization* (Springer, Berlin, 2009).

[5] C. J. Brabec, V. Dyakonov, J. Parisi, N. S. Sariciftci, eds., *Organic Photovoltaics* (Springer, Berlin, 2003).

[6] D. Bernards, R. Owens, G. Malliaras, eds., *Organic Semiconductors in Sensor Applications* (Springer, Berlin, 2008).

[7] I. D. Dzyaloshinskii, E. M. Lifshitz, L. P. Pitaevskii, *Usp. Fiz. Nauk* **73**, 381 (1961).

[8] S. Grimme, *J. Comp. Chem.* **27**, 1787 (2006).

[9] J. F. Dobson, J. Wang, *Phys. Rev. Lett.* **82**, 2123 (1999).

[10] M. Dion, H. Rydberg, E. Schroeder, D. C. Langreth, B. I. Lundqvist, *Phys. Rev. Lett.* **92**, 246401 (2004).

[11] A. Marini, P. Garca-Gonzlez, A. Rubio, *Phys. Rev. Let.* **96**, 136404 (2006).

[12] J. Harl, G. Kresse, *Phys. Rev. B* **77**, 045136 (2008).

[13] D. C. Langreth, B. I. Lundqvist, S. D. Chakarova-Käck, V. R. Cooper, M. Dion, P. Hyldgaard, A. Kelkkanen, J. Kleis, L. Kong, S. Li, P. G. Moses, E. Murray, A. Puzder, H. Rydberg, E. Schröder, T. Thonhauser, *J. Phys.: Condens. Matter* **21**, 084203 (2009).

[14] H. Rydberg, B. I. Lundqvist, D. C. Langreth, M. Dion, *Phys. Rev. B* **62**, 6997 (2000).

[15] A. Puzder, M. Dion, D. C. Langreth, *J. Chem. Phys.* **124**, 164105 (2006).

[16] T. Thonhauser, A. Puzder, D. C. Langreth, *J. Chem. Phys.* **124**, 164106 (2006).

[17] S. D. Chakarova-Käck, E. Schröder, B. I. Lundqvist, D. C. Langreth, *Phys. Rev. Lett.* **96**, 146107 (2006).

[18] E. A. Silinsh, *Organic Molecular Crystals* (Springer, Berlin, 1980).

[19] M. Pope, C. E. Swenberg, *Electronic Processes in Organic Crystals and Polymers* (Oxford University Press, New York, USA, 1999).

[20] D. Williams, M. Schadt, *Proc. IEEE (Lett.)* **58**, 476 (1970).

[21] C. K. Chiang, C. R. Fincher, Y. W. Park, A. J. Heeger, H. Shirakawa, E. J. Louis, S. C. Gau, A. G. MacDiarmid, *Phys. Rev. Lett.* **39**, 1098 (1977).

[22] T. Scotheim, ed., *Handbook of Conducting Polymers* (M. Dekker, New York, 1986).

[23] P. M. Borsenberger, D. S. Weiss, *Organic Photoreceptors for Imaging Systems* (M. Dekker, New York, 1993).

[24] C. W. Tang, *Appl. Phys. Lett.* **48**, 183 (1986).

[25] J. H. Burroughes, C. A. Jones, R. H. Friend, *Nature* **355**, 137 (1988).

[26] H. Koezuka, A. Tsumara, T. Ando, *Synth. Met.* **18**, 699 (1987).

[27] G. Horowitz, D. Fichou, X. Z. Peng, Z. Xu, F. Garnier, *Solid State Commun.* **72**, 381 (1989).

[28] M. E. Gershenson, V. Podzorov, A. F. Morpurgo, *Rev. Mod. Phys.* **78**, 973 (2006).

[29] M. Schwoerer, H. C. Wolf, *Organic Molecular Solids* (Wiley-VCH, Weinheim, 2007).

[30] W. Brütting, ed., *The physics of Organic Semiconductors* (Wiley-VCH, Weinheim, 2005).

[31] K. Hummer, P. Puschnig, C. Ambrosch-Draxl, *Phys. Rev. Lett.* **92**, 147402 (2004).

[32] P. Puschnig, C. Ambrosch-Draxl, *Phys. Rev. B* **66**, 165105 (2002).

[33] E. A. Silinsh, Ĉápek, *Organic Molecular Crystals: Interaction, Localization, and Transport Phenomena* (AIP, New York, 1994).

[34] A. Troisi, G. Orlandi, J. Anthony, *Chem. Mater.* **17**, 5024 (2005).

[35] K. Hannewald, V. M. Stojanović, J. M. T. Schellekens, P. A. Bobbert, G. Kresse, J. Hafner, *Phys. Rev. B* **69**, 075211 (2004).

[36] O. D. Jurchescu, J. Baas, T. T. M. Palstra, *J. Appl. Phys.* **84**, 3061 (2004).

[37] M.-S. Nam, A. Ardavan, R. J. Cava, P. M. Chaikin, *J. Appl. Lett.* **83**, 4782 (2003).

[38] L. Torsi, A. Dodabalapur, L. J. Rothberg, A. W. P. Fung, H. E. Katz, *Science* **272**, 1462 (1996).

[39] N. Koch, *Chem. Phys. Chem.* **8**, 1438 (2007).

[40] P. Hohenberg, W. Kohn, *Phys. Rev.* **136**, B864 (1964).

[41] W. Kohn, *Reprint from Highlights of Condensed- Matter Theory, Soc. Italiana di Fisica* **Course LXXXIX**, 4 (1985).

[42] M. Levy, *Phys. Rev. A* **26**, 1200 (1982).

[43] E. Lieb, *Int. J. Quant. Chem.* **24**, 243 (1983).

[44] W. Kohn, L. J. Sham, *Phys. Rev.* **140**, A1133 (1965).

[45] D. M. Ceperly, *Phys. Rev. B* **18**, 3126 (1978).

[46] D. M. Ceperly, B. J. Alder, *Phys. Rev. Lett.* **45**, 566 (1980).

[47] A. D. Becke, *J. Chem. Phys.* **96**, 2155 (1992).

[48] A. D. Becke, *J. Chem. Phys.* **97**, 9173 (1992).

[49] J. P. Perdew, S. Kurth, *A Primer in Density Functional Theory* (Springer, Berlin, 2003).

[50] J. P. Perdew, K. Burke, M. Ernzerhof, *Phys. Rev. Lett.* **77**, 3865 (1996).

[51] J. P. Perdew, A. Ruzsinszky, G. I. Csonka, O. A. Vydrov, G. E. Scuseria, L. A. Constantin, X. Zhou, K. Burke, *Physical Review Letters* **100**, 136406 (2008).

[52] Y. Zhang, W. Yang, *Phys. Rev. Lett.* **80**, 890 (1998).

[53] B. Hammer, L. B. Hansen, J. K. Norskov, *Phys. Rev. B* **59**, 7413 (1999).

[54] R. Armiento, A. E. Mattsson, *Physical Review B (Condensed Matter and Materials Physics)* **72**, 085108 (2005).

[55] G. I. Csonka, J. P. Perdew, A. Ruzsinszky, P. H. T. Philipsen, S. Lebegue, J. Paier, O. A. Vydrov, J. G. Angyan, *Phys. Rev. B* **79**, 155107 (2009).

[56] P. Haas, F. Tran, P. Blaha, *Physical Review B (Condensed Matter and Materials Physics)* **79**, 085104 (2009).

[57] A. D. Becke, *Phys. Rev. A* **38**, 3098 (1988).

[58] J. P. Perdew, *Phys. Rev. B* **33**, 8822 (1986).

[59] C. Lee, W. Yang, R. G. Parr, *Phys. Rev. B* **37**, 785 (1988).

[60] J. Perdew, *Electronic Structure of Solids '91* (Akademie Verlag, Berlin, 1991), vol. 17 of *Physical Research*, chap. Unified theory of exchange and correlation beyond the local density approximation, pp. 11–20.

[61] J. P. Perdew, J. A. Chevary, S. H. Vosko, K. A. Jackson, M. R. Pederson, D. J. Singh, C. Fiolhais, *Phys. Rev. B* **46**, 6671 (1992).

[62] B. Grabowski, T. Hickel, J. Neugebauer, *Phys. Rev. B* **76**, 024309 (2007).

[63] D. C. Langreth, J. P. Perdew, *Sol. Stat. Comm.* **17**, 1425 (1975).

[64] O. Gunnarsson, B. I. Lundqvist, *Phys. Rev. B* **13**, 4274 (1976).

[65] W. Kohn, *Rev. Mod. Phys.* **71** (1999).

[66] S. Grimme, *J. Comput. Chem.* **25**, 1463 (2004).

[67] A. J. Misquitta, B. Jeziorski, K. Szalewicz, *Phys. Rev. Lett. 91, 033201 (2003)* **91**, 033201 (2003).

[68] K. S. Rafa Podeszwa, *Chem. Phys. Lett.* **412**, 488 (2005).

[69] M. Fuchs, X. Gonze, *Phys. Rev. B* **65**, 235109 (2002).

[70] T. Thonhauser, V. R. Cooper, S. Li, A. Puzder, P. Hyldgaard, D. C. Langreth, *Phys. Rev. B* **76**, 125112 (2007).

[71] D. C. Langreth, M. Dion, H. Rydberg, E. Schrder, P. Hyldgaard, B. I. Lundqvist, *Int. J. Quant. Chem.* **101**, 599 (2005).

[72] O. A. Vydrov, T. V. Voorhis, *J. Chem. Phys.* **130**, 104105 (2009).

[73] X. Wu, M. C. Vargas, S. Nayak, V. Lotrich, G. Scoles, *J. Chem. Phys.* **115**, 8748 (2001).

[74] P. Davis, P. Rabinowitz, *Methods of Numerical Integration* (Academic Press, New York, 1975).

[75] W. H. Press, B. P. Flannery, S. A. Teukolsky, W. T. Vetterling, *Numerical Recipies in Fortran 77* (Cambridge Univ. Press, 2005).

[76] B. L. Fox, *ACM Trans. Math. Soft.* **12**, 362 (1986).

[77] P. Bratley, B. L. Fox, *ACM Trans. Math. Soft.* **12**, 88 (1988).

[78] A. Kokalj, *Comp. Mater. Sci.* **28**, 155 (2003). Code available from http://www.xcrysden.org/.

[79] W. Gordon, *SIAM Journal on Numerical Analysis* **8**, 158 (1971).

[80] N. M. Korobov, *Fizmatgiz* (1963).

[81] T. Hahn, *Comput. Phys. Commun.* **168**, 78 (2005).

[82] J. H. Friedman, M. H. Wright, *ACM Trans. Math. Soft.* **7**, 76 (1981).

[83] M. Matsumoto, T. Nishimura, *ACM Trans. Modeling Comp. Simulation* **8**, 3 (1998).

[84] A. Genz, A. Malik, *SIAM J. Numer. Anal.* **20**, 580 (1983).

[85] S. Baroni, A. D. Corso, S. de Gironcoli, P. Giannozzi, C. Cavazzoni, G. Ballabio, S. Scandolo, G. Chiarotti, P. Focher, A. Pasquarello, K. Laasonen, A. Trave, R. Car, N. Marzari, A. Kokalj, *http://www.pwscf.org/* (2007).

[86] S. Tsuzuki, K. Honda, M. Mikami, T. Tanabe, *J. Am. Chem. Soc.* **124**, 104 (2002).

[87] L. X. Benedict, N. G. Chopra, M. L. Cohen, A. Zettl, S. G. Louie, V. H. Crespi, *Chem. Phys. Lett.* **286**, 490 (1998).

[88] R. Zacharia, H. Ulbricht, T. Hertel, *Phys. Rev. B* **69**, 155406 (2004).

[89] F.-J. M. zu Heringdorf, M. C. Reuter, R. M. Tromp, *Nature* **412**, 517 (2001).

[90] M. A. Loi, E. da Como, F. Dinelli, M. Murgia, R. Zamboni, F. Biscarini, M. Muccini, *Nature Materials* **4**, 81 (2005).

[91] G. Hlawacek, Q. Shen, C. Teichert, R. Resel, D. M. Smilgies, *Surf. Sci.* **601**, 2584 (2007).

[92] M. L. Tiago, J. E. Northrup, S. G. Louie, *Phys. Rev. B* **67**, 115212 (2003).

[93] G. Koller, S. Berkebile, M. Oehzelt, P. Puschnig, C. Ambrosch-Draxl, F. P. Netzer, M. G. Ramsey, *Science* **317**, 351 (2007).

[94] D. Vanderbilt, *Phys. Rev. B* **41**, 7892 (1990).

[95] H. J. Monkhorst, J. D. Pack, *Phys. Rev. B* **13**, 5188 (1976).

[96] J. P. Perdew, A. Zunger, *Phys. Rev. B* **23**, 5048 (1981).

[97] J. S. Chickos, J. William E. Acree, *J. Phys. Chem. Ref. Data* **31**, 537 (2002).

[98] A. T. Hagler, E. Huler, S. Lifson, *J. Am. Chem. Soc.* **96**, 5319 (1976).

[99] I. V. Markov, *Crystal growth for beginners : fundamentals of nucleation, crystal growth and epitaxy* (World Scientific, 2003).

[100] J. E. Northrup, M. L. Tiago, S. G. Louie, *Phys. Rev. B* **66**, 121404(R) (2002).

[101] P. Puschnig, K. Hummer, C. Ambrosch-Draxl, G. Heimel, M. Oehzelt, R. Resel, *Phys. Rev. B* **67**, 235321 (2003).

[102] K. Hummer, P. Puschnig, C. Ambrosch-Draxl, *Phys. Rev. B* **67**, 184105 (2003).

[103] L. F. Drummy, P. K. Miska, D. Alberts, N. Lee, D. C. Martin, *J. Phys. Chem. B* **110**, 6066 (2006).

[104] A. I. Kitaigorodsky, N. A. Ahmed, *Acta Cryst. A* **28**, 207 (1972).

[105] S. Jo, H. Yoshikawa, A. Fujii, M. Takenaga, *Surf. Sci.* **592**, 37 (2005).

[106] G. Heimel, L. Romaner, E. Zojer, *SPIE newsletter* (2008).

[107] F. Mittendorfer, J. Hafner, *Surf. Sci.* **472**, 133 (2001).

[108] F. Mittendorfer, J. Hafner, *Surf. Sci.* **492**, 27 (2001).

[109] S. Picozzi, A. Pecchia, M. Gheorghe, A. D. Carlo, P. Lugli, B. Delley, M. Elstner, *Phys. Rev. B* **68**, 195309 (2003).

[110] A. Hauschild, K. Karki, B. C. C. Cowie, M. Rohlfing, F. S. Tautz, M. Sokolowski, *Phys. Rev. Lett.* **94**, 036106 (2005).

[111] S. X. Du, H. J. Gao, C. Seidel, L. Tsetseris, W. Ji, H. Kopf, L. F. Chi, H. Fuchs, S. J. Pennycook, S. T. Pantelides, *Phys. Rev. Lett.* **97**, 156105 (2006).

[112] F. Ortmann, K. Hannewald, F. Bechstedt, *Appl. Phys. Lett.* **93**, 222105 (2008).

[113] N. Atodiresei, V. Caciuc, J.-H. Franke, S. Blügel, *Phys. Rev. B* **78**, 045411 (2008).

[114] N. Atodiresei, V. Caciuc, P. Lazić, S. Blügel, *Phys. Rev. Lett.* **102**, 136809 (2009).

[115] M. Rohlfing, T. Bredow, *Phys. Rev. Lett.* **101**, 266106 (2008).

[116] S. D. Chakarova-Käck, O. Borck, E. Schröder, B. I. Lundqvist, *Phys. Rev. B* **74**, 155402 (2006).

[117] P. Sony, P. Puschnig, D. Nabok, C. Ambrosch-Draxl, *Phys. Rev. Lett.* **99**, 176401 (2007).

[118] P. Sony, P. Puschnig, D. Nabok, C. Ambrosch-Draxl, *Phys. Rev. B* (2009). Submitted.

[119] L. Romaner, D. Nabok, P. Puschnig, E. Zojer, C. Ambrosch-Draxl, *New J. Phys.* **11**, 053010 (2009).

[120] A. Imanishi, T. Yokoyama, Y. Kitajima, T. Ohta, *Bulletin of the Chemical Society of Japan* **71**, 831 (1998).

[121] P. Milligan, J. McNamarra, B. Murphy, B. Cowie, D. Lennon, M. Kadodwala, *Surf. Sci.* **412/413**, 166 (1998).

[122] A. Imanishi, S. Yagi, T. Yokoyama, Y. Kitajima, T. Ohta, *J. Electron Spectrosc. Relat. Phenom.* **80**, 151 (1996).

[123] B. A. Sexton, *Surf. Sci.* **163**, 99 (1985).

[124] S. Y. Liem, G. Kresse, J. H. R. Clarke, *Surf. Sci.* **415**, 194 (1998).

[125] F. S. Tautz, *Prog. Surf. Sci.* **82**, 479520 (2007).

[126] R. Rurali, N. Lorente, P. Ordejon, *Phys. Rev. Lett.* **95**, 209601 (2005).

[127] M. Rohlfing, R. Temirov, F. S. Tautz, *Phys. Rev. B* **76**, 115421 (2007).

[128] A. Kraft, R. Temirov, S. K. M. Henze, S. Soubatch, M. Rohlfing, F. S. Tautz, *Phys. Rev. B* **74**, 041402(R) (2006).

[129] K. Glöckler, C. Seidel, A. Soukopp, M. Sokolowski, E. Umbach, M. Bohringer, R. Berndt, W.-D. Schneider, *Surf. Sci.* **405**, 1 (1998).

[130] L. Kilian, E. Umbach, M. Sokolowski, *Surf. Sci.* **573**, 359 (2004).

[131] P. Fenter, F. Schreiber, L. Zhou, P. Eisenberger, S. R. Forrest, *Phys. Rev. B* **56**, 3046 (1997).

[132] S. Mannsfeld, M. Toerker, T. T. Schmitz-Hübsch, F. Sellam, T. Fritz, K. Leo, *Org. Electronics* **2**, 121 (2001).

[133] T. Schmitz-Hübsch, T. Fritz, F. Sellam, R. Staub, K. Leo, *Phys. Rev. B* **55**, 7972 (1997).

[134] L. Kilian, E. Umbach, M. Sokolowski, *Surf. Sci.* **600**, 26332643 (2006).

[135] T. Wagner, A. Bannani, C. Bobisch, H. Karacuban, R., Möller, *J. Phys.: Condens. Matter* **19**, 056009 (2007).

[136] A. Hauschild, K. Karki, B. C. C. Cowie, M. Rohlfing, F. S. Tautz, M. Sokolowski, *Phys. Rev. Lett.* **95**, 209602 (2005).

[137] U. Stahl, D. Gador, A. Soukopp, R. Fink, E. Umbach, *Surf. Sci.* **414**, 423 (1998).

[138] J.-P. Jalkanen, F. Zerbetto, *J. Phys. Chem. B* **110**, 5595 (2006).

[139] R. Ruiz, A. C.Mayer, G. G. Malliaras, B. Nickel, G. Scoles, A. Kazimirov, *Appl. Phys. Lett.* **85**, 4926 (2004).

[140] R. Resel, N. Koch, F. Meghdadi, G. Leising, W. Unzog, K. Reichmann, *Thin Solid Films* **305**, 232 (1997).

[141] G. Hlawacek, P. Puschnig, P. Frank, A. Winkler, C. Ambrosch-Draxl, C. Teichert, *Science* **321**, 108 (2008).

[142] T. Michely, J. Krug, *Islands, Mounds and Atoms. Patterns and Processes in Crystal Growth Far from Equilibrium* (Springer, Berlin, 2004).

[143] R. Kern, 'Fundamentals of Epitaxy'. In: *Crystal Growth in Science and Technology* (Plenum Press, New York, 1989).

[144] J.-M. Zhang, M.-Y. Zhang, , K.-W. Xu, *Cryst. Res. Technol.* **3**, 275 (2009).

[145] I. Yagi, K. Tsukagoshia, Y. Aoyagi, *Thin Solid Films* **467**, 168 (2004).

[146] Y. Wu, T. Toccoli, N. Koch, E. Iacob, A. Pallaoro, P. Rudolf, S. Iannotta, *Phys. Rev. Lett.* **98**, 076601 (2007).

[147] K. Hummer, P. Puschnig, S. Sagmeister, C. Ambrosch-Draxl, *Mod. Phys. Lett. B* **20**, 261 (2006).

[148] C. Ambrosch-Draxl, K. Hummer, S. Sagmeister, P. Puschnig, *Chem. Phys.* **325**, 3 (2006).

[149] D. Nabok, P. Puschnig, C. Ambrosch-Draxl, O. Werzer, R. Resel, D.-M. Smilgies, *Phys. Rev. B* **76**, 235322 (2007).

[150] A. Moser, O. Werzer, H.-G. Flesch, M. Koini, D.-M. Smilgies, D. Nabok, P. Puschnig, C. Ambrosch-Draxl, M. Schiek, H.-G. Rubahn, R. Resel, *Eur. Phys. J. Special Topics* **168**, 59 (2009).

[151] O. Werzer, Structure and morphology of thiophene based polymers and pentacene for organic electronics: an x-ray based study, Ph.D. thesis, Graz University of Technology (2008).

[152] A. Moser, Crystal structure determination from two-dimensional powders. studies on rod-like conjugated molecules, Master's thesis, Graz University of Technology (2008).

[153] M. Birkholz, *Thin Film Analysis by X-Ray Scattering* (Wiley-VCH Verlag, 2006).

[154] R. Feidenhans'l, *Surf. Sci. Rep.* **10**, 105 (1989).

[155] J. Als-Nielsen, D. McMorrow, *Elements of Modern X-Ray Physics* (John Wiley & Sons, 2001).

[156] W. Kraus, G. Nolze, *J. Appl. Cryst.* **29**, 301 (1996).

[157] D.-M. Smilgies, *Rev. Sci. Inst.* **73**, 1706 (2002).

[158] K. Hummer, On the electro-optical properties of oligo-acenes, Ph.D. thesis, Universität Graz (2003).

[159] C. D. Dimitrakopoulos, D. J. Mascaro, *IBM. J. Res. & Dev.* **45**, 11 (2001).

[160] C. C. Mattheus, A. B. Dros, J. B. A. Meetsma, J. L. de Boer, T. T. M. Palstra, *Acta Cryst. C* **57**, 939 (2001).

[161] C. C. Mattheus, A. B. Dros, J. Baas, G. T. Oostergetel, A. Meetsma, J. L. de Boer, T. T. M. Palstra, *Synth. Met.* **138**, 475 (2003).

[162] R. B. Campbell, J. M. Robertson, *Acta Cryst.* **15**, 289 (1962).

[163] D. Holmes, S. Kumaraswamy, A. J.Matzger, K. P. Vollhardt, *Chem. Eur. J.* **5**, 3399 (1999).

[164] T. Siegrist, J. S. C. Kloc, B. Batlogg, R. C. Haddon, S. Berg, G. A. Thomas, *Angew. Chem.Int. Ed.* **40**, 1732 (2001).

[165] H. Yoshida, K. Inaba, N. Sato, *Appl. Phys. Lett.* **90**, 181930 (2007).

[166] S. Schiefer, M. Huth, A. Dobrinevski, B. Nickel, *J. Am. Chem. Soc.* **129**, 10316 (2007).

[167] S. Kowarik, A. Gerlach, W. Leitenberger, J. Hu, G. Witte, C. Wöll, U. Pietsch, F. Schreiber, *Thin Solid Films* **515**, 5606 (2007).

[168] A. C. Mayer, A. Kazimirov, G. G. Malliaras, *Phys. Rev. Lett.* **97**, 105503 (2006).

[169] C. D. Dimitrakopoulos, A. R. Brown, A. Pomp, *J. Appl. Phys.* **80**, 2501 (1996).

[170] D. J. Gundlach, T. N. Jackson, D. G. Schlom, S. F. Nelson, *Appl. Phys. Lett.* **74**, 3302 (1999).

[171] J. Puigdollers, C. Voz, A. Orpella, I. Martin, M. Vetter, R. Alcubilla, *Thin Solid Films* **427**, 367 (2003).

[172] T. Kakudate, N. Yoshimoto, Y. Saito, *Appl. Phys. Lett.* **90**, 081903 (2007).

[173] H. Yoshida, N. Sato, *Appl.Phys. Lett.* **89**, 101919 (2006).

[174] S. E. Fritz, S. M. Martin, C. D. Frisbie, M. D. Ward, M. F. Toney, *J. Am. Chem. Soc.* **126**, 4084 (2004).

[175] V. Vand, *Acta Cryst.* **1**, 109 (1948).

[176] J. S. Wu, C. H. Spence, *J. Appl. Cryst.* **37**, 78 (2004).

[177] P. E. Blöchl, *Phys. Rev. B* **50**, 17953 (1994).

[178] K. Hummer, C. Ambrosch-Draxl, *Phys. Rev. B* **72**, 205205 (2005).

[179] F. Balzer, H.-G. Rubahn, *Adv. Funct. Matter.* **15**, 17 (2005).

[180] G. Leising, S. Tasch, W. Graupner, *Fundamentals of Electroluminescence in Paraphenylene-Type Conjugated Polymers and Oligomers, in Handbook of Conducting Polymers* (M. Dekker, New York, 1998, 1998), second edn.

[181] J. Brewer, M. Schiek, I. Wallmann, H.-G. Rubahn, *Opt. Comm.* **281**, 3892 (2008).

[182] M. Schiek, F. Balzer, K. Al-Shamery, A. Lützen, H.-G. Rubahn, *Soft Mat.* **4**, 277 (2008).

[183] M. Schiek, F. Balzer, K. Al-Shamery, J. Brewer, A. Lützen, H.-G. Rubahn, *Small* **4**, 176 (2008).

[184] F. H. Allen, *Acta Cryst.* **B58**, 380 (2002).

List of Publications

The list comprises a number of publications that have been written during the development of this thesis. They can be considered as a supplementary material to the results presented in the thesis.

[P-1] P. Sony, P. Puschnig, D. Nabok, C. Ambrosch-Draxl, *Phys. Rev. Lett.* **99**, 176401 (2007).

[P-2] D. Nabok, P. Puschnig, C. Ambrosch-Draxl, O. Werzer, R. Resel, D.-M. Smilgies, *Phys. Rev. B* **76**, 235322 (2007).

[P-3] D. Nabok, P. Puschnig, C. Ambrosch-Draxl, *Phys. Rev. B* **77**, 245316 (2008).

[P-4] A. Moser, O. Werzer, H.-G. Flesch, M. Koini, D.-M. Smilgies, D. Nabok, P. Puschnig, C. Ambrosch-Draxl, M. Schiek, H.-G. Rubahn, R. Resel, *Eur. Phys. J. Special Topics* **168**, 59 (2009).

[P-5] L. Romaner, D. Nabok, P. Puschnig, E. Zojer, C. Ambrosch-Draxl, *New J. Phys.* **11**, 053010 (2009).

[P-6] P. Sony, P. Puschnig, D. Nabok, C. Ambrosch-Draxl (submitted to *PRB*).

[P-7] D. Nabok, P. Puschnig, C. Ambrosch-Draxl, (to be submitted *Comp. Phys. Commun.*).